MOBILE UNDERWATER ACOUSTIC COMMUNICATIONS WITH MULTICARRIER MODULATION IN VERY SHALLOW WATERS

YONG XU CHANG
B.Eng. (Hons.), NUS

A THESIS SUBMITTED FOR THE DEGREE OF
MASTER OF ENGINEERING

DEPARTMENT OF ELECTRICAL & COMPUTER ENGINEERING
NATIONAL UNIVERSITY OF SINGAPORE

2007

Acknowledgements

The completion of this thesis marks the end of a memorable and eventful academic pursuit under the Double Degree Program in Engineering hosted by the National University of Singapore.

I would like to extend my heartfelt thanksgiving to my supervisor, Dr. Samir Attallah, whose support and patience throughout the course of my academic pursuit has been greatly appreciated. I would also like to thank Dr. Mandar Chitre for his invaluable guidance, insights and assistance rendered in making this thesis possible.

My deepest gratitude goes out to my family and friends, whose support, understanding and encouragement I will always remember and cherish.

Table of Contents

Summary

Communications in shallow underwater acoustic channel is challenged by strong reverberations, fast time varying statistics and impulsive ambient noise. Using channel measurements and analysis studied previously, a complete communication scheme is developed to allow for mobile communications. The receiver design combines different methods tested for signal detection, synchronization, mobility-induced Doppler compensation and channel equalization using spatial diversity techniques. The final system constructed implements linear frequency modulated signals for detection, synchronization and Doppler acquisition, linear interpolation for Doppler compensation and finally orthogonal frequency division multiplexing (OFDM) and differential phase shift keying (DPSK) for signal and data modulation. The performance results are based solely upon simulated data.

List of Tables

List of Figures

Abbreviations and Symbols

Abbreviations

BER	Bit error rate
CIR	Channel impulse response
CFAR	Constant false alarm rate
CFO	Carrier frequency offset
DFE	Decision feedback equalizer
DOA	Direction of arrival
DSP	Digital signal processing
ESPRIT	Estimation of signal parameters via rotational invariance techniques
FLOM	fractional low-order moments
ICI	Inter-carrier interference
ISI	Inter-symbol interference
ISNR	Interference and signal-to-noise ratio
LFM	Linear frequency modulated
ML	Maximum likelihood
MMSE	Minimum mean square error
MSE	Mean square error
MSSNR	Maximum shortening signal-to-noise ratio
PDF	Probability density function
PLL	Phase-locked-loop
PSD	Power spectrum density
RMS	Root mean square
SαS	Symmetric alpha-stable
SINR	Signal-to-interference and noise ratio
SNR	Signal-to-noise ratio
UWA	Underwater acoustic communications

Symbols

B_c	Coherence bandwidth
B_d	Doppler spread
B_{LFM}	Chirp signal bandwidth
B_s	Signal bandwidth
D_k	Data symbol on k^{th} OFDM sub-carrier
Δ	Doppler time scaling factor
ε_{beam}	Threshold for conditioning number in spatial beamforming
ε_{dop}	Threshold for Doppler estimate error between multiple channels
ε_{sym}	Threshold for symbol timing error between multiple channels
f_c	Carrier frequency
f_s	Sampling frequency
L_r	Length of input signal in least square spatial beamforming
λ	Forgetting factor for least square spatial beamforming
N	Number of OFDM sub-carriers
N_p	Length of OFDM cyclic prefix
τ_{ds}	Duration of delay spread
T_c	Coherence time of UWA channel
T_{LFM}	Duration of chirp signal
T_{rp}	Measured duration between chirp signals
T_{tp}	Actual duration between chirp signals
T_s	Duration of symbol

1. Introduction

1.1. Background

The technological advent of underwater explorations, off-shore mining operations, oceanography and several other applications has challenged underwater communications to keep in pace with current advancements, or risk becoming the bottleneck of today's high speed technology. Not only do we demand a fast and reliable communications link, the vastness of the oceans has also prompted a need for untethered, wireless connection.

Communications underwater has always been conducted via sound because electromagnetic as well as optical waves attenuate rapidly in sea water. However, underwater acoustic communications (UWA) is by no means without problems. In very shallow waters, characterized by sea bed depths of less than 50 meters, sound transmission is subjected to long reverberations and refractions. In addition, scattering resulting from inhomogeneities within the sea as well as the random motion of the sea surface gives rise to an extensive, time-varying multipath communication channel [37].

Earlier methods of UWA communications focused mainly on non-coherent and spread spectrum techniques in order to overcome the underlying problems of limited bandwidth, time-varying channel impulse response (CIR) as well as channel phase variation [4, 14]. However, these methods tend to be bandwidth inefficient, having data rates that are typically less than 1 kilobits per second (kbps). With the growth of digital signal processing (DSP) technology, research focus has now shifted to phase coherent modulation techniques. Although such methods are typically more complicated and require accurate synchronization, the higher bandwidth achievable is an important factor

of consideration. Recent advanced techniques applying decision feedback equalizers (DFE) coupled with second order phase-locked-loops (PLL) have yield data rates of up to 10 kbps under medium range, shallow UWA channels [38, 39].

Often, bandwidth efficiency is proportional to computational complexity. The severe time-dispersion of UWA channels results in inter-symbol interference (ISI), which effectively reduces the transmission bandwidth should there be no equalization involved. Time reversal mirroring (TRM) employs the time symmetry in wave equation and requires rather slow time-varying channel to effectively refocus the energy back at the transmission source [8, 16]. In single carrier modulation techniques, long adaptive equalizers are used [13]. Multi-carrier systems employing orthogonal frequency division multiplexing (OFDM) implicitly equalize the dispersive channel with the implementation of a cyclic prefix that exceeds the delay spread of the channel [17], effectively reducing the bandwidth with increasingly time-dispersive channel. Channel shortening filters, which essentially equalize the channel partially to a targeted delay spread, have been employed in ADSL lines as well as UWA channels so as to improve the bandwidth efficiency of OFDM [7, 20, 36]. Spatial diversity techniques via multi-channel combining have also proven to be effective in combating reverberations by focusing upon the direction of arrival (DOA) of the first signal path [38, 40].

In the context of Singapore waters, UWA communications is further complicated by severe Rayleigh fading as well as the presence of snapping shrimps which contributes to highly impulsive ambient noise levels in the channel [6, 28, 29]. Modelled as symmetric alpha stable (SαS) distributions, such impulsive noises have no closed form probability density function (PDF) [27], hence invalidating methodologies under

Gaussian noise assumptions. The stable family of distributions, instead, arises out of a generalized Central Limit Theorem which states that the sum of independent and identically distributed random variables, with or without a finite variance, converges to a stable distribution by increasing the number of variables [27]. Intensive studies have been made to model the channel, with the consensus that the multipath structure of the channel arises from distinct eigen-rays that are separable in short ranges but tend to combine quickly at medium to long range [5, 41]. Coherent methods have been employed using both single and multi carrier modulations further coupled with coding to improve the overall bit error rate (BER).

In order to factor mobility in UWA communications, precautions must be taken to first understand the influence of Doppler spread in this medium. Whilst propagation speed in the air via radio frequency is rapid enough to marginalize Doppler effects as a carrier frequency shift, the propagation speed of sound in water is considerably slower. In addition, the practical limit upon the carrier frequency in UWA communications results in the signal being wideband at high data rate transmission. Thus, the Doppler contribution in UWA channels under mobility conditions consists of a spread as well as an overall shift of the entire frequency spectrum [10, 23].

Research has been done to derive maximum likelihood (ML) as well as estimation of signal parameters via rotational invariance techniques (ESPIRIT) estimators to compensate for the Doppler corruption in OFDM [33]. Compensation methods that involve lower computational complexities use linear interpolation to offset the compression / expansion effect contributed by mobility upon the signal. Simulations have been conducted on both single-carrier and multi-carrier modulation using such a

technique of compensation [15, 33, 35]. In addition, sea trials were successfully conducted upon the single-carrier systems, reporting a data rate of 16kbps at velocities up to 2.6 m/s with acceleration up to 1 m/s^2 [34].

1.2. Thesis Contributions

This thesis is part of the Double Degree Program with French Grandes Ecoles organized by National University of Singapore and was conceived within a project framework funded by Defence Science Organisation of Singapore. The key aim is to implement an UWA communications system for a fleet of autonomous underwater vehicles based on the best simulation results obtained from an amalgamation of various methods for wireless communications. These methods are not novel and can be commonly found in the literature of engineering research publications.

With the knowledge of the constraints in shallow UWA communications as well as with the methodology used to overcome some of these challenges, the aim is now to develop a wireless acoustic telemetry that allows for reliable, mobile, high-performance communication subjected to impulsive ambient noise at all ranges. The work done in this thesis is highly reliant upon the accuracy of the channel model developed in [5] for the design of UWA communication systems in the context of Singapore waters.

An attempt to exhaust the vast resource of communication techniques developed over the decades for use in shallow waters would not be feasible. Hence, this thesis focuses on developing OFDM, a modulation technique that is gaining great popularity, as the choice of telemetry. Another of the objectives in this project is to concentrate upon the development of the physical layer of communications; hence correction codes will not be mention in this discourse but can nevertheless be easily implemented into the system.

The key contributions of this thesis are essentially to:

i. Study the performance of wideband OFDM under mobility conditions. It can be shown that even under favourable channel conditions, mobility-induced Doppler of wideband signals cannot be compensated for using narrowband techniques.

ii. Evaluate the choice of Doppler compensation for application. Linear interpolation is the preferred method of two that were studied for its low computational complexity and ease of implementation.

iii. Develop a reliable detection and synchronization algorithm under severe Rayleigh fading conditions and short channel coherence time. Due to the fact that the strength of signals from surface reflected arrivals can be greater than that of direct arrivals within this channel, the synchronization algorithm must be able to make a decision as to which path to lock upon.

iv. Utilize spatial diversity to counter the severe time-dispersion of the channel. At shorter ranges, the DOA of each eigen-ray can be differentiated and hence equalized using multi-channel combining.

v. Design a signal frame that maximizes the bandwidth given physical limitations of the transducers and severe channel conditions.

1.3. Thesis Outline

The thesis is organized into 7 main chapters, of which the first has been dedicated to give the readers a general understanding of shallow UWA communications in impulsive ambient noise and mobile conditions.

Chapter 2 reviews the salient points of the channel model that constraints the parameterization of the communications schematic. Within this chapter, the reader will

discover in greater detail the characteristics of the channel such as SαS noise distribution, coherence fading time, Doppler spread as well as delay spread.

We find in Chapter 3 the physics of Doppler spread in wideband signals, as well as an analysis of correction methods commonly applied to the signal under narrowband and wideband assumptions. Chapter 4 presents an analysis of the detection and synchronization algorithm applied at the receiver end to ensure reliable coherent communication.

The findings from chapters 2 to 4 decide the overall structure of the signal frame in Chapter 5. The signal frame is then used in simulations to understand its suitability and overall performance. Chapter 6 supplements the experimental results by attempting multi-channel combining to take advantage of spatial diversity for better performance.

Finally, Chapter 7 summarizes the key findings from this research and highlights the possible directions for future work.

2. Shallow Underwater Acoustic Channel

Characterization of the channel model with respect to measurement taken off Singapore waters has been done by both Chitre [5] and Tan [41] with experimental results that concur very closely with each another. The focus of this chapter is thus to review the important features of the channel model that would aid in the design of the communications system.

2.1 Channel Propagation Model

The Helmholtz wave equation gives a theoretical description of UWA propagation. Characteristics of both the bottom and the surface of shallow waters determine the acoustic field arising from reflections. On the other hand, the velocity of sound over different sections of the water channel determines how the acoustic field is refracted. Sound propagation at high frequencies may be modelled using ray theory, whereby the underlying assumption is of sound waves travelling in straight lines in an isovelocity medium [3, 43].

2.1.1 Sound Velocity

The governing factors of sound velocity in water are temperature and salinity [14]. The temperature in warm shallow waters is not expected to vary greatly and the salinity of water is expected to be constant unless it is near freshwater source (e.g. river mouths). Figure 2.1[*] shows a sample of the profile of sound velocity in waters off Singapore,

[*] The figure has been reproduced from [18] for cross-reference purposes

validating the assumption of an isovelocity channel. In this thesis, we shall assume a slightly lower, theoretical velocity of 1500 m/s for simplicity of calculation and simulation. This assumption is valid as a lower propagation speed leads to more pronounced wideband effects on signals, which requires more compensation. Also, the practical limits of mobility that are applied in this thesis are low as compared to the assumed propagation speed, hence the Doppler spread will only be affected marginally. The rationale is revisited in Chapter 3, where mathematical studies are made on how the speed of sound and mobility affects wideband signals.

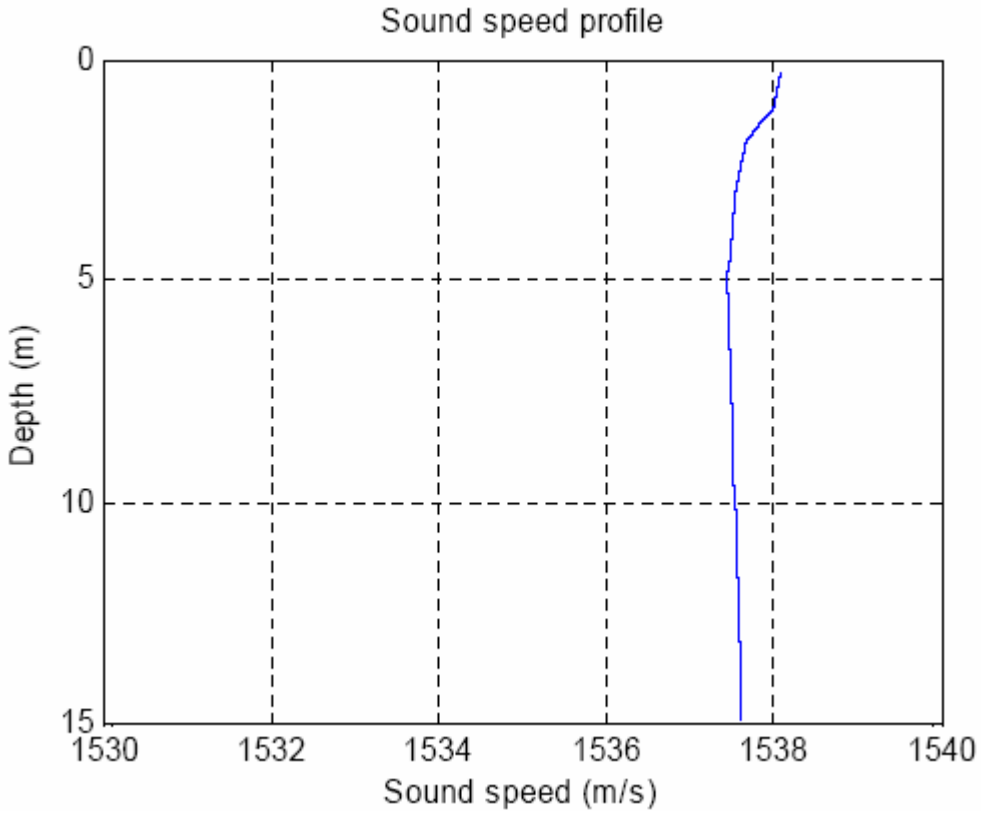

Figure 2.1: Typical sound velocity profile in warm shallow waters off Singapore

2.1.2 Delay Spread and Coherence Bandwidth

Delay spreads are measurements of the time taken between the arrival of the first signal path and last, detectable signal path which depends on the signal-to-noise ratio (SNR). Excessive delay spreads leads to severe ISI: in single carrier systems, this will influence the length of adaptive filter required to equalize the channel [13]; in multi-carrier systems like OFDM, the guard time of the cyclic prefix will be proportional to the delay spread if no pre-equalization is performed.

Even with a cyclic prefix, the duration of delay spreads, τ_{ds}, will still affect the performance of OFDM due to frequency domain nulls on certain sub-carriers [17]. Multiple paths that are sparsely located in time leads to more nulls in the signal bandwidth. In addition, secondary paths of arrival that are stronger will lead to deeper nulls. In a noisy environment, this will degrade the detection of the affected sub-carriers.

Estimates of the coherence bandwidth, B_c, can be obtained from Doppler spreads using the following equation [32]:

$$B_s = \frac{0.423}{\tau_{ds}} \tag{2.1}$$

The coherence bandwidth gives a statistical measure of the range of frequencies that undergo *flat fading*. All frequency components within this range are considered to be correlated and hence undergo the same amount of fading. In the context of signal design, distortion is minimised when the signal bandwidth is less than the coherence bandwidth. Hence, when considering OFDM as the choice of signal modulation, each sub-carrier bandwidth should not exceed the expected coherence bandwidth; otherwise *frequency selective fading* will occur.

Table 2.1[*]: Delay spread and coherence bandwidth at different transmission ranges.

Range (m)	Delay Spread τ_{ds} (ms)	Coherence Bandwidth B_c (Hz)
80	5.5	77
130	7.0	60
560	3.0	141
1040	3.5	121
1510	2.5	169
1740	1.3	325
2740	0.5	846

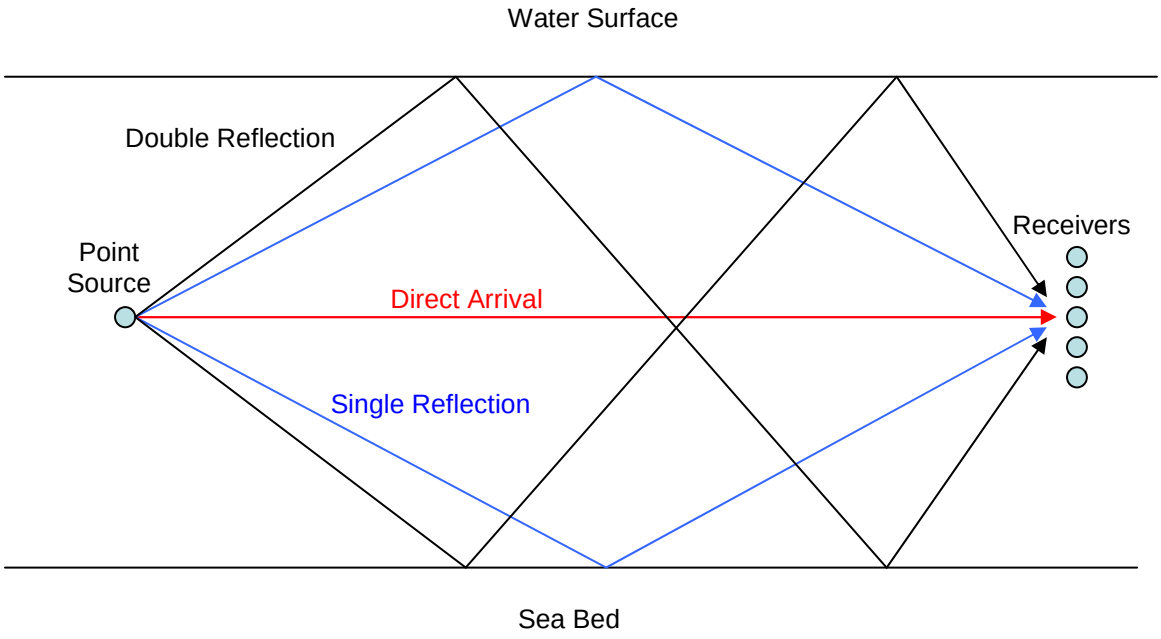

Figure 2.2: Shallow water multipath model with up to 2 reflections

Figure 2.2 shows the signal arriving from the direct path, single reflections and double reflections that constitute the multipath model and hence a delay spread. As the distance between the transmitter and receiver increases, the DOA of each path becomes harder to differentiate. Also, the delay spread will tend to reduce with transmission range, as shown in Table 2.1, since the horizontal distance then becomes more dominant compared to the vertical distance travelled by the reflected signals.

[*] The table has been partially reproduced from [19] for cross-reference purposes

2.1.3 Fading Characteristics

Two models are commonly used to characterise fading in multipath environments: the Rician distribution and the Rayleigh distribution [32]. The former is normally applied when there is a line of sight between transmitter and receiver whereas the latter does not make such an assumption.

Usually, Rayleigh fading occurs due to the aggregation of numerous signal paths. Both authors of [5] and [41] concluded that the fading statistics conforms to that of a Rayleigh distribution at shorter ranges (< 100m), although the direct path arrival exhibits less severe fading statistics than predicted by the model at this range. Rayleigh fading was reported in [41] at medium ranges (between 500m to 1000m) whereas a novel model resulting from the difference between two independent Rayleigh random variables was found to be the best fit for the empirical data collected. Long ranges (1500m and above) yielded fading statistics that are similar to the Rician distribution in [41].

In order to simplify channel simulations, this thesis assumes, as in [5], a Rayleigh fading upon each eigen-ray resulting from the channel.

2.1.4 Background Doppler Effects

Due to the dynamics within the water channel, time variation occurs in the arrival paths. That, as a result, leads to a phase modulation of the signal, of which the bandwidth of the modulation is defined to be the Doppler spread B_d [37]. As the name suggests, this effect broadens the bandwidth of a narrowband signal about its centre frequency.

The importance of understanding Doppler spread is because it dictates the maximum possible transmission duration of a symbol. In single carrier systems, the symbol duration, T_s, is inversely proportional to the signal bandwidth B_s ($T_s = 1/B_s$). In

OFDM, the symbol duration depends on the number of sub-carriers N_c, the length of cyclic prefix N_p as well as the signal bandwidth B_s ($T_s = (N_c + N_p)/B_s$). This time constraint is known as the coherence time, which is the time duration whereby there exists a certain level of correlation in the CIR. It the symbol duration is insignificant compared to the coherence time, then *slow fading* occurs. In such a situation, the influence of Doppler spread upon the performance in terms of BER is negligible. Vice versa, *fast fading* results in distortion of the signal and hence a penalty upon the BER.

A popular rule of thumb is taken at the 50% coherence time T_c [32], meaning that correlation levels will be at least 50%:

$$T_c = \frac{0.423}{B_d} \tag{2.2}$$

Doppler spreads have been found empirically in [5] to be between 5 to 10 Hz. This concurs with the measurements in [41], showing that Doppler spread decreases as the transmission range increases. Table 2.2[*] shows the typical profile of Doppler spread across varying transmission range.

Table 2.2: Delay spread and coherence bandwidth at different transmission ranges.

Range (m)	Doppler Spread B_d (Hz)	50% Coherence Time T_c (ms)
80	9	47
130	8	53
560	4	106
1040	3	141
1510	2	212
1740	2	212
2740	3	141

[*] The table has been partially reproduced from [19] for cross-reference purposes

2.1.5 Overall Power Loss

Besides fading which leads to temporal loss in acoustic intensity, two other major factors lead to an overall attenuation of acoustic signals with increasing distance from the source: cylindrical spreading and volume absorption.

Cylindrical spreading arises from an omni-directional propagation of waves from the source. In an isovelocity medium, the finite amount of energy dissipated from the source is evenly spread over the spherical wavefront. As the distance increases, so does the surface area of the sphere hence the energy per unit area decreases resulting in attenuation.

Volume absorption is frequency dependent and the resulting signal attenuation becomes more significant with increasing distance of transmission and at high frequencies (typically more than 2 kHz). An empirical expression of attenuation resulting from volume absorption can be found in Eq. (6.7) of [5].

Energy is dissipated in terms of surface and bottom reflection losses when the acoustic wavefront comes into contact with the sea surface and sea bed respectively. Surface reflection losses are less significant compared to bottom reflection losses; the reflection coefficient can be taken as -1 when the sea surface is calm, which translates to merely a change in phase of the signal. Part of the sound energy is usually absorbed via refraction at the seabed. Eqs. (6.8) and (15) of [5] and [41], respectively, describes the Rayleigh coefficient of reflection used in modelling the channel.

2.2 Channel Noise Model

The UWA channel, in the context of Singapore waters, has an ambient noise dominated by snapping shrimps at frequencies beyond 2 kHz [28, 29]. Strong ambient

noise is detected at frequencies lower than 1 kHz, resulting largely from shipping activities and surface waves. Sea water acts generally as a low pass filter for ambient noise, attenuating it more at higher frequencies [5]. Figure 2.3* shows an example of the power spectrum density (PSD) of ambient noise in waters of an anchorage area.

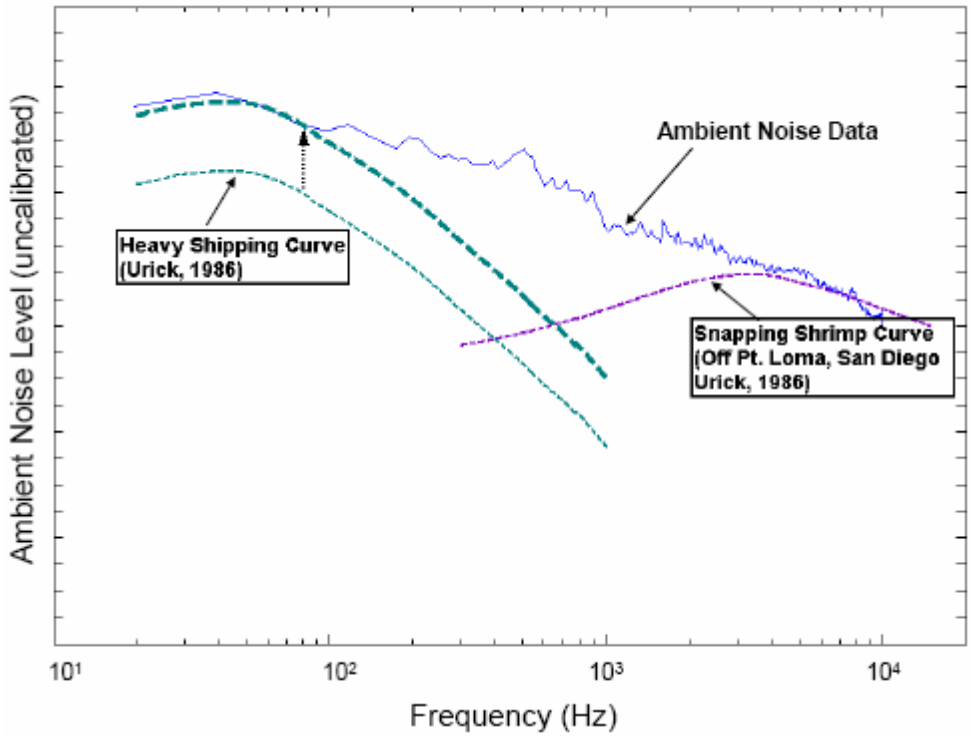

Figure 2.3: Typical Ambient noise profile in warm shallow waters

Snapping shrimp noise has been found to be highly impulsive in nature [5, 41]. As such, the Gaussian distribution has been found to conform poorly to data collected for ambient noise in Singapore waters. We thus look instead towards the generalized Central Limit Theorem, from which the SαS distribution arises, to better understand the channel noise model [27].

* The figure has been reproduced from [30] for cross-reference purposes

2.2.1 SαS Distribution

The SαS distribution can be viewed as a generalized distribution which encompasses both the Gaussian and Cauchy distributions. Alpha-stable distributions are parameterized by four variables. In the case of a zero-mean and SαS distribution, which is the noise distribution model of snapping shrimps, then only two variables are required to describe the characteristic function: the characteristic exponential α and the scale parameter γ. Both parameters must strictly be positive. In addition, the zero mean Cauchy and Gaussian distributions are obtained when α takes on the value of 1 and 2 respectively.

2.2.2 Properties of SαS Random Variables

Although there are many theorems involving the SαS distribution, the following properties would give us a necessary understanding of how to deal with ambient noise. Rigorous proofs have been given in [27] and hence are not reproduced here.

Property 1: Stability Property

A random variable X has a stable distribution if and only if for all X_1 and X_2, independent, with the same distribution as X, and for arbitrary constants a_1 and a_2, there exists constants a and b, such that:

$$a_1 X_1 + a_2 X_2 \overset{d}{=} aX + b \tag{2.3}$$

Property 2: Existence of Lower-order Moments

Let X be a SαS random variable with characteristic exponent α. The p-order moment of X can be expressed as $E|X|^p$. If $\alpha < 2$,

$$E|X|^P < \infty \qquad \text{if } 0 \le p < \alpha$$
$$E|X|^P = \infty \qquad \text{if } p \ge \alpha \tag{2.4}$$

When α = 2,

$$E|X|^P < \infty \qquad \forall p \tag{2.5}$$

For $\alpha < 1$, the SαS distribution has no finite first- or higher-order moments. For $1 < \alpha < 2$, the SαS distribution has a finite first-order moment and fractional low-order moments (FLOM) but an *infinite* variance and higher-order moments. When $\alpha = 2$, all moments exist.

Property 3: No closed-form PDF

With the exception of $\alpha = 2$ (Gaussian) and $\alpha = 1$ (Cauchy), the distribution of the random variables do not take on a closed-form expression.

Property 4: Dependency of Complex Isotropic SαS Random Variables

A complex SαS random variable $X = X_1 + jX_2$ is isotropic (or rotationally invariant) if X_1 and X_2 are SαS random variables and

$$e^{j\phi}X \overset{d}{=} X \qquad \forall \phi \in [0, 2\pi) \tag{2.6}$$

If the SαS random variables are of $\alpha = 2$, the random variable X is a complex isotropic Gaussian random variable, whereby the isotropy condition is satisfied by X for independently and identically distributed X_1 and X_2 with Gaussian distributions. This is the well known fact that complex Gaussian noise has independent real and imaginary components. For $\alpha < 2$, X_1 and X_2 cannot be independent [27], implying that the real and imaginary components of complex isotropic SαS noise processes are in fact dependent.

2.2.3 Signal to Noise Ratio (SNR)

From the second property of the previous section, it is evident that ambient noise in warm shallow waters does not have a finite variance theoretically since the value of α is empirically found to be approximately 1.7 [5]. In view of providing mobility to UWA communications, a practical approach would assume that the communications system is running on an autonomous but limited power supply. Thus, the signal strength at the transmitter would be highly dependent on the available power left. In addition, fast time-varying Rayleigh fading and strong signal attenuation can greatly distort the signal strength at the receiver end.

A method of circumventing the issue of infinite variance has been proposed in [27], whereby the dispersion, γ, of SαS noise is used to replace the variance taken from the Gaussian noise model:

$$\gamma = \left(\frac{\sqrt{N_0}}{2} \right)^{\alpha} \tag{2.7}$$

Evidently, when $\alpha = 2$, the dispersion is equivalent to the expression of the variance of Gaussian random variables.

SNR is measured from a specific point of reference. Since this thesis concentrates on designing a robust receiver in shallow UWA channels, the variance of the signal at the receiver end together with the deterministic value of the variance of simulated ambient noise is thus used to study the performance of the communications system under varying noise conditions. The simplicity of this method allows for a comparison of the BER of a precise signal modulated under identical channel conditions but varying noise strength. The disadvantage however is that the signal envelope will vary greatly under long

transmission durations, thereby the localised ratio at certain points in time of the signal would vary greatly. Shorter transmission durations within the order of the channel coherence time would minimise such a distortion.

The measurement is thus defined as the interference and signal to noise ratio (ISNR), since the variance of the signals arriving from different paths are taken as part of the signal envelope strength.

2.3 Conclusion

Characterisation of the channel model in this chapter allows for an understanding of the constraints in designing and measuring the performance of an UWA communications system. The channel is highly dispersive at short ranges, but the delay spread reduces significantly with transmission distance. Fast time-varying Rayleigh fades in this channel where background Doppler spread is more prominent at short transmission ranges.

The lack of a closed form expression for SαS distributions poses difficulty in analysing SNR, although the signal to noise dispersion ratio has been proposed as an alternative. Instead, this thesis uses the ISNR at the receiver end due to rapid variations in the channel conditions as well as the ease of implementation via the deterministic variances of both the signal and noise.

3. Doppler Compensation Schemes

In order to understand the severity of Doppler spread in wideband[*] signals, we examine how a narrowband[†] assumption and compensation technique would fare. The dominant effect under this assumption is a Doppler shift of the carrier frequency, leading to compensation of the carrier frequency offset (CFO). In this chapter, we first define the framework of mobility induced Doppler and that of the communications scheme before analysing the performance in terms of BER when applying different Doppler compensation methods under both narrowband and wideband assumptions

3.1 Mobility in Wideband Signals

3.1.1 Single Path Doppler Contribution

We first begin by developing a simplified mathematical model in order to understand how mobility affects a signal. Considering a baseband signal *u(t)* that is modulated on a carrier frequency f_c. The resulting passband signal *s(t)* that is transmitted is simply:

$$s(t) = \mathrm{Re}\left\{u(t)e^{j2\pi f_c t}\right\} \tag{3.1}$$

At the receiver end, assuming a relative velocity of *v*, a propagation speed of *c*, and an attenuation of the signal *a(t)*, the received signal *r(t)* can be expressed as:

$$r(t) = a(t)s(t + \frac{v}{c}t - \tau(t)) = a(t)s\big((1+\Delta)t - \tau(t)\big) \tag{3.2}$$

[*] A signal is wideband should the bandwidth be within octave range of the centre frequency
[†] A signal is narrowband should the bandwidth be insignificant compared to the centre frequency

where $\tau(t)$ is a delay incurred due to the transmission distance. Assuming that $a(t)$ and $\tau(t)$ are slow time varying processes, the baseband equivalent of $r(t)$ would then be:

$$r(t) = au\big((1+\Delta)t\big)e^{j2\pi f_c \Delta t} e^{j2\pi f_c \tau} \tag{3.3}$$

and the Fourier transform of the received baseband signal is:

$$R(f) = ae^{j2\pi f_c \tau} U\big((f - f_c\Delta)/(1+\Delta)\big) \tag{3.4}$$

From Eq. (3.4), a Doppler time scaling factor of $\Delta = v/c$ as well as a shift of $f_c\Delta$ is applied to the frequency spectrum of the signal. Whilst communications done on radio frequencies have propagation speeds in the order of 10^7, UWA communications are done at much lower speeds. As seen in Chapter 2, a typical sound profile would propagate at 1500m/s in shallow waters. Assuming a maximum relative velocity of 5m/s, then $\Delta = v/c$ = 1/300. Using Eq. (3.3), the discrete baseband signal is expressed as:

$$r(nT_s) = au\big((1+\Delta)nT_s\big)e^{j2\pi f_c \Delta n T_s} e^{j2\pi f_c \tau} \tag{3.5}$$

where T_s is the duration of each discrete sample. This translates to a slippage of 1 sample for every 300 samples taken from the received signal. In the case of OFDM, this would severely hinder the maximum length of a symbol possible.

3.1.2 Multi-path Doppler Contribution

Under multipath conditions, the angle of arrival θ_p at the receiver varies for each path. In such a case, each individual path contribution to the Doppler scaling factor is $\Delta_p = \Delta \cos \theta_p$. The received passband signal is thus:

$$r(t) = \sum_{p=0}^{L_p - 1} a_p s\big((1+\Delta_p)t - \tau_p\big) \tag{3.6}$$

As the different arrivals are dominated by surface and bottom reflections, the angle of arrival will vary greatly under rapid vertical movement. Under horizontal motion, the Doppler scaling factor for each path can be considered to be identical. This thesis assumes that the relative vertical motion of the mobile platform is quasi-stationary with respect to time duration, hence the Doppler contribution of individual paths are equal:

$$r(t) = \sum_{p=0}^{L_p - 1} a_p s\left((1+\Delta)t - \tau_p\right) \tag{3.7}$$

3.2 Communications Framework

3.2.1 OFDM modulation scheme

The basic idea of using OFDM as a communication technique is to divide the available bandwidth of transmission into multiple sub-carriers that are mathematically defined to be orthogonal to one another [2, 17]. From Chapter 2, it is understood that flat fading occurs when the transmission bandwidth is smaller than the coherence bandwidth. When applied to the context of OFDM, having a sub-carrier bandwidth that is less than the coherence bandwidth simplifies channel equalization to a one-tap equalizer in the frequency domain. However, the more sub-carriers there are, the longer the symbol length will be. Although this would make the transmission robust towards impulsive noise, the symbol length should also ideally be much less than the coherence time of the channel.

To perform OFDM for transmission and reception, the Inverse Discrete Fourier Transform (IDFT) and Discrete Fourier Transform (DFT) are used respectively. Let N be the number of sub-carriers in an OFDM symbol, and D_k be the data symbol modulated on

sub-carrier k, $k \in [0, N\text{-}1]$. The discrete-time domain samples u_n that constitute an OFDM symbol via IDFT is:

$$u_n = \frac{1}{N}\sum_{k=0}^{N-1} D_k e^{j2\pi kn/N} \quad n \in [0, N-1] \tag{3.8}$$

and reconstruction to obtain the data symbols via DFT is:

$$D_k = \sum_{n=0}^{N-1} u_n e^{-j2\pi kn/N} \tag{3.9}$$

3.2.2 Cyclic Prefix

To overcome ISI arising from multipath channels, a cyclic prefix comprising of the last N_p discrete-time domain samples is attached to the start of the OFDM symbol, maintaining orthogonality within the sub-carriers whilst negating the effects of ISI. The length of the cyclic prefix is dependent on the delay spread of the channel. Evidently, long cyclic prefixes results in lower bandwidth efficiency as the data symbols are transmitted at a lower rate. Upon demodulation, the cyclic prefix is removed and DFT is performed on the remaining OFDM symbol.

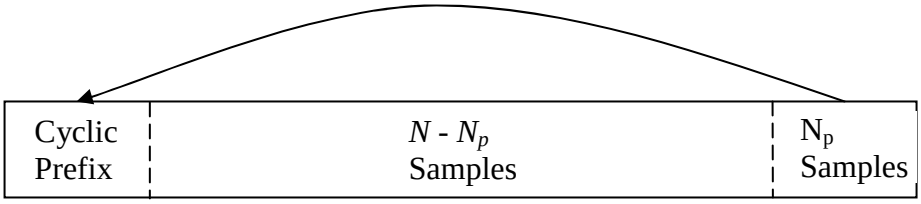

Figure 3.1: Illustration of cyclic prefix in OFDM symbol

3.2.3 Data Modulation Scheme

Two different types of data modulation schemes are employed in this thesis: Quadrature Phase Shift Keying (QPSK) and Differential QPSK (DQPSK) [30].

In QPSK, pilot data symbols are used to first equalize the individual OFDM sub-carriers for distortions in phase and/or amplitude before determining the data symbols D_k which are valid in the dictionary set (for QPSK, the size of this set is 4). This process involves the multiplication of a single-tap equalizer ω_k, $k \in [0, N\text{-}1]$ to the *received* data symbol $\overline{D}_k$, which is usually corrupted by noise and distorted in phase. During equalization mode using pilot symbols, ω_k is first obtained using:

$$\omega_k = \frac{D_k}{\overline{D}_k} \tag{3.10}$$

Subsequent updates with any pilot symbols are weighted with a coefficient so as to reduce the impact of noise on the equalizers. In addition, the average angle of rotation of the data constellation is compensated for:

$$\hat{\omega}_k = \frac{D_k}{\overline{D}_k} \tag{3.11}$$

$$\phi = \frac{\beta_\phi}{N} \sum_{k=0}^{N-1} \angle(\hat{\omega}_k, \omega_k) \qquad 0 < \beta_\phi \leq 1 \tag{3.12}$$

$$\omega_k = \beta_\omega e^{j\phi} \omega_{k-1} + (1 - \beta_\omega)\hat{\omega}_k \quad 0 < \beta_\omega \leq 1 \tag{3.13}$$

β_ϕ and β_ω are the update coefficients for the angle of rotation and equalizer tap respectively. This allows for the equalizer taps to accurately track rapidly rotating constellations due to timing mismatches. Evidently, more sub-carriers will result in a better estimate of the rotation in data constellation. When determining the data symbols, Eqs. (3.11) to (3.13) are still applicable, except that a smaller value for β_ω is applied to minimise decision errors. The equalized received data symbol is then placed through a slicer; the symbol in the dictionary set that yields the minimum distance to this symbol is considered as the intended symbol transmitted at the source:

$$D_k = slicer(\omega_k \overline{D}_k) \tag{3.14}$$

In DQPSK, equalization is comparatively easier and requires in theory one pilot symbol to be first transmitted followed by the data symbols. Let $n \in \mathbf{Z}^+$ represent the time instance of the data symbol. Evidently, $\overline{D}_{k,0}$ represents the received pilot symbol that is mapped onto $D_{k,0}$. Subsequent data symbols that are received can be determined based on the difference in phase:

$$\phi = \angle\left(\overline{D}_{k,n}, \overline{D}_{k,n-1}\right) \tag{3.15}$$

$$D_{k,n} = slicer(D_{k,n-1} e^{j\phi}) \tag{3.16}$$

As a result, errors can be propagated easily to subsequent received symbols.

To minimize errors for both QPSK and DQPSK, the constellation mappings should be based upon Gray codes.

3.2.4 Signal Processing Per Symbol Basis and Per Frame Basis

Within a known duration of time, multiple OFDM symbols can and may be transmitted. Often, the number of symbols is fixed and the symbols are collectively named as a signal frame. The overall structure involving the placement of pilot and data symbols is also known to both the transmitter and receiver.

Compensation techniques like CFO compensation for example are normally based on maximum likelihood (ML) [9] or minimum mean square error (MSE) methods. These techniques can be applied on a per symbol basis or on the totality of the frame. While compensation by symbols is easier to implement, compensation by frames can yield better results by averaging the errors over several symbols in the context of a quasi-stationary channel condition.

3.3 Doppler Compensation Techniques

3.3.1 CFO Compensation using OFDM CP

OFDM is known to be highly vulnerable to CFO, which leads to inter-carrier interference (ICI) as the DFT is not done at the point of orthogonality between sub-carriers [17]. The orthogonal structure is destroyed by mobility between transmitter and receiver. Taking Eqs. (3.5) and (3.8), let us assume without a loss in generality a sampling interval $T_s = 1$:

$$r(n) = \frac{a}{N} e^{j2\pi f_c \Delta n} e^{j2\pi f_c \tau} \sum_{k=0}^{N-1} D_k e^{j2\pi k(1+\Delta)n/N} \qquad n \in [0, N-1] \tag{3.17}$$

and in vector notation:

$$\begin{aligned}
&\mathbf{r} = [r(0) \quad \ldots \quad r(N-1)]^T \\
&\mathbf{d}(\Delta) = [D_0 \quad \ldots \quad D_{N-1}]^T \\
&\mathbf{C}(\Delta) = diag\left(1 \quad e^{j2\pi f_c \Delta} \quad \ldots \quad e^{j2\pi f_c \Delta (N-1)}\right) \\
&\mathbf{W}(\Delta) = \begin{bmatrix} w^0 & \cdots & \cdots & w^0 \\ w^1 & \ddots & \cdots & w^{N-1} \\ \vdots & \vdots & \ddots & \vdots \\ w^{N-1} & \cdots & \cdots & w^{(N-1)(N-1)} \end{bmatrix} \qquad w = e^{j2\pi(1+\Delta)/N} \\
&\mathbf{r}(\Delta) = \frac{a e^{j2\pi f_c \tau}}{N} \mathbf{C}(\Delta)\mathbf{W}(\Delta)\mathbf{d}(\Delta)
\end{aligned} \tag{3.18}$$

Except for integer values of Δ, $\mathbf{W}(\Delta)$ is no longer an orthonormal matrix and cannot be made unitary via the conjugate transpose of $\mathbf{W}$ [12]. If, however, the value of Δ is negligible, then $\mathbf{W^H W} \approx \mathbf{I}$. ICI can be considered to be negligible in this case. Compensation is done to render $\mathbf{C}(\Delta)$ unitary, which is trivial should the value of Δ be known since it is a diagonal matrix.

CFO compensation is performed using the cyclic prefix correlation of OFDM symbols to estimate Δ [44]. However, since the UWA channel has impulsive ambient noise, this ML estimation would not be appropriate. Instead, the cyclic prefix correlation is averaged over the energy of the received signal equivalent to the length of cyclic prefix [5]:

$$c_{rr}(\tau) = \frac{\sum_{n=0}^{N_p-1} r^*(n-N+\tau)r(n+\tau)}{\sum_{n=0}^{N_p-1} r^*(n+\tau)r(n+\tau)} \tag{3.19}$$

Correlation estimates obtained from multiple OFDM symbols can be combined together to improve the accuracy. Under slow time-varying channel assumption, the absolute peak value of $c_{rr}(t)$ at the point of cyclic prefix correlation would be very close to 1. Due to ambient impulsive noise, a margin of 0.8 to 1.1 is imposed upon this peak value to be considered as an acceptable estimate. Assuming that there are N_{sym} symbols in a frame and that any drift in clock synchronization does not lead to a slippage of more than one baseband sample, then from Eq. (3.19) we derive:

$$\begin{aligned} c_{rr}(\tau,m) &= \begin{cases} c_{rr}(\tau+m(N+N_p)) & if\ 0.8 \le \max\left(c_{rr}(\tau+n(N+N_p))\right) \le 1.1 \\ 0 & otherwise \end{cases} \\ c_{rr}^{'}(\tau) &= \sum_{m=0}^{N_{sym}-1} c_{rr}(\tau,m) \end{aligned} \tag{3.20}$$

To obtain the estimated value of Δ, the phase is measured at the point of maximum correlation taken from $c_{rr}(\tau)$ of each symbol or from $c_{rr}^{'}(\tau)$ of the signal frame:

$$\begin{aligned} \hat{\Delta} &= \frac{\angle \max\left(c_{rr}(\tau)\right)}{2\pi f_c T_s N} \\ \hat{\Delta} &= \frac{\angle \max\left(c_{rr}^{'}(\tau)\right)}{2\pi f_c T_s N} \end{aligned} \tag{3.21}$$

It is to be noted, however, that the range of CFO compensation using this technique is limited over the phase of -π to π. Hence, the range for $\hat{\Delta}$ using OFDM cyclic prefix is:

$$\frac{-1}{2 f_c T_s N} \leq \hat{\Delta} \leq \frac{1}{2 f_c T_s N} \tag{3.22}$$

3.3.2 Interpolation

Using interpolation as a method of wideband Doppler compensation was first proposed in [23]. The accuracy of the resulting interpolants with respect to the original transmitted signal depends on the sampling rate and the type of interpolation applied to the signal [9, 11]. Ideally, the sine cardinal* filter would allow for perfect recovery of the interpolants; however, this filter is non-causal and has an infinite impulse response. Instead, 3 types of interpolators are proposed: linear, cubic and parabolic. Parabolic and cubic interpolators incur a higher computational complexity compared to the linear interpolator, but produce less distortion [9].

In this thesis, linear interpolation is chosen as the mode of Doppler compensation for its ease of implementation. In general, interpolation can correct drifts due to synchronization errors in the transmitter and receiver clock, which is taken to be a general mistiming error of Δ. The algorithm accounts for both positive and negative mistiming errors. An accumulator *acc* is used to keep track of the sample positions from which the interpolants *y(n)* are obtained. Once the accumulator exceeds or is equal to 1 (we assume that Δ takes on values less than 1), the counter will be adjusted in accordance to the sign of Δ.

---

* The sine cardinal function is defined as $\text{sinc}(x) = \frac{\sin x}{x}$

Linear interpolation algorithm

Given a discrete signal x*(n), n ∈ [1, N], n ∈ Z*

cond := sign(Δ)

counter := 2 – cond

y(1) := x(1)

n := 2

acc := abs(Δ)

while *counter < N*

    *y(n) := (1-acc)*x(counter+cond) + x(counter)*

    increment *n*

    increment *counter*

    acc := acc + abs(Δ)

    if *acc >= 1*

        acc:= acc – 1

        counter := counter – cond

    end

end

3.3.3 Null Sub-carrier Maximum Likelihood (ML) Estimation

A ML estimator has been derived in [33] involving the strategic placement of null sub-carriers in OFDM. The minimum number of active[*] sub-carriers that can be used is determined by the delay spread of the channel. Although the mean square error (MSE) of the estimates was low, the high computational complexity involved puts this method at a disadvantage over other methods. In addition, the ML estimator assumes a Gaussian noise model with finite variance, which is not applicable in this UWA channel model. Hence, the estimate would be at best sub-optimal in SαS noise. For these reasons, this method was not chosen to be tested.

[*] This refers to sub-carriers containing data and/or pilot symbols. Sub-carriers may be null in OFDM.

3.4 Doppler Acquisition Techniques

3.4.1 Iterative Interpolation method

In order to apply the Doppler compensation algorithm, mobility induced Doppler must first be estimated. Kim and Lu [15] proposed a method based on an iterative approach towards interpolation to determine the compensated sampling interval required under mobility. Based upon OFDM using the correlation of the cyclic prefix [9], the time interval between the two peaks as well as the phase offset at the second peak is used to determine a new sampling interval to be applied.

Iterative Interpolation Algorithm*

1. Guess an initial sampling interval $T_{s,est}$
2. Find the peak cyclic prefix correlation ξ_{peak} and the phase at that point ϕ_{peak}
3. Estimate timing error Δ using:

   $\xi_{peak} = NT_s / [(1 + \Delta)T_{s,est}]$

   $\phi_{peak} = -2\pi [(1 + \Delta)T_s - T_{s,est}] \xi_{peak} f_c$

   where N is the number of sub-carriers, f_c is the carrier frequency and T_s is the original sampling interval
4. If $\xi_{peak} \approx N$ and $\phi_{peak} \approx 0$, terminate the iteration
5. determine a new sampling interval using $T_{s,est} = T_s / (1 + \Delta)$
6. Repeat steps 1 to 5.

3.4.2 Linear Frequency Modulated (LFM) Signal

LFM signals, or commonly known as chirp signals, are mathematically defined as:

$$x(t) = \cos\left(2\pi f_0 t + \pi k t^2\right) \tag{3.23}$$

The instantaneous frequency can be obtained via differentiation:

* The algorithm has been reproduced from [25] for cross-reference purposes

$$f(t) = \frac{1}{2\pi}\frac{d}{dt}\left(2\pi f_0 t + \pi k t^2\right) = f_0 t + kt \tag{3.24}$$

Thus, the start frequency f_0, a stop frequency f_1 and the time duration of transmission T_{LFM} are all that is required to characterise a chirp signal:

$$|k| = \frac{|f_0 - f_1|}{T_{LFM}} = \frac{B_{LFM}}{T_{LFM}} \tag{3.25}$$

where B_{LFM} is the bandwidth of the chirp signal [31].

The ambiguity function shows the matched filter response against delay and Doppler shift variations of the incoming signal. For a wide-band continuous time signal, the definition of the ambiguity function is given as:

$$\chi_s(\tau, \Delta) = (1+\Delta)\int_{-\infty}^{\infty} s((1+\Delta)t)s(t-\tau)dt \tag{3.26}$$

For LFM signals, the main ridge of the ambiguity function lies along the axis of correlation delay (τ) as a function of the fractional Doppler shift Δ [18]:

$$\tau(\Delta) = \frac{T}{B}\frac{\Delta}{(1-\Delta)}\left[\frac{f_0}{1-\Delta} - \frac{\Delta f_1}{1+\Delta}\right] \tag{3.27}$$

At realistic levels of Doppler shifts ($\Delta < 0.01$), the delay can be considered to vary linearly with Doppler.

From the ambiguity function in Eq. (3.26), a bank of discrete correlators replicating the LFM signal at different values of Doppler shift can be used to estimate Δ. However, the number of filters required would be significant should the expected velocity range be wide or should the required resolution of estimation be important. Instead, two LFM waveforms are interleaved in the signal frame and detected via matched filtering using a single correlator [34].

From Figure 3.2, the duration T_{rp} between the measured peaks of the received signal varies due to expansion / compression of the signal frame under the influence of Doppler. Thus, by using the original duration T_{tp} between the LFM waveforms, the fractional Doppler shift can be estimated as [34]:

$$\hat{\Delta} = \frac{T_{rp}}{T_{tp}} - 1 \tag{3.28}$$

The resolution of $\hat{\Delta}$ depends not only on the duration T_{tp} between LFM signals, but also B_{LFM} as well as the sampling rate used.

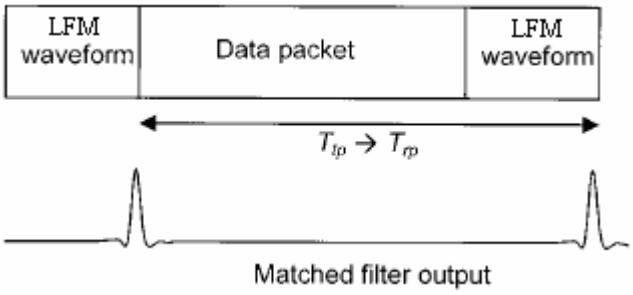

Figure 3.2*: Illustration of match filtering with LFM waveforms

3.5 Simulation Tests

3.5.1 Simulation Parameters

To standardise the tests conducted in this section, the channel as well as signal parameters used are identical so as to have a fair basis for comparison. The channel parameters used are considerably less "severe" than those expected from an UWA channel: each individual path arrival undergoes Rayleigh fading that is constant over the signal frame duration; in addition, channel delay spread is less than the OFDM CP length. Since none of these assumptions are imposed prior to deriving the different Doppler

* The figure has been reproduced from [23] for cross-reference purposes

compensation methods, the validity and suitability of the various methods should not be affected.

In all the tests, QPSK is applied upon the data symbols. Also, *perfect timing synchronization* is assumed in locating the start of frame. For tests that require the usage of LFM signals, the bandwidth B_{LFM} is assumed to be equal to that of the OFDM signal B_s. The results obtained for each test are averaged over 1000 Monte Carlo trials.

Table 3.1: Simulation parameters for analysing Doppler effects.

Channel Parameters		
Ambient noise type	SαS; α = 1.7	
SNR range	0 to 30 dB	
Channel type	Dispersive, non time-varying.	
Fading type	Rayleigh distributed for each individual path	
Propagation speed	1500 m/s	
Velocity range	-5 to 5 m/s	
Signal Parameters		
Carrier frequency	f_c	50 kHz
Signal bandwidth	B_s , B_{LFM}	20 kHz
LFM duration	T_{LFM}	1 ms
Number of OFDM symbols	N_b	8
Number of OFDM pilots	N_{pilot}	4
Number of OFDM sub-carriers	N	128
OFDM cyclic prefix length	N_p	32

3.5.2 Simulation Test 3.1

This initial test analyses the robustness of Doppler acquisition using LFM signals as well as the sensitivity of wideband OFDM to CFO. We assume here that Doppler spread is insignificant compared to Doppler shift, hence only CFO compensation is performed upon the received time dilated / constricted signals due to mobility.

LFM	NULL	LFM	4 OFDM pilots	4 OFDM data

Figure 3.3: Signal frame structure for Test 3.2

Figure 3.3 shows the structure of the transmitted signal. A null period of 5ms is implemented between the LFM signals to prevent reverberations from affecting the estimation of the second correlation peak. CFO compensation is done in 2 steps:

1) Initial Doppler shift estimate $\hat{\Delta}_1$ is obtained using Eq. (3.28) and compensated for in passband before low-pass filtering the signal to baseband.
2) Each baseband OFDM symbol is individually compensated for using the OFDM cyclic prefix. The estimate $\hat{\Delta}_2$ represents the average Doppler shift obtained from the cyclic prefixes of all the OFDM symbols.

At a sampling rate of f_s = 160kHz, it is observed from Table 3.2 that the first estimate $\hat{\Delta}_1$ is stratified over different ranges of velocity, yielding similar results for different velocities. This result is not surprising as this method of estimation is dependent on the duration between the LFM signals as well as *sampling rate* applied. Also, $\hat{\Delta}_1$ is observed to over-estimate the actual value of Doppler shift.

From Table 3.3, we find that $\hat{\Delta}_2$ is able to improve the overall Doppler shift estimate. The figures in red represents a residual MSE ε for which the value is higher than that of the MSE obtained using only $\hat{\Delta}_1$. At velocities of 0.5m/s, 2.0m/s and 2.5m/s, $\sqrt{\varepsilon}$ is of the same order (10^{-3}) if not higher than that of the actual Doppler shift Δ. This is due to the fact that the initial estimates $\hat{\Delta}_1$ are not precise enough to limit the residual CFO within the value of $-\pi$ and π.

Table 3.2: Estimated Doppler shift $\hat{\Delta}_1$ from LFM signals at f_s = 160 kHz for Test 3.1

Velocity m/s	Doppler shift Δ	Estimated Doppler shift $\hat{\Delta}_1$ at different ISNR (dB)						
		0	5	10	15	20	25	30
-5.0	$-3.33*10^{-3}$	$-1.89*10^{-3}$	$-2.06*10^{-3}$	$-2.07*10^{-3}$	$-2.07*10^{-3}$	$-2.07*10^{-3}$	$-2.07*10^{-3}$	$-2.07*10^{-3}$
-4.5	$-3.00*10^{-3}$	$-1.93*10^{-3}$	$-2.07*10^{-3}$	$-2.08*10^{-3}$	$-2.07*10^{-3}$	$-2.07*10^{-3}$	$-2.07*10^{-3}$	$-2.07*10^{-3}$
-4.0	$-2.67*10^{-3}$	$-1.92*10^{-3}$	$-2.06*10^{-3}$	$-2.07*10^{-3}$	$-2.07*10^{-3}$	$-2.07*10^{-3}$	$-2.07*10^{-3}$	$-2.07*10^{-3}$
-3.5	$-2.33*10^{-3}$	$-9.32*10^{-4}$	$-1.05*10^{-3}$	$-1.04*10^{-3}$	$-1.04*10^{-3}$	$-1.04*10^{-3}$	$-1.04*10^{-3}$	$-1.04*10^{-3}$
-3.0	$-2.00*10^{-3}$	$-9.57*10^{-4}$	$-1.03*10^{-3}$	$-1.04*10^{-3}$	$-1.04*10^{-3}$	$-1.04*10^{-3}$	$-1.04*10^{-3}$	$-1.04*10^{-3}$
-2.5	$-1.67*10^{-3}$	$-9.56*10^{-4}$	$-1.03*10^{-3}$	$-1.04*10^{-3}$	$-1.04*10^{-3}$	$-1.04*10^{-3}$	$-1.04*10^{-3}$	$-1.04*10^{-3}$
-2.0	$-1.33*10^{-3}$	$-9.41*10^{-4}$	$-1.03*10^{-3}$	$-1.04*10^{-3}$	$-1.04*10^{-3}$	$-1.04*10^{-3}$	$-1.04*10^{-3}$	$-1.04*10^{-3}$
-1.5	$-1.00*10^{-3}$	$-6.43*10^{-5}$	$-2.06*10^{-6}$	0	0	0	0	0
-1.0	$-6.67*10^{-4}$	$-1.13*10^{-4}$	$-1.60*10^{-5}$	0	0	0	0	0
-0.5	$-3.33*10^{-4}$	$-9.22*10^{-5}$	$-9.96*10^{-6}$	0	0	0	0	0
0	0	$-1.27*10^{-4}$	$-1.64*10^{-5}$	0	0	0	0	0
0.5	$3.33*10^{-4}$	$1.86*10^{-3}$	$2.08*10^{-3}$	$2.08*10^{-3}$	$2.08*10^{-3}$	$2.08*10^{-3}$	$2.08*10^{-3}$	$2.08*10^{-3}$
1.0	$6.67*10^{-4}$	$1.84*10^{-3}$	$2.08*10^{-3}$	$2.08*10^{-3}$	$2.08*10^{-3}$	$2.08*10^{-3}$	$2.08*10^{-3}$	$2.08*10^{-3}$
1.5	$1.00*10^{-3}$	$1.86*10^{-3}$	$2.08*10^{-3}$	$2.08*10^{-3}$	$2.08*10^{-3}$	$2.08*10^{-3}$	$2.08*10^{-3}$	$2.08*10^{-3}$
2.0	$1.33*10^{-3}$	$2.81*10^{-3}$	$3.10*10^{-3}$	$3.13*10^{-3}$	$3.13*10^{-3}$	$3.13*10^{-3}$	$3.13*10^{-3}$	$3.13*10^{-3}$
2.5	$1.67*10^{-3}$	$2.76*10^{-3}$	$3.12*10^{-3}$	$3.13*10^{-3}$	$3.13*10^{-3}$	$3.13*10^{-3}$	$3.13*10^{-3}$	$3.13*10^{-3}$
3.0	$2.00*10^{-3}$	$2.75*10^{-3}$	$3.12*10^{-3}$	$3.13*10^{-3}$	$3.13*10^{-3}$	$3.13*10^{-3}$	$3.13*10^{-3}$	$3.13*10^{-3}$
3.5	$2.33*10^{-3}$	$2.76*10^{-3}$	$3.12*10^{-3}$	$3.13*10^{-3}$	$3.13*10^{-3}$	$3.13*10^{-3}$	$3.13*10^{-3}$	$3.13*10^{-3}$
4.0	$2.67*10^{-3}$	$3.04*10^{-3}$	$3.32*10^{-3}$	$3.33*10^{-3}$	$3.33*10^{-3}$	$3.33*10^{-3}$	$3.33*10^{-3}$	$3.33*10^{-3}$
4.5	$3.00*10^{-3}$	$3.06*10^{-3}$	$3.32*10^{-3}$	$3.33*10^{-3}$	$3.33*10^{-3}$	$3.33*10^{-3}$	$3.33*10^{-3}$	$3.33*10^{-3}$
5.0	$3.33*10^{-3}$	$3.04*10^{-3}$	$3.33*10^{-3}$	$3.33*10^{-3}$	$3.33*10^{-3}$	$3.33*10^{-3}$	$3.33*10^{-3}$	$3.33*10^{-3}$

Table 3.3: MSE ε from overall Doppler acquisition at f_s = 160 kHz for Test 3.1.

Velocity m/s	Doppler MSE $\varepsilon = \left(\Delta - \hat{\Delta}_1 - \hat{\Delta}_2\right)^2$ at different ISNR (dB)						
	0	5	10	15	20	25	30
-5.0	$2.70*10^{-7}$	$5.90*10^{-8}$	$4.16*10^{-8}$	$4.20*10^{-8}$	$4.16*10^{-8}$	$4.20*10^{-8}$	$4.20*10^{-8}$
-4.5	$1.88*10^{-7}$	$4.28*10^{-8}$	$3.28*10^{-8}$	$3.28*10^{-8}$	$3.28*10^{-8}$	$3.28*10^{-8}$	$3.28*10^{-8}$
-4.0	$1.58*10^{-7}$	$3.06*10^{-8}$	$2.53*10^{-8}$	$2.53*10^{-8}$	$2.53*10^{-8}$	$2.53*10^{-8}$	$2.53*10^{-8}$
-3.5	$2.39*10^{-7}$	$2.79*10^{-8}$	$1.88*10^{-8}$	$1.88*10^{-8}$	$1.88*10^{-8}$	$1.88*10^{-8}$	$1.88*10^{-8}$
-3.0	$1.25*10^{-7}$	$1.90*10^{-8}$	$1.35*10^{-8}$	$1.37*10^{-8}$	$1.35*10^{-8}$	$1.35*10^{-8}$	$1.35*10^{-8}$
-2.5	$5.06*10^{-8}$	$1.21*10^{-8}$	$9.16*10^{-9}$	$9.20*10^{-9}$	$9.18*10^{-9}$	$9.24*10^{-9}$	$9.20*10^{-9}$
-2.0	$2.22*10^{-8}$	$7.23*10^{-9}$	$5.75*10^{-9}$	$5.82*10^{-9}$	$5.78*10^{-9}$	$5.76*10^{-9}$	$5.76*10^{-9}$
-1.5	$4.00*10^{-10}$	$3.65*10^{-9}$	$3.06*10^{-9}$	$3.06*10^{-9}$	$3.06*10^{-9}$	$3.07*10^{-9}$	$3.05*10^{-9}$
-1.0	$4.34*10^{-9}$	$4.20*10^{-10}$	$1.27*10^{-9}$	$1.30*10^{-9}$	$1.27*10^{-9}$	$1.28*10^{-9}$	$1.28*10^{-9}$
-0.5	$5.01*10^{-9}$	$5.11*10^{-11}$	$2.62*10^{-10}$	$2.96*10^{-10}$	$2.62*10^{-10}$	$2.76*10^{-10}$	$2.72*10^{-10}$
0	$1.37*10^{-8}$	$3.92*10^{-10}$	$4.62*10^{-12}$	$1.03*10^{-11}$	$1.03*10^{-11}$	$8.18*10^{-12}$	$7.90*10^{-12}$
0.5	$7.24*10^{-6}$	$9.30*10^{-6}$	$9.61*10^{-6}$	$9.61*10^{-6}$	$9.61*10^{-6}$	$9.61*10^{-6}$	$9.61*10^{-6}$
1.0	$1.99*10^{-8}$	$1.96*10^{-8}$	$9.18*10^{-10}$	$6.25*10^{-10}$	$1.54*10^{-10}$	$2.46*10^{-10}$	$1.56*10^{-10}$
1.5	$2.10*10^{-8}$	$2.17*10^{-9}$	$3.67*10^{-9}$	$3.70*10^{-9}$	$3.65*10^{-9}$	$3.67*10^{-9}$	$3.66*10^{-9}$
2.0	$4.84*10^{-6}$	$6.40*10^{-6}$	$6.55*10^{-6}$	$6.55*10^{-6}$	$6.55*10^{-6}$	$6.55*10^{-6}$	$6.55*10^{-6}$
2.5	$3.42*10^{-7}$	$8.72*10^{-7}$	$8.41*10^{-7}$	$9.49*10^{-7}$	$8.85*10^{-7}$	$9.31*10^{-7}$	$9.41*10^{-7}$
3.0	$1.92*10^{-7}$	$1.61*10^{-8}$	$1.51*10^{-8}$	$1.51*10^{-8}$	$1.54*10^{-8}$	$1.54*10^{-8}$	$1.54*10^{-8}$
3.5	$2.34*10^{-7}$	$2.46*10^{-8}$	$2.13*10^{-8}$	$2.16*10^{-8}$	$2.13*10^{-8}$	$2.13*10^{-8}$	$2.13*10^{-8}$
4.0	$1.81*10^{-7}$	$3.06*10^{-8}$	$2.86*10^{-8}$	$2.82*10^{-8}$	$2.82*10^{-8}$	$2.82*10^{-8}$	$2.82*10^{-8}$
4.5	$2.16*10^{-7}$	$4.00*10^{-8}$	$3.69*10^{-8}$	$3.69*10^{-8}$	$3.69*10^{-8}$	$3.69*10^{-8}$	$3.69*10^{-8}$
5.0	$2.69*10^{-7}$	$5.06*10^{-8}$	$4.75*10^{-8}$	$4.75*10^{-8}$	$4.75*10^{-8}$	$4.75*10^{-8}$	$4.75*10^{-8}$

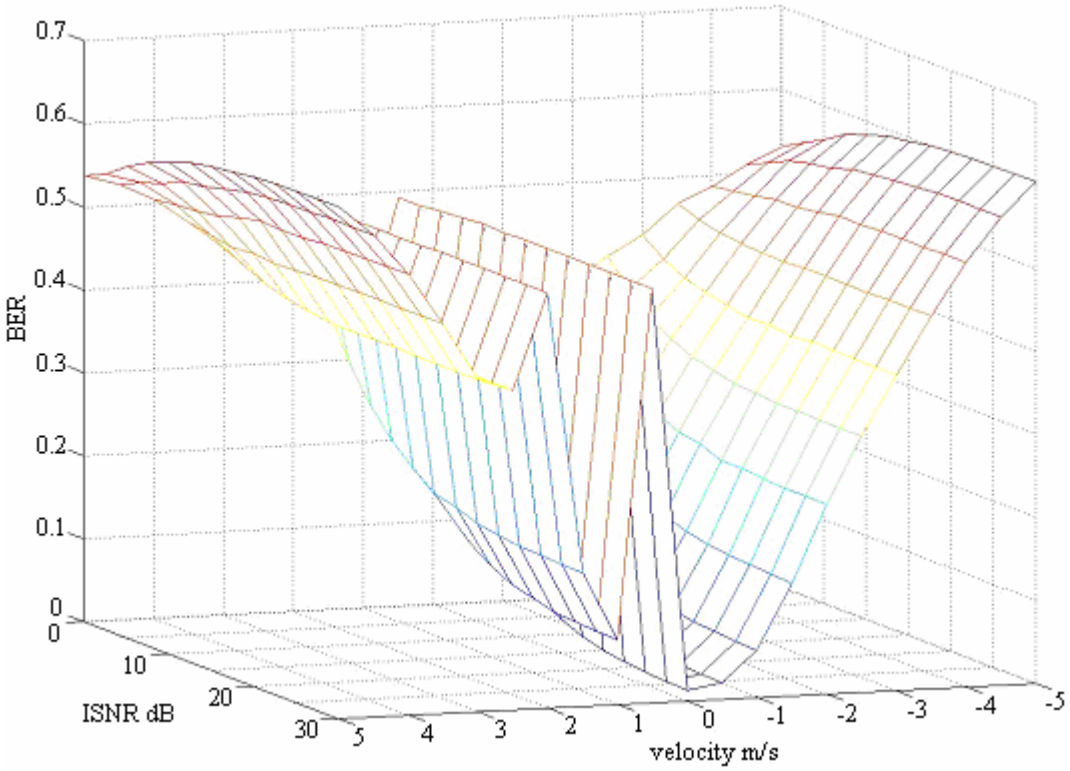

Figure 3.4: BER under varying ISNR and velocity at f_s=160 kHz for Test 3.1

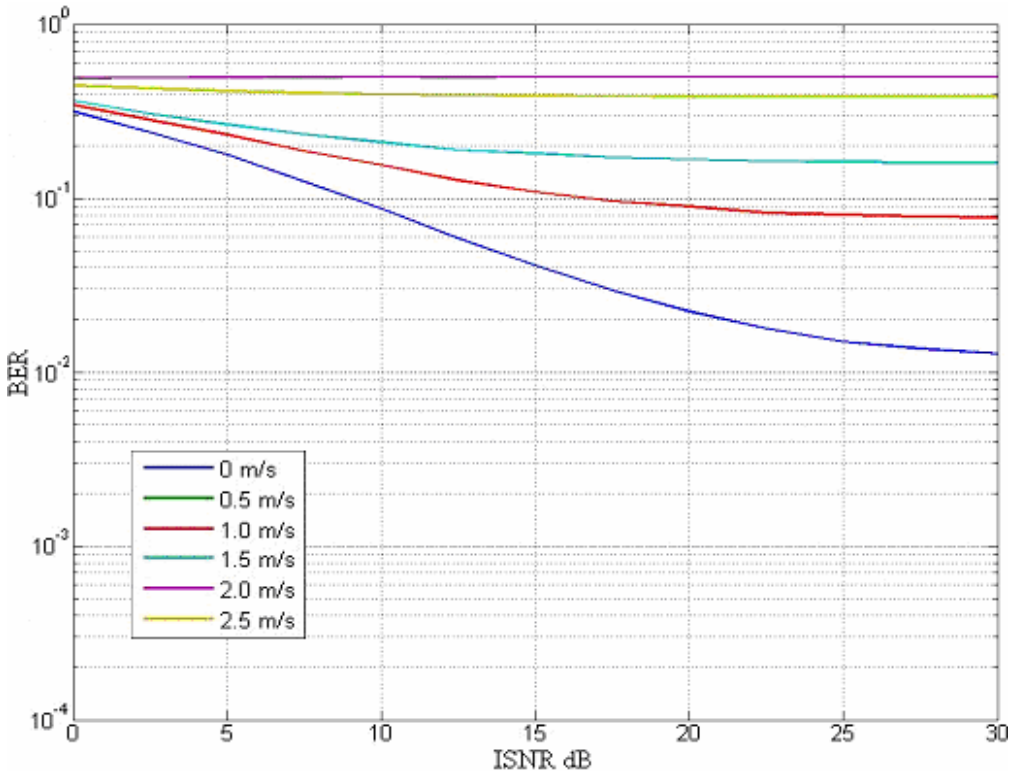

Figure 3.5: BER under varying ISNR and selected velocities at f_s=160 kHz for Test 3.1

Figure 3.4 shows irreducible BER across different ISNR for the 3 velocities of high residual error (0.5, 2.0 and 2.5 m/s). Compared to Test 3.4, the severity of both Doppler shift and Doppler spread is evident in this case; the former is characterised by high irreducible BER with increasing SNR whereas the latter is noticed in poorer BER at augmented speeds. A noticeable phenomenon at ±5m/s is an increment of BER to a ceiling with increasing ISNR. This is due to a rapidly rotating constellation of which the equalizer taps are unable to keep track, resulting in a bias on the decision from the slicer.

Figure 3.5 shows the BER performance for velocities between 0m/s to 2.5m/s. The disparity in performance due to mobility can be seen from low ISNR of 5 dB. The BER at 0 m/s approaches a threshold at higher ISNR due to imprecision in estimation of CFO via the OFDM cyclic prefix. As a result, while a BER performance of $<10^{-3}$ was attainable in the previous test at 30 dB, the results here show BER that cannot surmount 10^{-2}.

In order to improve the accuracy obtain from $\hat{\Delta}_1$, the timing resolution is increased by applying a sampling rate of f_s = 640 kHz. Table 3.4 shows the initial estimated Doppler shift obtained from the LFM signals. The values are no longer stratified across similar bands and have smaller errors. The figures in red represent estimates yielding higher MSE compared to those at f_s = 160 kHz.

Table 3.5 shows the MSE after applying the second step of CFO compensation vis-à-vis the OFDM cyclic prefixes. The values in red represent absolute errors in estimation that are higher than those arising from the initial estimate $\hat{\Delta}_1$. As the residual Doppler MSE resulting after $\hat{\Delta}_1$ are well within the bounds defined by Eq. (3.22), excessively high errors were avoided after CFO compensation from $\hat{\Delta}_2$.

Table 3.4: Estimated Doppler shift $\hat{\Delta}_1$ from LFM signals at f_s = 640 kHz for Test 3.1.

Velocity m/s	Doppler shift Δ	Estimated Doppler shift $\hat{\Delta}_1$ at different ISNR (dB)						
		0	5	10	15	20	25	30
-5.0	$-3.33*10^{-3}$	$-2.63*10^{-3}$	$-2.98*10^{-3}$	$-3.11*10^{-3}$	$-3.11*10^{-3}$	$-3.11*10^{-3}$	$-3.11*10^{-3}$	$-3.11*10^{-3}$
-4.5	$-3.00*10^{-3}$	$-2.16*10^{-3}$	$-2.48*10^{-3}$	$-2.58*10^{-3}$	$-2.60*10^{-3}$	$-2.60*10^{-3}$	$-2.60*10^{-3}$	$-2.60*10^{-3}$
-4.0	$-2.67*10^{-3}$	$-1.89*10^{-3}$	$-2.28*10^{-3}$	$-2.33*10^{-3}$	$-2.34*10^{-3}$	$-2.34*10^{-3}$	$-2.34*10^{-3}$	$-2.34*10^{-3}$
-3.5	$-2.33*10^{-3}$	$-1.75*10^{-3}$	$-1.99*10^{-3}$	$-2.07*10^{-3}$	$-2.07*10^{-3}$	$-2.08*10^{-3}$	$-2.08*10^{-3}$	$-2.08*10^{-3}$
-3.0	$-2.00*10^{-3}$	$-1.62*10^{-3}$	$-1.70*10^{-3}$	$-1.82*10^{-3}$	$-1.82*10^{-3}$	$-1.82*10^{-3}$	$-1.82*10^{-3}$	$-1.82*10^{-3}$
-2.5	$-1.67*10^{-3}$	$-1.39*10^{-3}$	$-1.49*10^{-3}$	$-1.55*10^{-3}$	$-1.56*10^{-3}$	$-1.56*10^{-3}$	$-1.56*10^{-3}$	$-1.56*10^{-3}$
-2.0	$-1.33*10^{-3}$	$-9.42*10^{-4}$	$-9.51*10^{-4}$	$-1.03*10^{-3}$	$-1.04*10^{-3}$	$-1.04*10^{-3}$	$-1.04*10^{-3}$	$-1.04*10^{-3}$
-1.5	$-1.00*10^{-3}$	$-7.14*10^{-4}$	$-7.50*10^{-4}$	$-7.75*10^{-4}$	$-7.80*10^{-4}$	$-7.80*10^{-4}$	$-7.80*10^{-4}$	$-7.80*10^{-4}$
-1.0	$-6.67*10^{-4}$	$-5.35*10^{-4}$	$-4.59*10^{-4}$	$-5.02*10^{-4}$	$-5.20*10^{-4}$	$-5.20*10^{-4}$	$-5.20*10^{-4}$	$-5.20*10^{-4}$
-0.5	$-3.33*10^{-4}$	$-2.78*10^{-4}$	$-2.15*10^{-4}$	$-2.42*10^{-4}$	$-2.60*10^{-4}$	$-2.60*10^{-4}$	$-2.60*10^{-4}$	$-2.60*10^{-4}$
0	0	$-1.24*10^{-4}$	$3.14*10^{-5}$	$5.97*10^{-7}$	0	0	0	0
0.5	$3.33*10^{-4}$	$5.25*10^{-4}$	$7.64*10^{-4}$	$7.85*10^{-4}$	$7.81*10^{-4}$	$7.81*10^{-4}$	$7.81*10^{-4}$	$7.81*10^{-4}$
1.0	$6.67*10^{-4}$	$6.99*10^{-4}$	$1.06*10^{-3}$	$1.05*10^{-3}$	$1.04*10^{-3}$	$1.04*10^{-3}$	$1.04*10^{-3}$	$1.04*10^{-3}$
1.5	$1.00*10^{-3}$	$9.40*10^{-4}$	$1.28*10^{-3}$	$1.31*10^{-3}$	$1.30*10^{-3}$	$1.30*10^{-3}$	$1.30*10^{-3}$	$1.30*10^{-3}$
2.0	$1.33*10^{-3}$	$1.10*10^{-3}$	$1.55*10^{-3}$	$1.57*10^{-3}$	$1.56*10^{-3}$	$1.56*10^{-3}$	$1.56*10^{-3}$	$1.56*10^{-3}$
2.5	$1.67*10^{-3}$	$1.46*10^{-3}$	$2.05*10^{-3}$	$2.08*10^{-3}$	$2.09*10^{-3}$	$2.09*10^{-3}$	$2.09*10^{-3}$	$2.09*10^{-3}$
3.0	$2.00*10^{-3}$	$1.66*10^{-3}$	$2.26*10^{-3}$	$2.35*10^{-3}$	$2.35*10^{-3}$	$2.35*10^{-3}$	$2.35*10^{-3}$	$2.35*10^{-3}$
3.5	$2.33*10^{-3}$	$1.92*10^{-3}$	$2.58*10^{-3}$	$2.60*10^{-3}$	$2.61*10^{-3}$	$2.61*10^{-3}$	$2.61*10^{-3}$	$2.61*10^{-3}$
4.0	$2.67*10^{-3}$	$2.11*10^{-3}$	$2.82*10^{-3}$	$2.86*10^{-3}$	$2.87*10^{-3}$	$2.87*10^{-3}$	$2.87*10^{-3}$	$2.87*10^{-3}$
4.5	$3.00*10^{-3}$	$2.30*10^{-3}$	$3.04*10^{-3}$	$3.13*10^{-3}$	$3.13*10^{-3}$	$3.13*10^{-3}$	$3.13*10^{-3}$	$3.13*10^{-3}$
5.0	$3.33*10^{-3}$	$2.78*10^{-3}$	$3.55*10^{-3}$	$3.66*10^{-3}$	$3.66*10^{-3}$	$3.66*10^{-3}$	$3.66*10^{-3}$	$3.66*10^{-3}$

Figure 3.6 shows a typical profile of $\sqrt{\varepsilon}$ obtained at the two different stages of Doppler acquisition. The compressive / expansive influence of mobility upon the received signal limits the accuracy of $\hat{\Delta}_2$ at higher ISNR, resulting in irreducible residual error from 10 dB onwards. It is once again observed from Figure 3.7 and Figure 3.8 that there exists a great disparity in BER performance with augmenting speeds. Figure 3.7 shows a symmetrical BER structure about 0m/s, which means that there is no bias to take into consideration at positive and negative velocities when using OFDM.

We can therefore conclude that compensation for Doppler shift only is insufficient at higher ISNR due to deterioration of the estimates by Doppler spreading. Corrections are to be made before CFO compensation using OFDM cyclic prefix correlation to minimise the influence of Doppler spreading in wideband signals.

Table 3.5: MSE ε from overall Doppler acquisition at f_s = 640 kHz for Test 3.1.

Velocity m/s	Doppler MSE $\varepsilon = \left(\Delta - \hat{\Delta}_1 - \hat{\Delta}_2\right)^2$ at different ISNR (dB)						
	0	5	10	15	20	25	30
-5.0	$4.68*10^{-7}$	$1.02*10^{-7}$	$3.57*10^{-8}$	$3.57*10^{-8}$	$3.61*10^{-8}$	$3.61*10^{-8}$	$3.61*10^{-8}$
-4.5	$4.75*10^{-7}$	$7.56*10^{-8}$	$3.28*10^{-8}$	$2.82*10^{-8}$	$2.82*10^{-8}$	$2.82*10^{-8}$	$2.82*10^{-8}$
-4.0	$4.87*10^{-7}$	$4.67*10^{-8}$	$2.53*10^{-8}$	$2.19*10^{-8}$	$2.19*10^{-8}$	$2.16*10^{-8}$	$2.19*10^{-8}$
-3.5	$3.60*10^{-7}$	$5.11*10^{-8}$	$1.88*10^{-8}$	$1.72*10^{-8}$	$1.64*10^{-8}$	$1.64*10^{-8}$	$1.64*10^{-8}$
-3.0	$2.58*10^{-7}$	$5.76*10^{-8}$	$1.25*10^{-8}$	$1.17*10^{-8}$	$1.19*10^{-8}$	$1.17*10^{-8}$	$1.17*10^{-8}$
-2.5	$8.41*10^{-8}$	$2.07*10^{-8}$	$9.84*10^{-9}$	$7.99*10^{-9}$	$8.05*10^{-9}$	$8.03*10^{-9}$	$8.03*10^{-9}$
-2.0	$2.13*10^{-8}$	$2.22*10^{-8}$	$6.10*10^{-9}$	$5.00*10^{-9}$	$5.01*10^{-9}$	$5.06*10^{-9}$	$5.04*10^{-9}$
-1.5	$6.05*10^{-12}$	$4.12*10^{-9}$	$3.12*10^{-9}$	$2.76*10^{-9}$	$2.77*10^{-9}$	$2.76*10^{-9}$	$2.76*10^{-9}$
-1.0	$6.42*10^{-9}$	$5.10*10^{-9}$	$2.45*10^{-9}$	$1.18*10^{-9}$	$1.16*10^{-9}$	$1.17*10^{-9}$	$1.16*10^{-9}$
-0.5	$2.13*10^{-9}$	$2.52*10^{-9}$	$9.49*10^{-10}$	$2.46*10^{-10}$	$2.50*10^{-10}$	$2.50*10^{-10}$	$2.50*10^{-10}$
0	$1.64*10^{-8}$	$5.57*10^{-10}$	$7.90*10^{-12}$	$5.86*10^{-12}$	$5.38*10^{-12}$	$4.97*10^{-12}$	$5.15*10^{-12}$
0.5	$8.57*10^{-9}$	$2.56*10^{-12}$	$2.16*10^{-10}$	$4.00*10^{-10}$	$4.16*10^{-10}$	$4.12*10^{-10}$	$4.12*10^{-10}$
1.0	$2.02*10^{-8}$	$4.08*10^{-10}$	$5.71*10^{-10}$	$1.47*10^{-9}$	$1.49*10^{-9}$	$1.51*10^{-9}$	$1.49*10^{-9}$
1.5	$3.28*10^{-8}$	$2.34*10^{-9}$	$2.08*10^{-9}$	$3.29*10^{-9}$	$3.28*10^{-9}$	$3.28*10^{-9}$	$3.28*10^{-9}$
2.0	$1.12*10^{-7}$	$4.62*10^{-9}$	$4.64*10^{-9}$	$5.73*10^{-9}$	$5.82*10^{-9}$	$5.81*10^{-9}$	$5.81*10^{-9}$
2.5	$3.35*10^{-7}$	$1.12*10^{-8}$	$1.06*10^{-8}$	$9.22*10^{-9}$	$9.14*10^{-9}$	$9.20*10^{-9}$	$9.14*10^{-9}$
3.0	$7.01*10^{-7}$	$4.93*10^{-8}$	$1.32*10^{-8}$	$1.35*10^{-8}$	$1.35*10^{-8}$	$1.35*10^{-8}$	$1.35*10^{-8}$
3.5	$7.83*10^{-7}$	$3.61*10^{-8}$	$2.04*10^{-8}$	$1.88*10^{-8}$	$1.88*10^{-8}$	$1.88*10^{-8}$	$1.88*10^{-8}$
4.0	$9.12*10^{-7}$	$4.58*10^{-8}$	$2.82*10^{-8}$	$2.50*10^{-8}$	$2.50*10^{-8}$	$2.50*10^{-8}$	$2.50*10^{-8}$
4.5	$9.53*10^{-7}$	$7.08*10^{-8}$	$3.35*10^{-8}$	$3.28*10^{-8}$	$3.24*10^{-8}$	$3.24*10^{-8}$	$3.28*10^{-8}$
5.0	$9.64*10^{-7}$	$8.76*10^{-8}$	$4.16*10^{-8}$	$4.16*10^{-8}$	$4.16*10^{-8}$	$4.16*10^{-8}$	$4.16*10^{-8}$

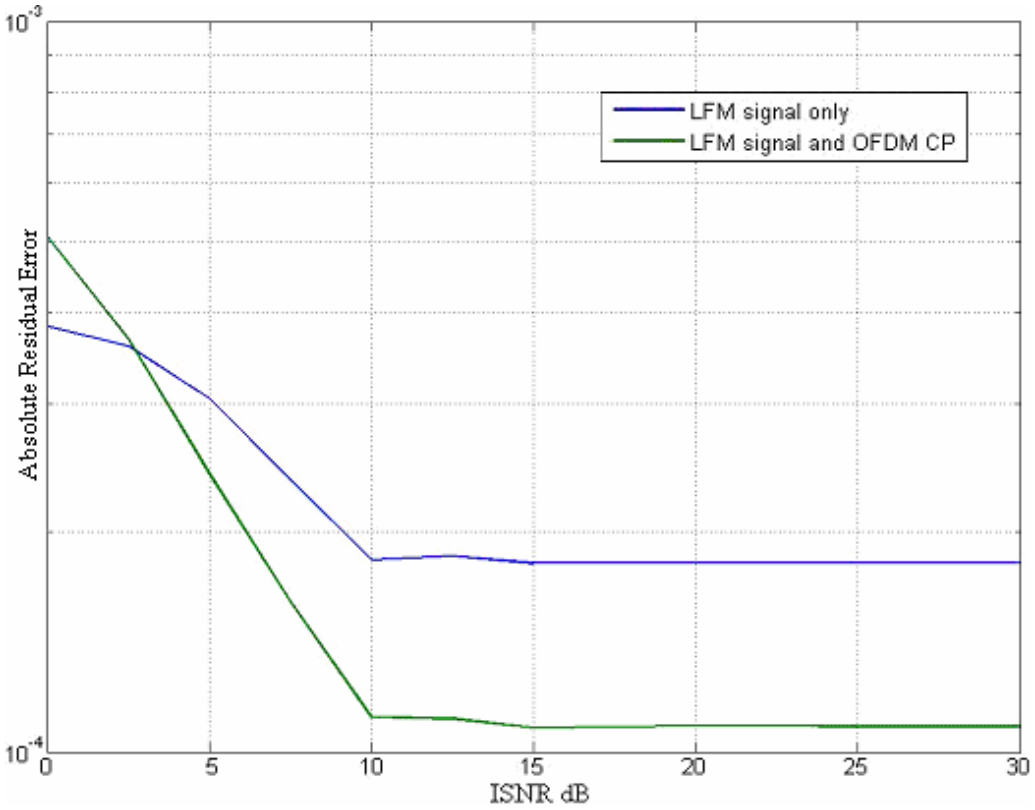

Figure 3.6: Doppler RMS error $\sqrt{\varepsilon}$ in varying ISNR at -3 m/s and f_s=640kHz for Test 3.1

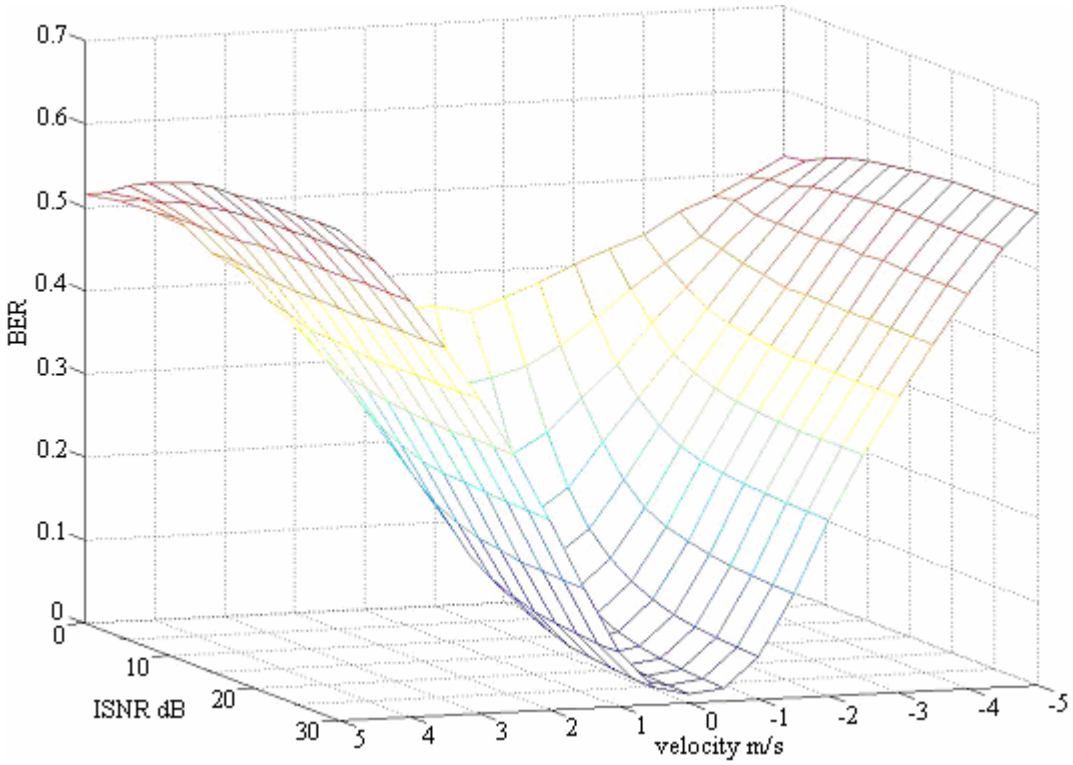

Figure 3.7: BER under varying ISNR and velocity at f_s=640 kHz for Test 3.1

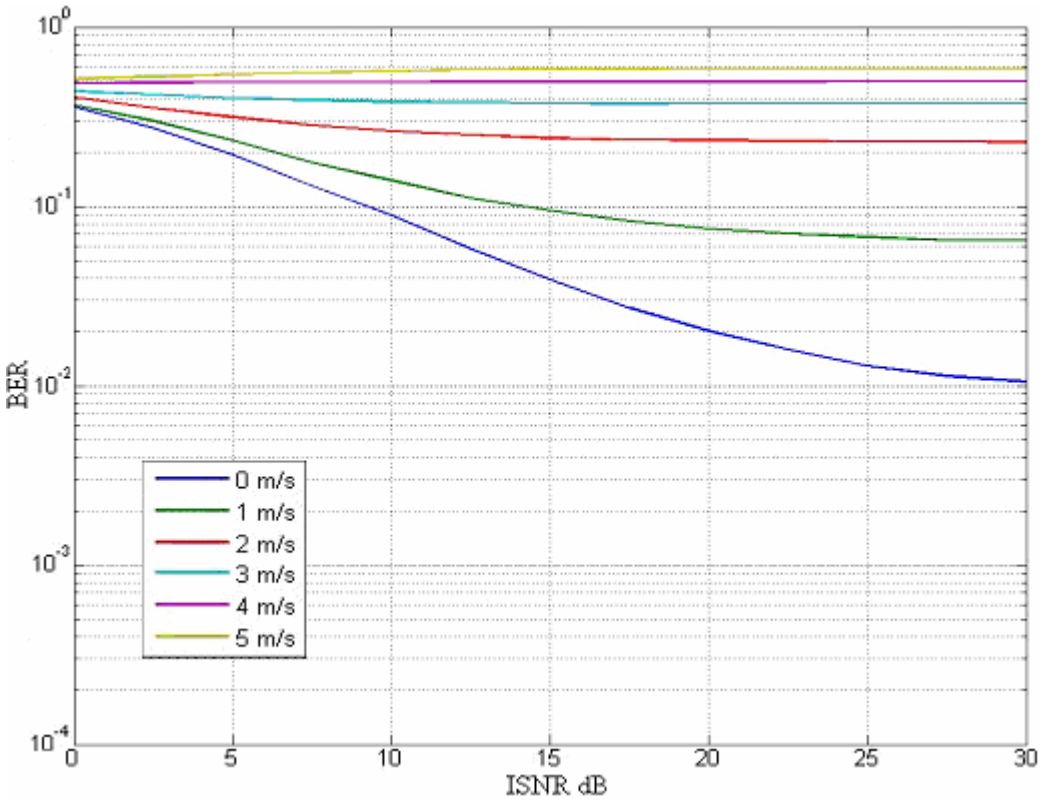

Figure 3.8: BER under varying ISNR and selected velocities at f_s=640 kHz for Test 3.1

Table 3.6[*]: Estimated Doppler shift $\hat{\Delta}_1$ from LFM signals at f_s=1.28MHz for Test 3.1

Velocity m/s	Doppler shift Δ	Estimated Doppler shift $\hat{\Delta}_1$ at different ISNR (dB)						
		0	5	10	15	20	25	30
-5.0	$-3.33*10^{-3}$	$-2.70*10^{-3}$	$-3.06*10^{-3}$	$-3.23*10^{-3}$	$-3.24*10^{-3}$	$-3.24*10^{-3}$	$-3.24*10^{-3}$	$-3.24*10^{-3}$
-4.0	$-2.67*10^{-3}$	$-2.07*10^{-3}$	$-2.46*10^{-3}$	$-2.59*10^{-3}$	$-2.60*10^{-3}$	$-2.60*10^{-3}$	$-2.60*10^{-3}$	$-2.60*10^{-3}$
-3.0	$-2.00*10^{-3}$	$-1.61*10^{-3}$	$-1.70*10^{-3}$	$-1.80*10^{-3}$	$-1.82*10^{-3}$	$-1.82*10^{-3}$	$-1.82*10^{-3}$	$-1.82*10^{-3}$
-2.0	$-1.33*10^{-3}$	$-1.08*10^{-3}$	$-1.12*10^{-3}$	$-1.17*10^{-3}$	$-1.17*10^{-3}$	$-1.17*10^{-3}$	$-1.17*10^{-3}$	$-1.17*10^{-3}$
-1.0	$-6.67*10^{-4}$	$-5.76*10^{-4}$	$-4.84*10^{-4}$	$-5.16*10^{-4}$	$-5.19*10^{-4}$	$-5.20*10^{-4}$	$-5.20*10^{-4}$	$-5.20*10^{-4}$
0	0	$-1.91*10^{-4}$	$3.53*10^{-5}$	$5.48*10^{-6}$	$7.81*10^{-7}$	0	0	0
1.0	$6.67*10^{-4}$	$3.64*10^{-4}$	$7.99*10^{-4}$	$7.86*10^{-4}$	$7.82*10^{-4}$	$7.82*10^{-4}$	$7.82*10^{-4}$	$7.82*10^{-4}$
2.0	$1.33*10^{-3}$	$9.12*10^{-4}$	$1.36*10^{-3}$	$1.45*10^{-3}$	$1.44*10^{-3}$	$1.43*10^{-3}$	$1.43*10^{-3}$	$1.43*10^{-3}$
3.0	$2.00*10^{-3}$	$1.47*10^{-3}$	$2.02*10^{-3}$	$2.10*10^{-3}$	$2.09*10^{-3}$	$2.09*10^{-3}$	$2.09*10^{-3}$	$2.09*10^{-3}$
4.0	$2.67*10^{-3}$	$2.08*10^{-3}$	$2.78*10^{-3}$	$2.87*10^{-3}$	$2.87*10^{-3}$	$2.87*10^{-3}$	$2.87*10^{-3}$	$2.87*10^{-3}$
5.0	$3.33*10^{-3}$	$2.57*10^{-3}$	$3.43*10^{-3}$	$3.53*10^{-3}$	$3.53*10^{-3}$	$3.53*10^{-3}$	$3.53*10^{-3}$	$3.53*10^{-3}$

[*] Values in red represent estimates that are less accurate than those obtained at f_s = 640 kHz.

Table 3.7[*]: MSE ε from overall Doppler acquisition at f_s=1.28MHz for Test 3.1.

Velocity m/s	Doppler MSE $\varepsilon = \left(\Delta - \hat{\Delta}_1 - \hat{\Delta}_2\right)^2$ at different ISNR (dB)						
	0	5	10	15	20	25	30
-5.0	$4.94*10^{-7}$	$1.32*10^{-7}$	$4.20*10^{-8}$	$3.80*10^{-8}$	$3.84*10^{-8}$	$3.80*10^{-8}$	$3.80*10^{-8}$
-4.0	$5.48*10^{-7}$	$8.47*10^{-8}$	$2.46*10^{-8}$	$2.28*10^{-8}$	$2.28*10^{-8}$	$2.28*10^{-8}$	$2.28*10^{-8}$
-3.0	$2.79*10^{-7}$	$6.00*10^{-8}$	$1.66*10^{-8}$	$1.21*10^{-8}$	$1.21*10^{-8}$	$1.21*10^{-8}$	$1.21*10^{-8}$
-2.0	$1.19*10^{-8}$	$1.19*10^{-8}$	$4.87*10^{-9}$	$5.18*10^{-9}$	$5.17*10^{-9}$	$5.16*10^{-9}$	$5.17*10^{-9}$
-1.0	$1.46*10^{-8}$	$2.18*10^{-9}$	$1.40*10^{-9}$	$1.22*10^{-9}$	$1.19*10^{-9}$	$1.19*10^{-9}$	$1.20*10^{-9}$
0	$3.84*10^{-8}$	$1.02*10^{-9}$	$3.81*10^{-13}$	$7.24*10^{-12}$	$6.71*10^{-12}$	$5.95*10^{-12}$	$6.00*10^{-12}$
1.0	$7.08*10^{-8}$	$5.36*10^{-15}$	$1.35*10^{-9}$	$1.60*10^{-9}$	$1.60*10^{-9}$	$1.60*10^{-9}$	$1.61*10^{-9}$
2.0	$1.47*10^{-7}$	$1.51*10^{-8}$	$4.28*10^{-9}$	$6.16*10^{-9}$	$6.15*10^{-9}$	$6.16*10^{-9}$	$6.15*10^{-9}$
3.0	$6.94*10^{-7}$	$4.45*10^{-8}$	$1.42*10^{-8}$	$1.37*10^{-8}$	$1.42*10^{-8}$	$1.42*10^{-8}$	$1.42*10^{-8}$
4.0	$9.41*10^{-7}$	$6.60*10^{-8}$	$2.72*10^{-8}$	$2.59*10^{-8}$	$2.62*10^{-8}$	$2.59*10^{-8}$	$2.62*10^{-8}$
5.0	$1.17*10^{-6}$	$9.12*10^{-8}$	$4.41*10^{-8}$	$4.37*10^{-8}$	$4.37*10^{-8}$	$4.37*10^{-8}$	$4.37*10^{-8}$

Table 3.6 and Table 3.7 show $\hat{\Delta}_1$ and ε, respectively, at f_s = 1.28 MHz. The MSE ε once again reaches a threshold from an ISNR of 10 dB onwards. The improvement in accuracy of $\hat{\Delta}_1$ is marginal as the sampling rate increases.

3.5.3 Simulation Test 3.2

Having seen from the previous test the influence of Doppler spread upon the BER performance, we now seek to compensate for it via linear interpolation of the received signal. Doppler acquisition is carried out using the LFM signal followed by compensation with linear interpolation which corrects for the Doppler spreading effect. Compensation of the Doppler shift is subsequently performed using the OFDM cyclic prefix method.

[*] Values in red represent higher residual errors obtained due to $\hat{\Delta}_2 : \left(\Delta - \hat{\Delta}_1\right)^2 < \left(\Delta - \hat{\Delta}_1 - \hat{\Delta}_2\right)^2$.

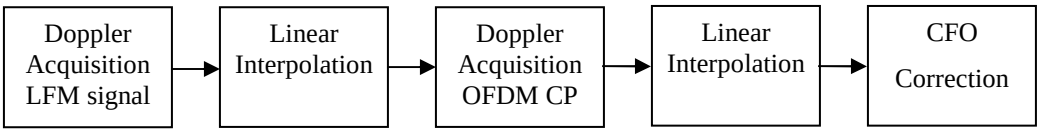

Figure 3.9: Schematic of both Doppler compensation methods applied in Test 3.2

The previous simulations show that sampling frequency inadvertently affects the accuracy of Doppler acquisition from the LFM signals. Thus we perform the simulation starting with a sampling frequency f_s = 640 kHz. Table 3.8 shows the accuracy of Doppler acquisition from the LFM signal only, which once again reaches a threshold at 10 dB due to limitations in the timing resolution. Table 3.9 shows the MSE after Doppler estimation using the OFDM cyclic prefix. The figures in red represent MSEs that exceed those in Table 3.8. Not only are the MSEs smaller than the previous test, the estimates $\widehat{\Delta}_2$ were also more precise as seen in Figure 3.10.

Table 3.8: Doppler MSE ε from $\widehat{\Delta}_1$ at f_s=640 kHz for Test 3.2.

Velocity m/s	Doppler MSE $\varepsilon = \left(\Delta - \widehat{\Delta}_1\right)^2$ at different ISNR (dB)						
	0	5	10	15	20	25	30
-5.0	$3.06*10^{-7}$	$1.16*10^{-7}$	$5.11*10^{-8}$	$4.84*10^{-8}$	$4.84*10^{-8}$	$4.84*10^{-8}$	$4.84*10^{-8}$
-4.0	$5.46*10^{-7}$	$1.62*10^{-7}$	$1.18*10^{-7}$	$1.09*10^{-7}$	$1.09*10^{-7}$	$1.09*10^{-7}$	$1.09*10^{-7}$
-3.0	$3.84*10^{-7}$	$6.50*10^{-8}$	$3.53*10^{-8}$	$3.28*10^{-8}$	$3.28*10^{-8}$	$3.28*10^{-8}$	$3.28*10^{-8}$
-2.0	$5.16*10^{-7}$	$1.57*10^{-7}$	$9.00*10^{-8}$	$8.58*10^{-8}$	$8.58*10^{-8}$	$8.58*10^{-8}$	$8.58*10^{-8}$
-1.0	$2.91*10^{-7}$	$6.60*10^{-8}$	$2.31*10^{-8}$	$2.13*10^{-8}$	$2.13*10^{-8}$	$2.13*10^{-8}$	$2.13*10^{-8}$
0	$1.72*10^{-8}$	$4.93*10^{-10}$	0	0	0	0	0
1.0	$2.58*10^{-9}$	$9.80*10^{-8}$	$1.41*10^{-7}$	$1.41*10^{-7}$	$1.41*10^{-7}$	$1.41*10^{-7}$	$1.41*10^{-7}$
2.0	$3.08*10^{-9}$	$2.59*10^{-8}$	$5.06*10^{-8}$	$5.34*10^{-8}$	$5.34*10^{-8}$	$5.34*10^{-8}$	$5.34*10^{-8}$
3.0	$3.17*10^{-9}$	$8.53*10^{-8}$	$1.21*10^{-7}$	$1.21*10^{-7}$	$1.21*10^{-7}$	$1.21*10^{-7}$	$1.21*10^{-7}$
4.0	$5.79*10^{-9}$	$2.28*10^{-8}$	$4.20*10^{-8}$	$4.20*10^{-8}$	$4.20*10^{-8}$	$4.20*10^{-8}$	$4.20*10^{-8}$
5.0	$2.50*10^{-7}$	$2.31*10^{-8}$	$6.76*10^{-10}$	$8.94*10^{-10}$	$1.91*10^{-9}$	$1.86*10^{-9}$	$1.88*10^{-9}$

Table 3.9: Doppler MSE ε from $\hat{\Delta}_1 + \hat{\Delta}_2$ at f_s=640 kHz for Test 3.2.

Velocity m/s	Doppler MSE $\varepsilon = \left(\Delta - \hat{\Delta}_1 - \hat{\Delta}_2\right)^2$ at different ISNR (dB)						
	0	5	10	15	20	25	30
-5.0	$9.67*10^{-8}$	$1.54*10^{-8}$	$5.67*10^{-11}$	$8.41*10^{-13}$	$1.56*10^{-12}$	$1.90*10^{-12}$	$1.72*10^{-12}$
-4.0	$1.41*10^{-7}$	$5.52*10^{-9}$	$2.16*10^{-10}$	$5.29*10^{-12}$	$6.45*10^{-12}$	$6.00*10^{-12}$	$5.48*10^{-12}$
-3.0	$1.67*10^{-7}$	$4.48*10^{-9}$	$3.53*10^{-11}$	$6.02*10^{-13}$	$2.36*10^{-13}$	$1.11*10^{-13}$	$3.03*10^{-14}$
-2.0	$1.60*10^{-7}$	$1.00*10^{-8}$	$5.94*10^{-11}$	$6.50*10^{-12}$	$2.99*10^{-12}$	$4.58*10^{-12}$	$3.80*10^{-12}$
-1.0	$1.38*10^{-7}$	$1.00*10^{-8}$	$2.95*10^{-11}$	$4.93*10^{-14}$	$1.08*10^{-15}$	$4.75*10^{-16}$	$3.06*10^{-14}$
0	$1.39*10^{-8}$	$6.05*10^{-10}$	$5.58*10^{-13}$	$2.50*10^{-12}$	$1.93*10^{-12}$	$3.10*10^{-12}$	$2.72*10^{-12}$
1.0	$8.53*10^{-8}$	$3.01*10^{-9}$	$1.65*10^{-11}$	$1.41*10^{-11}$	$1.19*10^{-11}$	$1.06*10^{-11}$	$1.10*10^{-11}$
2.0	$6.81*10^{-8}$	$3.91*10^{-9}$	$2.44*10^{-11}$	$1.80*10^{-12}$	$1.28*10^{-12}$	$2.31*10^{-12}$	$1.82*10^{-12}$
3.0	$6.92*10^{-8}$	$2.39*10^{-9}$	$3.76*10^{-12}$	$7.73*10^{-12}$	$9.61*10^{-12}$	$1.14*10^{-11}$	$1.08*10^{-11}$
4.0	$7.24*10^{-8}$	$2.81*10^{-9}$	$5.76*10^{-12}$	$4.84*10^{-12}$	$1.74*10^{-12}$	$2.25*10^{-12}$	$2.89*10^{-12}$
5.0	$3.66*10^{-7}$	$5.81*10^{-8}$	$1.62*10^{-9}$	$1.12*10^{-9}$	$3.69*10^{-10}$	$3.92*10^{-10}$	$3.80*10^{-10}$

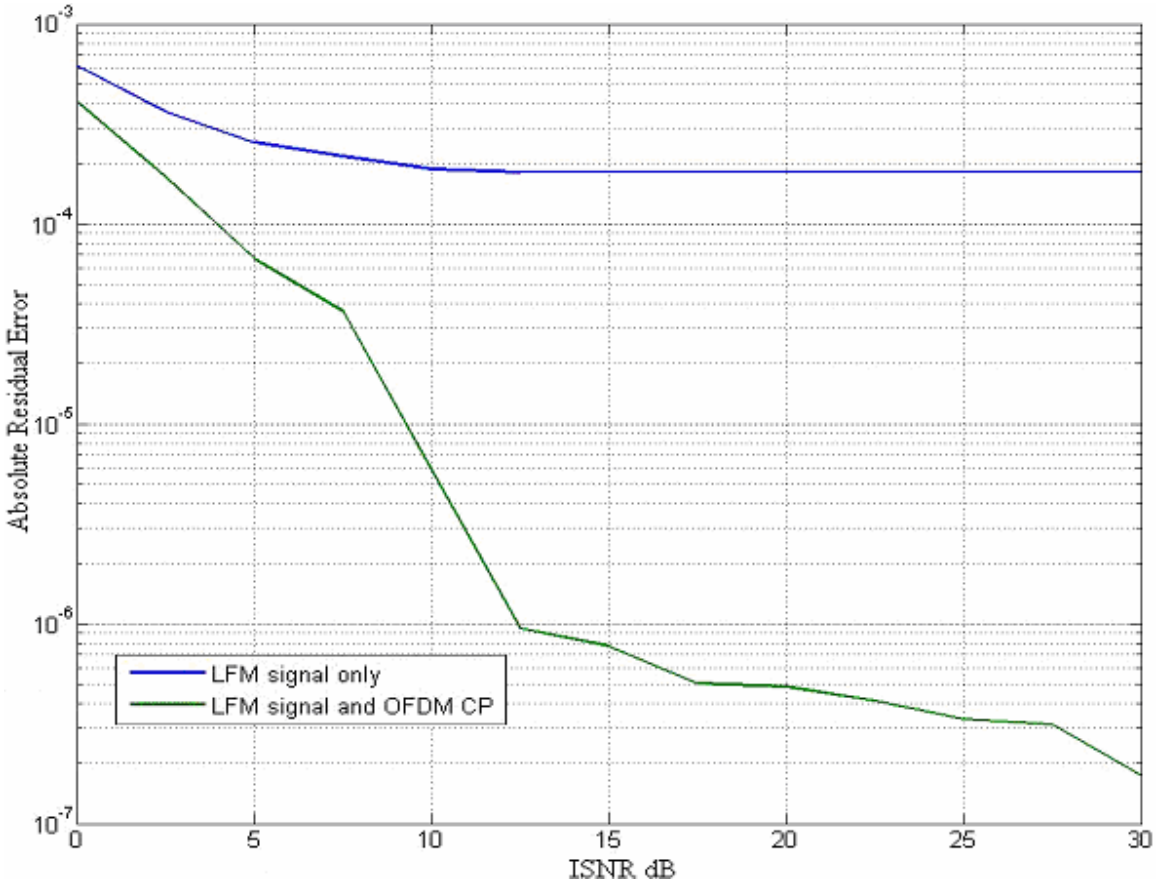

Figure 3.10: Doppler RMS error $\sqrt{\varepsilon}$ in varying ISNR at -3m/s and f_s=640kHz for Test 3.2

Figure 3.11 shows the BER across different ISNR and velocities with interpolation applied using the estimate $\widehat{\Delta}_1$ and CFO compensation applied using the estimate $\widehat{\Delta}_2$. From the similar BER performance for different velocities, it is evident that interpolation is able to compensate for the mobility-induced expansion and contraction of the received signal in the time domain.

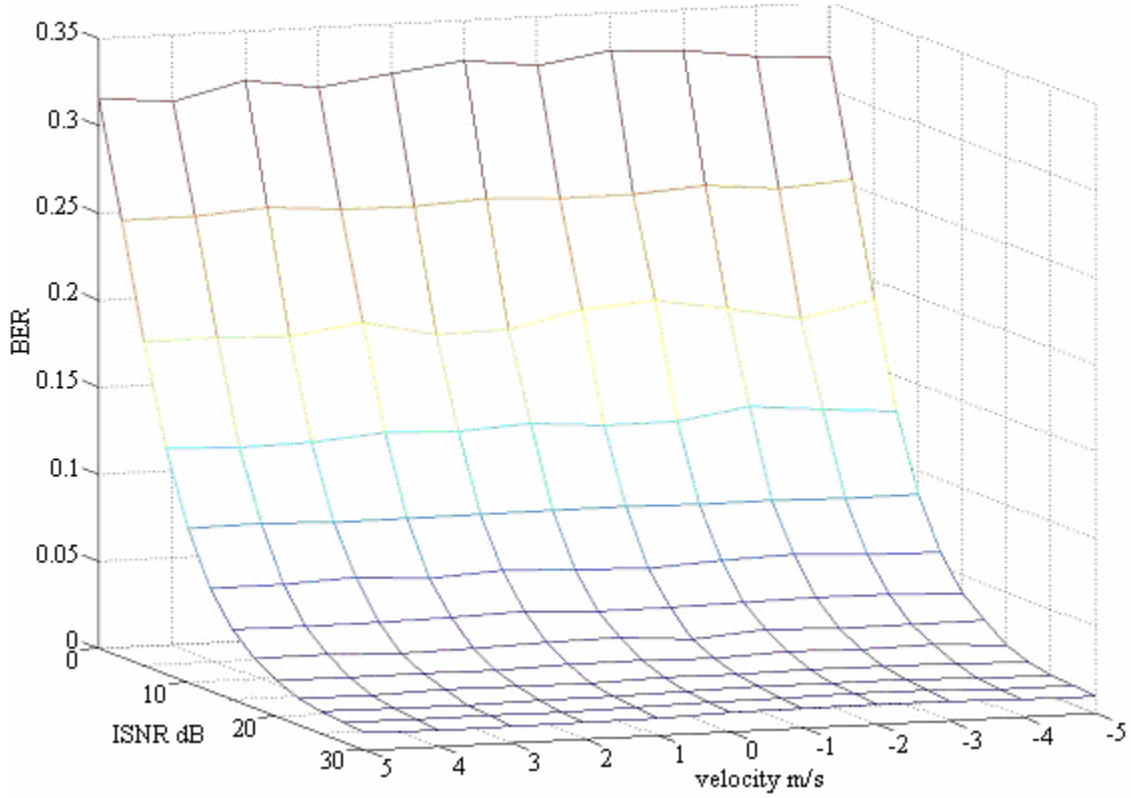

Figure 3.11: BER under varying ISNR and velocity at f_s=640 kHz for Test 3.2

Figure 3.12 shows a detailed comparison in BER at selected velocities. The similarity in performance indicates the ability of interpolation to eradicate Doppler spread due to mobility. Further testing at f_s = 1.28 MHz and 2.56 MHz yielded similar performances in BER, hence proving that the time resolution at f_s = 640 kHz is sufficient for the initial Doppler compensation using LFM signals.

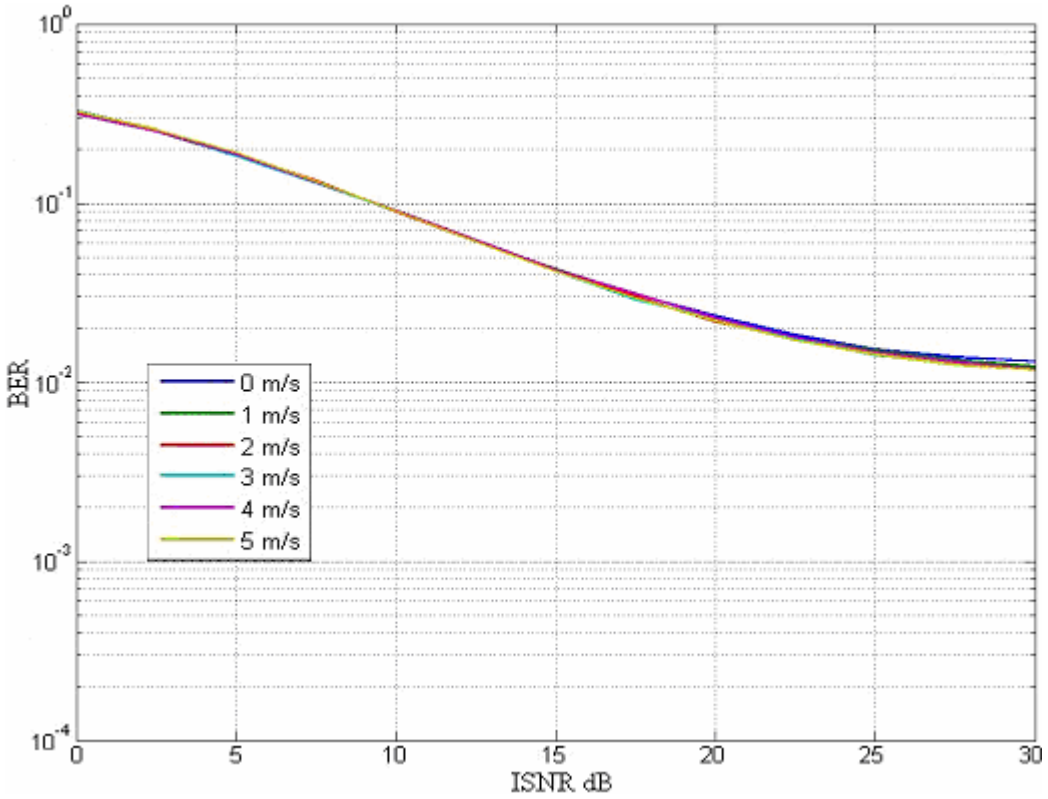

Figure 3.12: BER under varying ISNR and selected velocities at f_s=640 kHz for Test 3.2

3.5.4 Simulation Test 3.3

Having seen the performance of Doppler compensation using a combination of LFM signal and OFDM cyclic prefix correlation, we now study the performance of the iterative interpolation approach [15].

The iterative interpolation algorithm seen in the previous section of this chapter is applied only to the first OFDM symbol as we have assumed perfect synchronization without knowledge of the exact start timing of the remaining symbols due to time dilation or compression of the signal frame. The velocity is assumed to be constant for the period of the signal frame, hence the estimated timing mismatch of $\hat{\Delta}$ is valid for the entirety of the signal frame. As the phase offset ϕ_{peak} cannot be zero in the presence of noise and ISI due to multi-path arrivals, a threshold of $5*10^{-4}$ is imposed on the absolute value of ϕ_{peak} to be considered as a good estimate. In addition, a limit of 5 iterations is imposed in order to prevent excessive computational complexity.

Table 3.10: Doppler MSE ε from $\hat{\Delta}$ at f_s = 160 kHz for Test 3.3.

Velocity m/s	Doppler shift Δ	Doppler MSE $\varepsilon = (\Delta - \hat{\Delta})^2$ at different ISNR (dB)						
		0	5	10	15	20	25	30
-5.0	$-3.33*10^{-3}$	$2.79*10^{-8}$	$3.06*10^{-9}$	$1.30*10^{-10}$	$3.87*10^{-11}$	$2.69*10^{-11}$	$2.97*10^{-13}$	$3.40*10^{-13}$
-4.0	$-2.67*10^{-3}$	$1.61*10^{-7}$	$3.17*10^{-8}$	$8.65*10^{-9}$	$3.66*10^{-9}$	$3.04*10^{-9}$	$3.00*10^{-9}$	$1.41*10^{-9}$
-3.0	$-2.00*10^{-3}$	$7.45*10^{-6}$	$8.88*10^{-6}$	$9.61*10^{-6}$	$9.67*10^{-6}$	$1.00*10^{-5}$	$1.01*10^{-5}$	$1.01*10^{-5}$
-2.0	$-1.33*10^{-3}$	$1.59*10^{-8}$	$8.95*10^{-9}$	$1.60*10^{-9}$	$5.95*10^{-10}$	$1.64*10^{-10}$	$3.50*10^{-10}$	$1.64*10^{-10}$
-1.0	$-6.67*10^{-4}$	$2.69*10^{-9}$	$2.89*10^{-10}$	$1.25*10^{-10}$	$9.12*10^{-11}$	$2.55*10^{-11}$	$1.56*10^{-11}$	$8.07*10^{-12}$
0	0	$1.04*10^{-8}$	$1.08*10^{-10}$	$8.93*10^{-11}$	$3.56*10^{-11}$	$7.97*10^{-11}$	$2.34*10^{-11}$	$4.57*10^{-11}$
1.0	$6.67*10^{-4}$	$1.17*10^{-10}$	$5.81*10^{-9}$	$6.76*10^{-10}$	$1.00*10^{-9}$	$9.92*10^{-10}$	$9.73*10^{-10}$	$6.60*10^{-10}$
2.0	$1.33*10^{-3}$	$8.54*10^{-9}$	$1.21*10^{-9}$	$3.76*10^{-10}$	$3.76*10^{-10}$	$3.84*10^{-10}$	$3.88*10^{-10}$	$3.88*10^{-10}$
3.0	$2.00*10^{-3}$	$7.02*10^{-6}$	$9.06*10^{-6}$	$9.67*10^{-6}$	$9.92*10^{-6}$	$9.92*10^{-6}$	$9.99*10^{-6}$	$9.99*10^{-6}$
4.0	$2.67*10^{-3}$	$1.55*10^{-7}$	$2.82*10^{-8}$	$1.30*10^{-8}$	$1.39*10^{-8}$	$1.30*10^{-8}$	$7.97*10^{-9}$	$8.89*10^{-9}$
5.0	$3.33*10^{-3}$	$6.81*10^{-8}$	$1.66*10^{-9}$	$6.15*10^{-10}$	$1.51*10^{-9}$	$3.69*10^{-10}$	$1.82*10^{-10}$	$7.53*10^{-11}$

Table 3.11: Average number of iterations at f_s=160 kHz for Test 3.3.

Velocity m/s	Average number of iterations at different ISNR (dB)						
	0	5	10	15	20	25	30
-5.0	3.16	2.89	2.77	2.69	2.69	2.71	2.69
-4.0	3.24	3.02	2.87	2.66	2.66	2.64	2.63
-3.0	4.86	4.94	4.96	4.97	4.97	4.97	4.97
-2.0	3.38	3.12	2.86	2.82	2.76	2.76	2.77
-1.0	3.36	3.02	2.90	2.79	2.73	2.74	2.73
0	2.76	2.23	2.11	1.97	1.89	1.88	1.89
1.0	3.39	3.06	2.85	2.75	2.70	2.69	2.69
2.0	3.34	2.95	2.85	2.71	2.66	2.67	2.66
3.0	4.91	4.95	4.98	4.98	4.98	4.99	4.99
4.0	3.26	2.91	2.77	2.67	2.65	2.65	2.63
5.0	3.10	2.84	2.68	2.67	2.61	2.62	2.60

Table 3.10 shows the average residual error ε at the end of the iterations conducted at a sampling rate of f_s = 640 kHz. At velocities of -3.0 m/s and 3.0 m/s, these errors were observed to be of the same order as the Doppler shift Δ. Further inspection of Table 3.11 shows that the average number of iterations required were very close to the limit of 5 at these velocities. This implies that the algorithm could not satisfy the stopping criteria before reaching the iteration limit imposed.

As a result, the BER at these velocities seen in Figure 3.13 and Figure 3.14 are extremely poor. The BER for the remaining velocities shown are slightly poorer than that obtained in Test 3.2. This is most likely due to the fact that the Doppler estimates obtained in the previous test were generally more accurate than the estimates obtained here. Lowering the threshold level would lead to an improvement in precision of $\hat{\Delta}$ from the iterative interpolation algorithm at the price of an increment in iterations.

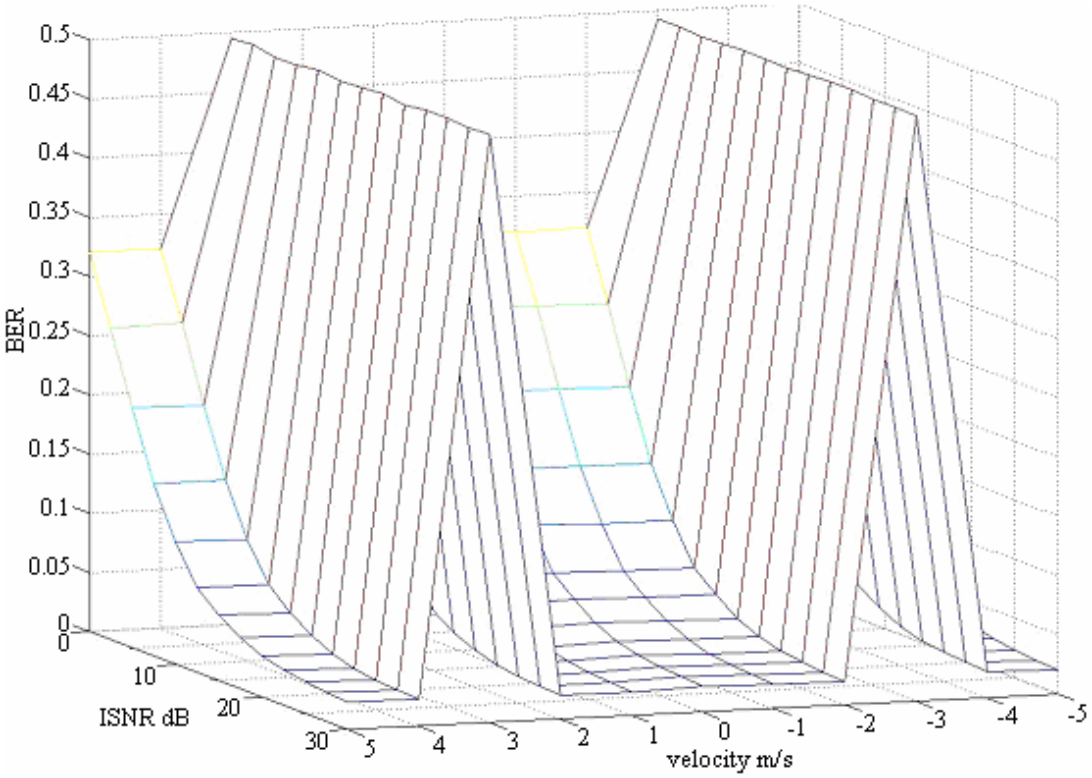

Figure 3.13: BER under varying ISNR and velocity at f_s=160 kHz for Test 3.3

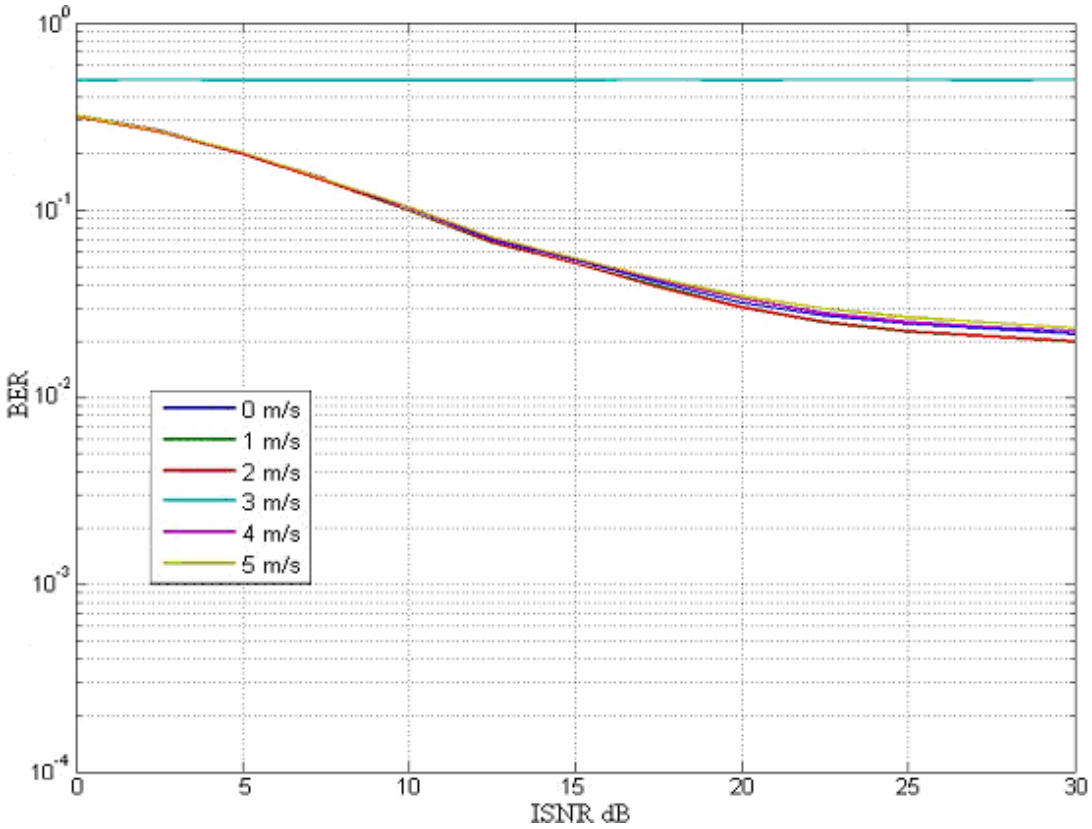

Figure 3.14: BER under varying ISNR and selected velocities at f_s=160 kHz for Test 3.3

Table 3.12: Doppler MSE ε from $\hat{\Delta}$ at f_s = 640 kHz for Test 3.3.

Velocity m/s	Doppler shift Δ	Doppler MSE $\varepsilon = (\Delta - \hat{\Delta})^2$ at different ISNR (dB)						
		0	5	10	15	20	25	30
-5.0	$-3.33*10^{-3}$	$2.86*10^{-8}$	$8.12*10^{-9}$	$8.76*10^{-10}$	$8.76*10^{-11}$	$5.61*10^{-11}$	$5.37*10^{-11}$	$5.42*10^{-11}$
-4.0	$-2.67*10^{-3}$	$1.76*10^{-7}$	$4.71*10^{-8}$	$8.28*10^{-9}$	$9.33*10^{-9}$	$2.39*10^{-9}$	$2.39*10^{-9}$	$2.38*10^{-9}$
-3.0	$-2.00*10^{-3}$	$8.07*10^{-6}$	$8.76*10^{-6}$	$9.80*10^{-6}$	$1.03*10^{-5}$	$1.04*10^{-5}$	$1.03*10^{-5}$	$1.04*10^{-5}$
-2.0	$-1.33*10^{-3}$	$2.19*10^{-8}$	$7.84*10^{-10}$	$8.23*10^{-11}$	$2.03*10^{-11}$	$3.39*10^{-12}$	$2.16*10^{-12}$	$2.82*10^{-12}$
-1.0	$-6.67*10^{-4}$	$1.17*10^{-10}$	$1.23*10^{-12}$	$6.86*10^{-10}$	$1.82*10^{-10}$	$1.85*10^{-10}$	$6.29*10^{-11}$	$6.02*10^{-11}$
0	0	$3.65*10^{-10}$	$3.08*10^{-9}$	$3.57*10^{-10}$	$8.19*10^{-11}$	$5.49*10^{-11}$	$6.19*10^{-11}$	$5.78*10^{-11}$
1.0	$6.67*10^{-4}$	$3.39*10^{-10}$	$1.33*10^{-9}$	$4.58*10^{-10}$	$5.17*10^{-11}$	$6.13*10^{-11}$	$4.62*10^{-12}$	$1.24*10^{-11}$
2.0	$1.33*10^{-3}$	$2.46*10^{-8}$	$3.28*10^{-9}$	$2.07*10^{-10}$	$1.60*10^{-11}$	$3.57*10^{-12}$	$1.88*10^{-11}$	$3.03*10^{-12}$
3.0	$2.00*10^{-3}$	$7.84*10^{-6}$	$9.49*10^{-6}$	$1.00*10^{-5}$	$1.01*10^{-5}$	$1.03*10^{-5}$	$1.04*10^{-5}$	$1.04*10^{-5}$
4.0	$2.67*10^{-3}$	$2.03*10^{-7}$	$8.70*10^{-8}$	$3.06*10^{-8}$	$8.63*10^{-9}$	$8.57*10^{-9}$	$7.67*10^{-9}$	$6.76*10^{-9}$
5.0	$3.33*10^{-3}$	$3.20*10^{-8}$	$3.50*10^{-9}$	$2.62*10^{-10}$	$2.40*10^{-10}$	$1.76*10^{-11}$	$1.17*10^{-11}$	$9.42*10^{-12}$

Table 3.13: Average number of iterations at f_s = 640 kHz for Test 3.3.

Velocity	Average number of iterations at different ISNR (dB)						
m/s	0	5	10	15	20	25	30
-5.0	3.66	3.18	2.98	2.96	2.79	2.77	2.77
-4.0	3.65	3.38	2.95	2.76	2.64	2.64	2.64
-3.0	4.95	4.98	5.00	4.99	4.99	5.00	5.00
-2.0	4.36	4.25	4.10	4.09	4.05	4.04	4.01
-1.0	4.42	4.36	4.23	4.16	4.10	4.11	4.11
0	3.59	3.08	2.84	2.54	2.45	2.42	2.46
1.0	4.45	4.33	4.08	4.02	3.98	3.95	3.99
2.0	4.42	4.30	4.16	4.02	3.95	3.95	3.92
3.0	4.95	4.99	4.98	5.00	4.99	4.99	5.00
4.0	3.62	3.17	3.02	2.84	2.80	2.71	2.71
5.0	3.55	3.21	2.96	2.81	2.72	2.77	2.70

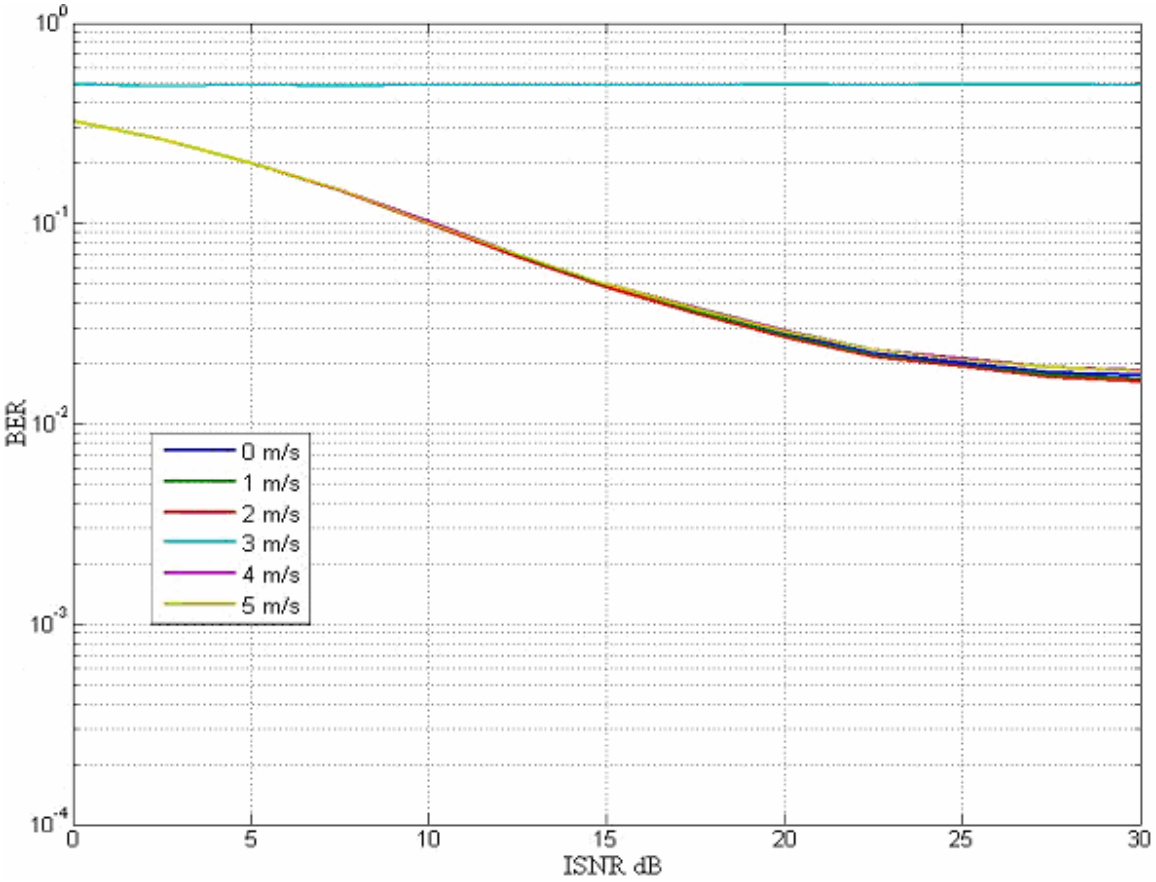

Figure 3.15: BER under varying ISNR and selected velocities at f_s=640 kHz for Test 3.3

Table 3.12 and Table 3.13 show that an increment in sampling rate did not improve the accuracy of Doppler estimation at -3.0 and 3.0 m/s, but resulted instead in higher number of iterations before meeting the stopping criteria. Figure 3.15 shows a similar BER performance when the sampling rate is 640 kHz. Further tests at higher sampling yielded the same trend: an increasing number of iterations required with similar performance in Doppler estimation and BER performance.

3.5.5 Simulation Test 3.4

Previous simulations have shown that while interpolation is able to correct for mobility induced Doppler spreading of the signal, BER however tends to decrease at a

slower rate at higher ISNR. This is most likely due to the sensitivity of OFDM to offsets in carrier frequency. Although the residual Doppler errors seen previously in Test 3.2 and Test 3.3 were low, they were based upon the average of $\hat{\Delta}_2$ obtained from individual OFDM cyclic prefixes. Hence, some of the individual estimates would be more imprecise than others, resulting in higher BER for the specific OFDM symbol. If we assume that time dilation / constriction is constant over the length of the signal frame, then CFO compensation by frame using Eq. (3.20) developed previously would be feasible.

The simulation conducted here is similar to Test 3.1, except that $\hat{\Delta}_2$ is obtained via Eq. (3.20) and only CFO compensation is applied thereafter. Table 3.14 shows the residual Doppler error obtained at various velocities and ISNR. Compared to Test 3.2, the MSEs are generally lower using this method, with RMS error order of 10^{-7} achievable from 15 dB onwards.

Table 3.14: Doppler MSE ε from $\hat{\Delta}_1 + \hat{\Delta}_2$ at f_s = 640 kHz for Test 3.4.

Velocity	Doppler	Doppler MSE $\varepsilon = \left(\Delta - \hat{\Delta}_1 - \hat{\Delta}_2\right)^2$ at different ISNR (dB)						
m/s	shift Δ	0	5	10	15	20	25	30
-5.0	$-3.33*10^{-3}$	$6.35*10^{-8}$	$1.95*10^{-9}$	$5.46*10^{-11}$	$2.50*10^{-13}$	$1.52*10^{-13}$	$1.12*10^{-13}$	$9.24*10^{-14}$
-4.0	$-2.67*10^{-3}$	$3.46*10^{-8}$	$3.12*10^{-9}$	$2.07*10^{-10}$	$4.37*10^{-14}$	$1.90*10^{-14}$	$6.15*10^{-14}$	$7.29*10^{-14}$
-3.0	$-2.00*10^{-3}$	$2.16*10^{-8}$	$7.08*10^{-10}$	$3.42*10^{-11}$	$1.14*10^{-13}$	$1.14*10^{-13}$	$1.11*10^{-13}$	$1.10*10^{-13}$
-2.0	$-1.33*10^{-3}$	$1.10*10^{-8}$	$6.45*10^{-10}$	$4.75*10^{-12}$	$1.02*10^{-14}$	$4.04*10^{-14}$	$6.10*10^{-14}$	$7.24*10^{-14}$
-1.0	$-6.67*10^{-4}$	$1.66*10^{-9}$	$9.72*10^{-11}$	$3.35*10^{-11}$	$1.18*10^{-13}$	$1.13*10^{-13}$	$1.10*10^{-13}$	$1.10*10^{-13}$
0	0	$6.76*10^{-10}$	$3.32*10^{-11}$	$4.04*10^{-12}$	$1.74*10^{-14}$	$5.02*10^{-14}$	$7.62*10^{-14}$	$9.36*10^{-14}$
1.0	$6.67*10^{-4}$	$2.76*10^{-9}$	$2.44*10^{-11}$	$7.45*10^{-12}$	$2.98*10^{-13}$	$2.20*10^{-13}$	$1.78*10^{-13}$	$1.55*10^{-13}$
2.0	$1.33*10^{-3}$	$1.72*10^{-8}$	$1.27*10^{-9}$	$2.27*10^{-11}$	$2.21*10^{-13}$	$1.74*10^{-13}$	$1.60*10^{-13}$	$1.56*10^{-13}$
3.0	$2.00*10^{-3}$	$2.99*10^{-8}$	$1.62*10^{-9}$	$7.73*10^{-11}$	$2.53*10^{-13}$	$2.02*10^{-13}$	$1.78*10^{-13}$	$1.66*10^{-13}$
4.0	$2.67*10^{-3}$	$2.04*10^{-8}$	$8.47*10^{-10}$	$4.04*10^{-11}$	$1.47*10^{-13}$	$1.41*10^{-13}$	$1.28*10^{-13}$	$1.06*10^{-13}$
5.0	$3.33*10^{-3}$	$6.66*10^{-8}$	$2.08*10^{-9}$	$3.92*10^{-14}$	$8.64*10^{-14}$	$1.11*10^{-13}$	$1.27*10^{-13}$	$1.36*10^{-13}$

Figure 3.16 shows BER in the order of 10^{-3} attained for ISNR above 25 dB, surpassing the results obtained previously whereby BER in the order of 10^{-2} were unachievable even at ISNR of 30 dB. Unlike the previous tests, the decrement in BER does not reach a threshold, demonstrating the sensitivity of OFDM to carrier frequency offsets.

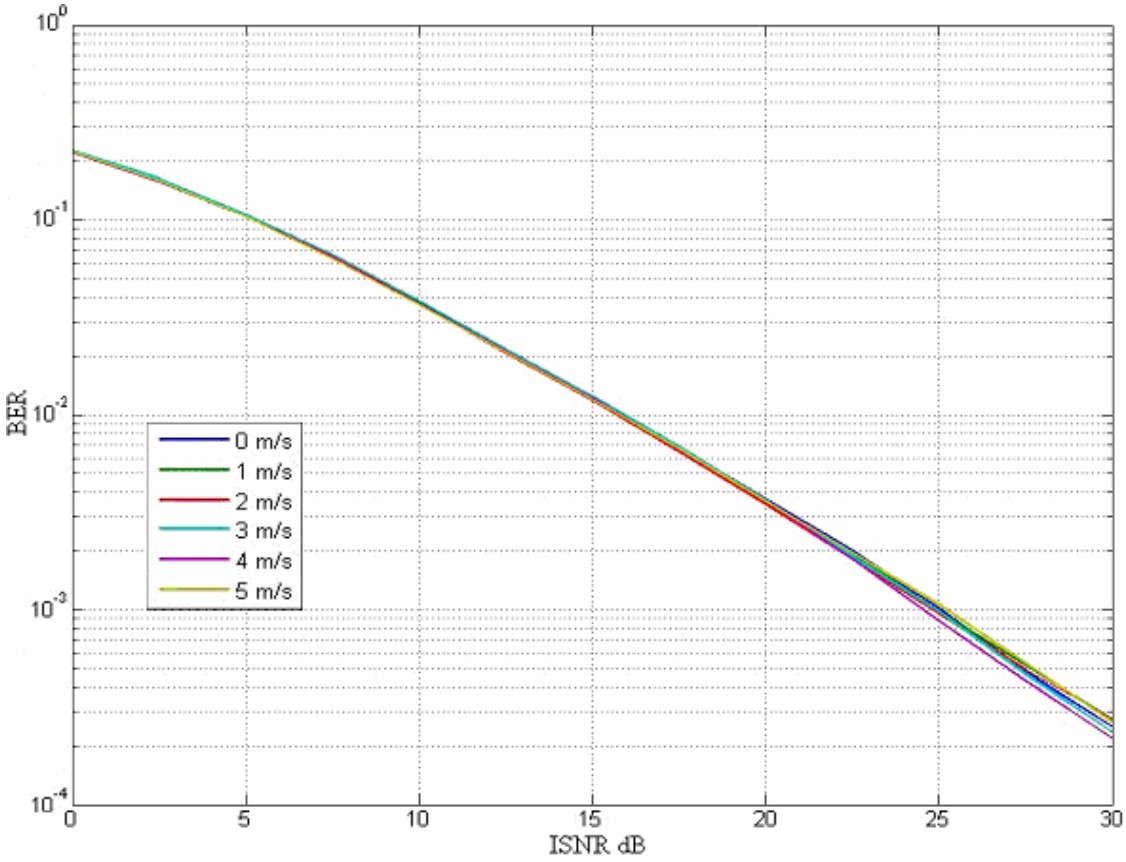

Figure 3.16: BER under varying ISNR and selected velocities at f_s=640 kHz for Test 3.4

3.6 Conclusion

In this chapter, we reviewed the mathematical model of mobility-induced Doppler spreading in wideband signals. Due to the fact that propagation speed of sound is at most 1000 times more than the expected speeds of mobile platforms in UWA channels, the Doppler timing scaling factor Δ becomes significant; hence the spread in the frequency spectrum of the signal becomes more accentuated.

The OFDM signal modulation scheme is presented in this chapter and shows how the usage of a cyclic prefix is able to combat ISI in a multi-path channel. Also, the data symbols under QPSK and DPSK modulation is expounded upon to complete the overall model of the communications framework.

Due to time dilation / compression, it is shown that CFO compensation using OFDM cyclic prefix correlation [44] is not sufficient due to the loss of orthogonality between sub-carriers, resulting in further ICI. Linear interpolation is an attractive method to compensate for the time dilations and compressions of the signal due to the ease of implementation and comparatively low computational complexity involved. The ML estimator using null sub-carriers in [33] is avoided as the ambient noise in warm shallow UWA channels is impulsive and not Gaussian; also, the comparatively high computational complexity places this method at a disadvantage. Doppler acquisition is performed using 2 different methods: using LFM signals and using the OFDM cyclic prefix. The former incurs a penalty on bandwidth usage but has a wide ambiguity function that makes it more detectable in mobile conditions.

The tests show that neglecting Doppler spread in the signal results in performance degradation in terms of BER at augmenting speeds. To effectively apply Doppler acquisition using LFM signals, the sampling rate and transmission delay between signals must be high enough to provide the required timing resolution. Estimating Doppler using the OFDM cyclic prefix however requires a few iterations and may not work at certain velocities. Nevertheless, linear interpolation has proven to be capable of compensating Doppler spread. Finally, CFO compensation by frame can greatly enhance the BER performance should there be no acceleration during the period of the signal frame.

4. Signal Detection and Timing Synchronization

A question commonly asked in communications systems is how signal detection and synchronization should be performed given a particular channel model. In this case, the UWA model is fast time-varying, dispersive, and has impulsive ambient noise. ML based detection methods would be sub-optimum since they rely on the Gaussian noise model with finite variance. This chapter looks into developing a method of detection and synchronization based upon constraints imposed by this particular channel.

4.1 General Signal Detection

4.1.1 Windowed Cross Correlation Detector

In the previous chapter, we have defined the ambiguity function and have stated that LFM signals would yield a ridge along the correlation delay axis which, under practical velocities, can be considered to vary linearly with the Doppler scaling factor.

In general, when a received signal *r(t)* is cross correlated with the original signal *s(t)*, a measure of how insensitive the signal is to the Doppler lies in the ability to detect a distinct peak at various Doppler scaling factors. However, in impulsive ambient noise, the peak can arise not due to a fact of high correlation between the received signal and the transmitted signal, but also due to a sudden spike in amplitude that is falsely detected.

To address this problem, the cross correlation function is normalized within the window of measurement. Let *T* represent the window length in which the cross correlation is measured. The windowed cross correlation is very similar to the OFDM cyclic prefix correlation in Eq. (3.19):

$$c_{rs}(\tau) = \frac{\sum_{n=0}^{T-1} r^*(n+\tau)s(n)}{\sqrt{\sum_{n=0}^{T-1} r^*(n+\tau)r(n+\tau)}} \tag{4.1}$$

From Eq. (4.1), we see that the cross-correlation is normalized to the root of the energy of the received signal within the window. As signal detection is based upon the correlation about the start of the signal frame, this accentuates the detected peak since the energy of the incoming signal is usually much higher when there is a signal present under practical SNR ratios. Hence, when transiting from the time period where no signal is present to the moment where there is one, an implicit gain is applied to the cross correlation. However, it is to be noted that should the window period be too short such that the impulsive noise duration is significant, then false detection can still occur.

In order to mathematically define a distinct peak in cross-correlation without knowledge of the attenuation level upon the received signal, we analyze the cross-correlation once again in a window length. The choice of this length is important as it decides the accuracy and computational complexity of the estimation. A short window length may falsely represent a localized peak whereas a long window would require more processing time. In this thesis, a window length of $2T$ is chosen. The ratio between the square of the peak value of cross correlation and the variance of the cross-correlation within the window is used as the criteria of measurement:

$$\begin{aligned} \mathbf{C}(\tau) &= \left\lfloor c_{rs}(\tau) \quad \ldots \quad c_{rs}(\tau + 2T - 1) \right\rfloor \\ \eta &= \frac{\max\left(diag\left(\mathbf{C}^H(\tau)\right)\mathbf{C}(\tau)\right)}{\mathrm{var}\left(\mathbf{C}(\tau)\right)} \end{aligned} \tag{4.2}$$

4.1.2 Threshold Detection Parameter

From the previous chapter, we observe that two different signals are known at the receiver: the LFM signal and the OFDM pilot symbol(s). These two signals are used to find the threshold η empirically in the following test. The LFM signal used has duration of T = 4ms and a bandwidth of 20kHz centered about a carrier frequency of 50kHz. Likewise, an OFDM signal of N = 256 and N_p = 64 with the same bandwidth modulated at the same carrier frequency is used. However, only 4ms of the OFDM signal (equivalent to 80 baseband OFDM samples) is used for cross-correlation. The signal is subjected to various Doppler time-scaling factors and processed at different ranges using the warm shallow UWA channel model developed in [5]. In addition, a null period consisting of 4ms of ambient noise is introduced before the start of the received signals so that the correlation window comprises equally of cross correlation with ambient noise as well as the signal of interest. 10000 Monte Carlo trials are conducted to obtain the results.

4.1.3 Results

In the absence of Doppler time scaling upon the signal, a distinct peak should be observable under the assumption that the channel attributes a single path. Figure 4.1 illustrates an example of $|c_{rs}(\tau)|$ taken within the stipulated duration. A peak is seen along the time axis close to 0ms which demarks the start of the OFDM signal. In contrast to Figure 4.2, measured similarly at an ISNR of 10dB and velocity of -5m/s, the peak obtained from the cross correlation using LFM signals is very distinct, with two other peaks visible near 0.5ms and 3ms that denote the arrival of secondary and tertiary paths.

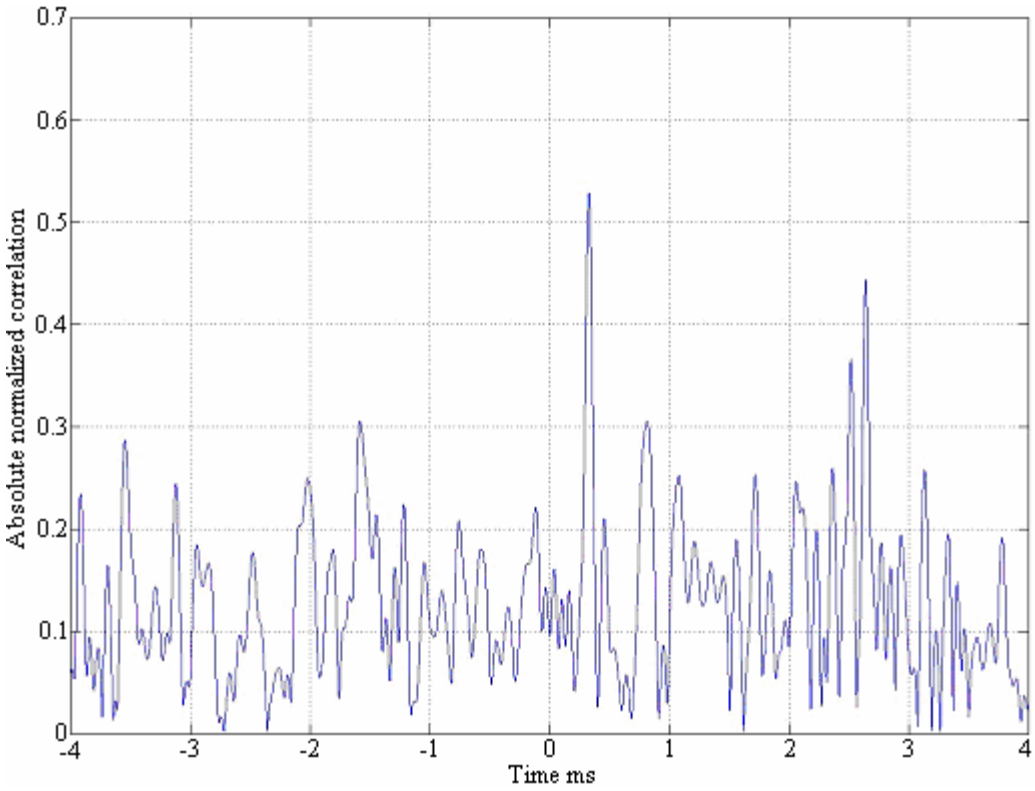

Figure 4.1: $|c_{rs}(\tau)|$ for OFDM signal at a velocity of -5m/s for an ISNR of 10dB

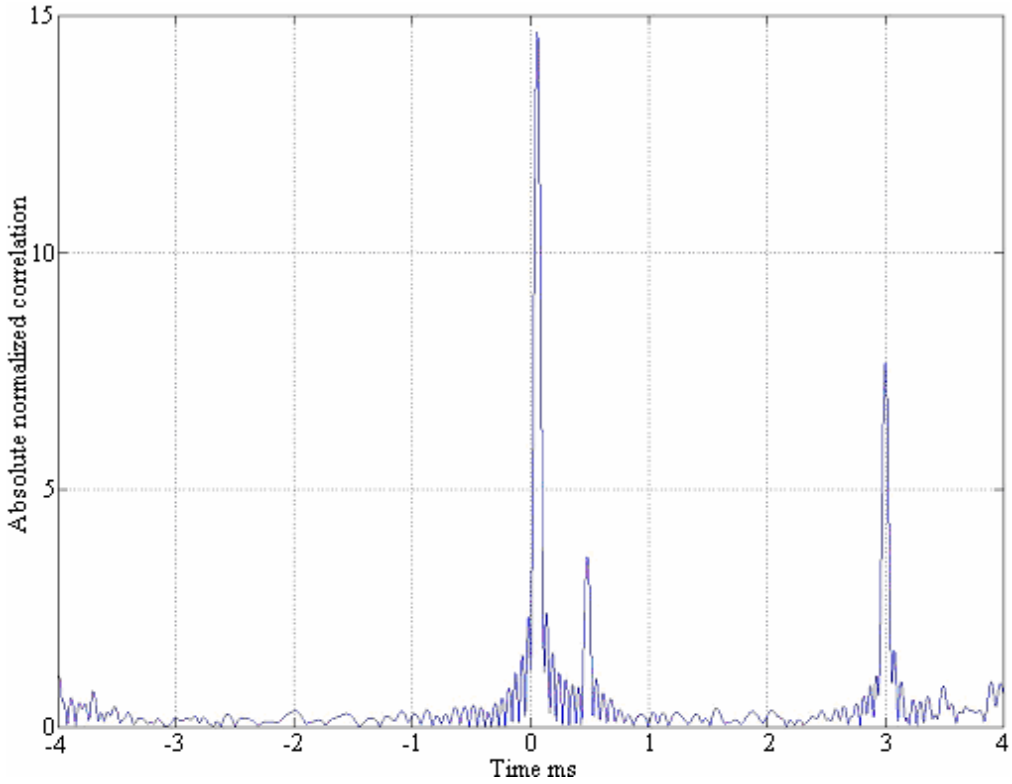

Figure 4.2**:** $|c_{rs}(\tau)|$ for LFM signal at a velocity of -5m/s for an ISNR of 10dB

As the noise is impulsive, deriving the constant false alarm rate (CFAR) would not yield a close-form expression. Instead, we obtain from Table 4.1 the breakdown of η when no signal is present for 10000 Monte Carlo trials. The data is used to compare with the number of occurrences for η with both the OFDM and LFM signal. Empirically, the minimum value obtained for η was 3.72 and 16.14 with the OFDM and LFM signal, respectively. In the absence of a signal, the limit of η was 20

Table 4.1: Windowed cross correlation η between LFM signal and ambient noise.

	Range of η, η > 0									
	< 3	<4	<5	<6	<7	<8	<10	<12	<16	<20
No. of occurences	26	726	3640	7069	8964	9637	9982	9995	9998	10000

Tables 4.2 to 4.4 show the number of occurrences for which η obtained from the cross correlation of the OFDM signal at a transmission range of 50m, 200m and 1km, respectively, was less than 20. Table 4.5, Table 4.6 and Table 4.7 represent that of the LFM signal at the various transmission ranges. Evidently, the number of false detections arising from the usage of the OFDM cross correlation is much higher than that with the LFM signal. At higher speeds, the OFDM based cross correlation performs poorly and is thus unsuitable for signal detection. In contrast, by setting the threshold value for η to 16, all the LFM signals would be detected with a false alarm rate of 0.02%.

Table 4.2: Number of occurrences for η < 20 with OFDM signal at 50m range.

Velocity m/s	ISNR (dB)						
	0	5	10	15	20	25	30
-5.0	10000	9980	9980	9944	9900	9893	9871
-2.0	3413	1201	373	94	32	31	27
0	2170	580	120	4	1	0	0
2.0	3402	1107	380	103	31	30	30
5.0	10000	9984	9982	9942	9903	9894	9873

Table 4.3: Number of occurrences for η < 20 with OFDM signal at 200m range.

Velocity m/s	ISNR (dB)						
	0	5	10	15	20	25	30
-5.0	10000	10000	9983	9961	9960	9958	9955
-2.0	6800	4611	3280	2582	2340	2263	2250
0	4813	2535	1454	1077	940	854	850
2.0	6803	4603	3341	2553	2342	2276	2242
5.0	10000	10000	9891	9960	9958	9956	9951

Table 4.4: Number of occurrences for η < 20 with OFDM signal at 1km range.

Velocity m/s	ISNR (dB)						
	0	5	10	15	20	25	30
-5.0	10000	10000	9993	9993	9992	9983	9973
-2.0	6844	4578	3510	2873	2598	2524	2496
0	5352	2773	1610	1194	1062	1024	990
2.0	6841	4663	3505	2871	2615	2521	2502
5.0	10000	10000	9995	9992	9991	9976	9970

Table 4.5: Number of occurrences for η < 20 with LFM signal at 50m range.

Velocity m/s	ISNR (dB)						
	0	5	10	15	20	25	30
-5.0	18	4	0	0	0	0	0
-2.0	9	2	0	0	0	0	0
0	11	1	0	0	0	0	0
2.0	14	0	0	0	0	0	0
5.0	11	3	0	0	0	0	0

Table 4.6: Number of occurrences for η < 20 with LFM signal at 200m range.

Velocity m/s	ISNR (dB)						
	0	5	10	15	20	25	30
-5.0	36	8	0	0	0	0	0
-2.0	28	5	0	0	0	0	0
0	30	4	0	0	0	0	0
2.0	21	6	0	0	0	0	0
5.0	34	5	1	0	0	0	0

Table 4.7: Number of occurrences for η < 20 with LFM signal at 1km range.

Velocity m/s	ISNR (dB)						
	0	5	10	15	20	25	30
-5.0	41	3	0	0	0	0	0
-2.0	33	5	0	0	0	0	0
0	23	1	0	0	0	0	0
2.0	36	0	0	0	0	0	0
5.0	38	6	0	0	0	0	0

4.2 LFM Signal Detection

Figure 3.2 and Figure 3.3 of the previous chapter show 2 possible arrangements of the LFM signal for Doppler acquisition. The structure in Figure 3.2 is more bandwidth efficient as no null period is required, but may be subjected to poorer estimation due to time-varying Rayleigh fading of the individual arrival paths which are highly time dispersive at short ranges. A method to minimize the impact of the multi-path channel could include a null period before the transmission of the second LFM signal in Figure 3.2 albeit at a loss of bandwidth efficiency. Although a better time resolution would be obtained, Rayleigh fading can still negate the improved accuracy.

4.2.1 LFM Signal Correlation

Assuming a LFM signal has been detected using the method developed in the previous section at time τ_0, a search is then conducted in a similar method by cross correlating T milliseconds of the received signal at τ_0 with the range of expected delay between LFM signals. This range is limited by the maximum expected velocity v_{max}:

$$\left(1-\frac{v_{\max}}{c}\right)T_{tp} \le T_{rp} \le \left(1+\frac{v_{\max}}{c}\right)T_{tp} \tag{4.3}$$

where c is the propagation speed of sound in water. The correlation is done before and after the point where the LFM signal is detected and is expressed as:

$$c_{rr}(T' \mid \tau_0) = \frac{\sum_{n=0}^{T-1} r^*(n+\tau_0)r(n+\tau_0+T')}{\sqrt{\sum_{n=0}^{T-1} r^*(n+\tau_0+T')r(n+\tau_0+T')}} \tag{4.4}$$

A correlation window is once again used to decide if the second LFM signal is detected. Let T'_{peak} represent the point in time within a window where the correlation is maximum, if $|T'_{peak}|$ lies within the criteria stipulated in Eq. (4.3), then the correlation peak is considered to be valid. The probability of false detection for the second LFM signal is hence minimized by having a larger window and a smaller delay range.

4.2.2 Test Parameters

In order to determine the effectiveness of both structures, 1000 Monte Carlo trials were conducted. The LFM signal was once again 4ms long with 20kHz bandwidth centred about a carrier frequency of 50kHz. For the signal structure of Figure 3.2, defined as Structure 1, 4 OFDM symbols of N = 256 and N_p = 64 are used, which yields a delay of 16ms between LFM signals. The null period seen in Figure 3.3 for Structure 2 is 6ms.

4.2.3 Results

Table 4.8 and Table 4.9 show the number of successful detections for Structure 1 and 2, respectively, at a transmission range of 50m. Due to extensive delay spreads, Structure 1 was not able to detect all the signal frames even at high ISNR. On the contrary, Structure 2 shows the benefit of the null period in terms of higher detection rate. The miss rate for both structures, however, is notably higher than the detection method with one LFM signal as two signals have to be successfully detected in this case. Table 4.10 and Table 4.11 show the MSE of the Doppler estimation resulting from the LFM signal. While Structure 1 gave better estimates at negative velocities, Structure 2 showed greater accuracy at positive velocities.

Table 4.8: Number of successful detections at 50m range for Structure 1.

Velocity m/s	ISNR (dB)												
	0	2.5	5	7.5	10	12.5	15	17.5	20	22.5	25	27.5	30
-5.0	623	741	836	905	951	974	977	984	987	988	986	986	986
-2.0	590	724	831	915	946	969	978	982	983	984	984	984	984
0	582	727	829	902	939	967	984	989	991	991	991	991	990
2.0	595	730	847	917	949	971	981	984	982	983	983	983	983
5.0	593	750	844	902	952	968	982	990	991	990	989	988	988

Table 4.9: Number of successful detections at 50m range for Structure 2.

Velocity m/s	ISNR (dB)												
	0	2.5	5	7.5	10	12.5	15	17.5	20	22.5	25	27.5	30
-5.0	782	850	904	958	981	993	997	1000	1000	1000	1000	1000	1000
-2.0	796	842	925	976	996	998	1000	1000	1000	1000	1000	1000	1000
0	769	869	945	980	994	998	1000	1000	1000	1000	1000	1000	1000
2.0	787	865	933	970	996	998	1000	1000	1000	1000	1000	1000	1000
5.0	795	828	884	949	974	992	997	1000	1000	1000	1000	1000	1000

Table 4.10: Doppler MSE ε with LFM Signal at f_s=640kHz for Structure 1.

Velocity m/s	Doppler MSE $\varepsilon = \left(\Delta - \hat{\Delta}_1\right)^2$ at different ISNR (dB)						
	0	5	10	15	20	25	30
-5.0	$1.63*10^{-7}$	$4.25*10^{-8}$	$1.60*10^{-8}$	$1.55*10^{-8}$	$1.52*10^{-8}$	$1.52*10^{-8}$	$1.51*10^{-8}$
-2.0	$9.49*10^{-8}$	$5.11*10^{-8}$	$1.09*10^{-8}$	$1.04*10^{-8}$	$1.03*10^{-8}$	$1.03*10^{-8}$	$1.03*10^{-8}$
0	$9.79*10^{-8}$	$2.07*10^{-8}$	$9.66*10^{-9}$	$3.92*10^{-11}$	$1.92*10^{-11}$	0	0
2.0	$1.20*10^{-7}$	$7.62*10^{-10}$	$2.26*10^{-10}$	$9.99*10^{-11}$	$2.11*10^{-11}$	$2.11*10^{-11}$	$2.11*10^{-11}$
5.0	$1.57*10^{-7}$	$2.36*10^{-8}$	$2.03*10^{-8}$	$5.15*10^{-10}$	$4.00*10^{-10}$	$3.06*10^{-10}$	$3.06*10^{-10}$

Table 4.11: Doppler MSE ε with LFM Signal at f_s=640kHz for Structure 2.

Velocity m/s	Doppler MSE $\varepsilon = \left(\Delta - \hat{\Delta}_1\right)^2$ at different ISNR (dB)						
	0	5	10	15	20	25	30
-5.0	$3.97*10^{-7}$	$1.44*10^{-7}$	$2.06*10^{-8}$	$5.61*10^{-9}$	$4.13*10^{-9}$	$4.02*10^{-9}$	$4.02*10^{-9}$
-2.0	$3.11*10^{-7}$	$1.51*10^{-7}$	$4.72*10^{-8}$	$1.49*10^{-8}$	$8.32*10^{-9}$	$6.87*10^{-9}$	$5.06*10^{-9}$
0	$2.20*10^{-7}$	$7.04*10^{-8}$	$1.69*10^{-8}$	$3.19*10^{-9}$	0	0	0
2.0	$3.38*10^{-7}$	$1.14*10^{-7}$	$5.25*10^{-8}$	$1.73*10^{-8}$	$7.17*10^{-9}$	$5.67*10^{-9}$	$5.62*10^{-9}$
5.0	$2.15*10^{-7}$	$7.36*10^{-8}$	$1.92*10^{-8}$	$6.12*10^{-9}$	$1.75*10^{-9}$	$1.75*10^{-9}$	$1.75*10^{-9}$

4.3 Timing Synchronization

Timing synchronization is pertinent in OFDM to minimize errors due to ISI. If the delay spread is shorter than the cyclic prefix, or if a cyclic suffix is included, then a greater margin of error is allowed for ISI free communications [17]. However, inclusion of a cyclic suffix results in lower bandwidth efficiency, while the extensive delay spread of the channel at short range transmission inhibits having the symbol start timing within the cyclic prefix.

4.3.1 Channel Estimation with LFM Signals

In the previous section, we have established the method of signal detection by cross-correlation of the received signal with a known LFM signal. Due to the assumption of Rayleigh fading on individual arrival paths, the first peak observed as shown in Figure 4.2 may not necessarily always be the strongest path. For example, should the arrival path represented by the peak at 3ms of Figure 4.2 be of higher amplitude and taken as the point of symbol synchronization, then a cyclic suffix of 60 samples will be required for ISI free communications.

A method to minimize such errors in timing is to include a roll-back period to search for a peak in the correlation function. From the studies done in [5], the first reflected arrivals tend to be strong; also, short range communication exhibits the largest delay between the first arrival and first reflected arrival. This delay is typically within 2ms, hence the time period taken for roll-back. In addition, a minimum threshold of -3dB is imposed upon the amplitude of the correlation peaks within the roll-back period to be considered as valid path arrivals.

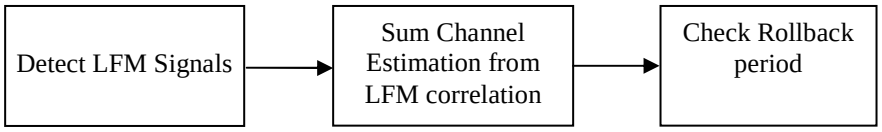

Figure 4.3**:** Schematic for Channel Estimation with LFM signals

Figure 4.3 shows the schematic for estimating the first arrival path. The cross-correlation between the 2 received LFM signals and the original LFM signal is summed together to improve detection. The window of correlation takes into account the rollback period which is then checked for peaks that are at least -3dB of the maximum peak detected. The first peak that surpasses the threshold within the rollback period is considered to be the first arrival.

Table 4.12: RMS error of timing synchronization with LFM signals at 50m range.

Velocity m/s	ISNR (dB)						
	0	5	10	15	20	25	30
-5.0	11.60	7.52	5.31	3.78	3.03	3.02	2.89
-2.0	12.97	9.20	7.24	5.37	4.66	4.62	4.49
0	10.44	7.70	4.07	2.86	2.35	2.35	2.48
2.0	13.68	9.71	7.64	5.66	4.91	4.88	4.73
5.0	11.05	7.17	5.06	3.60	2.88	2.87	2.76

Table 4.13: RMS error of timing synchronization with LFM signals at 200m range.

Velocity m/s	ISNR (dB)						
	0	5	10	15	20	25	30
-5.0	10.08	4.89	3.11	2.25	1.09	0.88	0.88
-2.0	12.66	6.61	3.75	1.53	0.81	0.48	0.47
0	12.53	6.59	4.52	2.38	0.43	0.44	0.44
2.0	13.63	7.12	4.04	1.65	0.87	0.51	0.50
5.0	10.66	5.18	3.29	2.38	1.15	0.93	0.93

Table 4.14: RMS error of timing synchronization with LFM signals at 1km range.

Velocity m/s	ISNR (dB)						
	0	5	10	15	20	25	30
-5.0	11.02	6.16	2.10	1.19	0.90	0.70	0.71
-2.0	10.87	5.64	2.69	1.92	1.01	0.59	0.58
0	11.37	5.53	5.06	2.13	1.31	0.79	0.80
2.0	11.70	6.07	2.90	2.06	1.08	0.64	0.62
5.0	11.66	6.51	2.22	1.25	0.95	0.74	0.75

A simulation test was conducted with Structure 2 LFM signals using the same parameters as the previous section and 2000 Monte Carlo trials. Table 4.12 to 4.14 show the RMS error of timing synchronization in terms of OFDM samples at various transmission ranges. The MSE tends to be high at short range transmission as the delay spread is higher, but stabilises from 200m onwards.

4.3.2 Timing Synchronization with OFDM Cyclic Prefix

To compare the effectiveness of using this method for timing synchronization, we conduct a test using the OFDM cyclic prefix to obtain the symbol start timing. Chitre [5] has shown that the cyclic prefix is able to perform accurate timing synchronization *between* OFDM symbols; however there is no conclusive evidence that the synchronization is locked upon the arrival of the first path. Van de Beek et. al [44] has shown however that timing synchronization deteriorates under multi-path channel conditions. From structure 2, the 8 OFDM symbols of N = 256 and N_p = 64 are used to measure the accuracy of symbol timing within the same 2000 Monte Carlo trials. The symbol timing obtained from averaging the OFDM CP correlation in a signal frame is expressed as:

$$\hat{\tau} = \arg\max_{\tau}\left(c'_{rr}(\tau)\right) \tag{4.5}$$

where $c'_{rr}(\tau)$ is obtained from Eq. (3.20). From Table 4.15, Table 4.16 and Table 4.17, we observe that the symbol timing RMS error is higher at all transmission ranges and velocities than using the LFM signals to estimate the channel for the first arrival. Hence, we can conclude that the proposed method with LFM signals for timing synchronization is more effective.

Table 4.15: RMS error of timing synchronization with OFDM CP at 50m range.

Velocity m/s	ISNR (dB)						
	0	5	10	15	20	25	30
-5.0	22.63	14.93	12.48	10.72	9.67	9.69	9.47
-2.0	26.07	19.57	14.23	12.73	11.41	11.28	10.61
0	18.78	11.86	7.35	5.36	4.21	4.19	4.59
2.0	25.22	17.00	14.60	13.62	13.50	12.86	12.30
5.0	19.58	11.83	9.49	8.12	7.81	7.80	7.81

Table 4.16: RMS error of timing synchronization with OFDM CP at 200m range.

Velocity m/s	ISNR (dB)						
	0	5	10	15	20	25	30
-5.0	20.54	10.32	5.18	5.08	3.90	3.13	3.09
-2.0	26.62	15.99	9.25	7.40	6.42	5.91	5.79
0	21.50	10.68	5.76	2.34	0.66	0.66	0.66
2.0	27.06	14.96	9.18	4.81	4.39	4.23	4.23
5.0	21.73	10.92	5.47	5.38	4.13	3.31	3.27

Table 4.17: RMS error of timing synchronization with OFDM CP at 1km range.

Velocity m/s	ISNR (dB)						
	0	5	10	15	20	25	30
-5.0	25.95	14.05	5.71	2.85	1.85	1.56	1.56
-2.0	27.77	15.17	6.41	3.97	1.36	1.36	1.36
0	24.06	11.76	6.27	4.52	2.74	1.44	1.44
2.0	28.51	14.81	6.52	4.33	3.18	1.50	1.49
5.0	20.41	11.49	4.26	2.35	2.35	1.28	1.28

4.4 Conclusion

In this chapter, we have determined that, without prior knowledge of the velocity at which mobile communications is conducted underwater, LFM signals are more robust than OFDM symbols for signal detection. Doppler induced time scaling of the signal results in a shift in frequency at a given time instance, hence it is more insensitive to mobility.

The structure for transmitting the LFM signals was chosen based upon bandwidth efficiency, accuracy of estimates as well as rate of detection. Having a short null period between LFM signals is found to be the better solution instead of attaching an LFM signal to both the start and end of the OFDM symbols, which makes detection very susceptible to long delay spreads. In addition, the accuracy of Doppler estimation was similar in both instances, which puts the latter structure at a further disadvantage.

The LFM signals are also utilized for estimation of path arrivals in the UWA channel. Given the fact that the correlation peak from match filtering may not correspond to the first path arrival, a roll back period is implemented with a search threshold of -3dB of the initial peak detected. This detection scheme results in lower error of estimation in comparison to the cyclic prefix method.

5. Single Channel UWA Wireless Communications

In the previous chapters, we identified the main challenges of acoustic communications under mobility conditions. Short coherence time impedes the symbol length for OFDM, yet a narrow coherence bandwidth limits that of each sub-carrier used. Mobility-induced Doppler effects requires compensation beyond that of a carrier frequency offset, whilst lengthy delay spreads with individual Rayleigh fades on individual arrival paths affects timing synchronization. In this chapter, we take into account these factors and implement the signal framework as well as receiver schematics for UWA wireless communications.

5.1 Signal Framework

In reality, acoustic transmitters have a maximum duration of transmission. In this thesis we assume that the duration is to be within 0.4s[*] and thus attempt to maximize the signal bandwidth within this period.

5.1.1 LFM Signal Structure

In Chapter 2, we observed that delay spreads of up to 7ms is possible in the real channel. In the course of simulations conducted in the previous chapter, it is shown that a null period of 6ms embedded within two LFM signals of 4ms duration and 20kHz bandwidth resulted in acceptable detection rates and Doppler estimation errors. Hence, the same structure is retained for the LFM signals, occupying a total duration of 14ms.

[*] The duration is obtained from the specifications of the transducer used by Chitre in his experimentations.

5.1.2 OFDM Signal Structure

Using a signal bandwidth of B_s = 20kHz, the OFDM symbol is constrained by the coherence bandwidth, coherence time and delay spread found in Chapter 2. To have acceptable DPSK communications, the OFDM symbol length must lie within half of the minimum coherence time of T_c = 47ms. Assuming moderate delay spreads at medium range (560m), a cyclic prefix length that is at least τ_{ds} = 3ms long would be required. At this delay spread, a coherence bandwidth of 141Hz is imposed upon each sub-carrier.

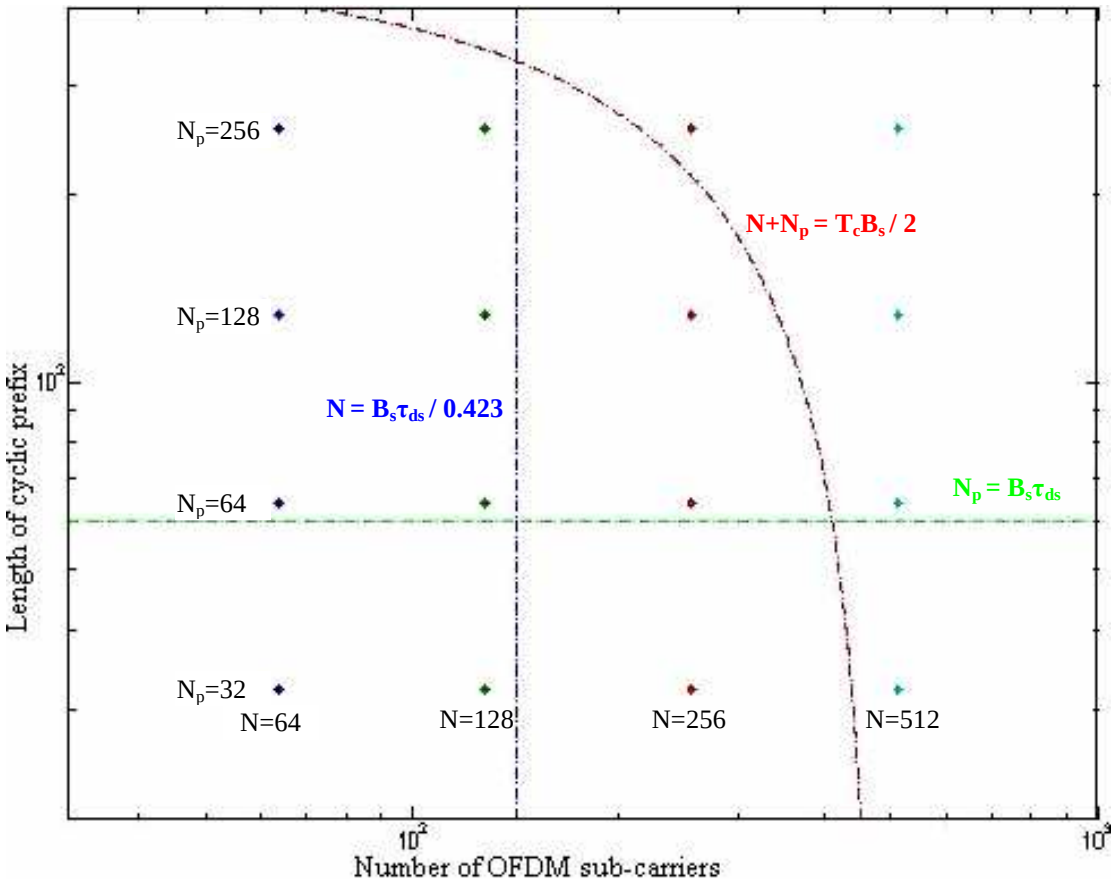

Figure 5.1**:** Viable zone for number of OFDM sub-carriers and cyclic prefix length

From Figure 5.1, two possible sub-carrier and cyclic prefix combinations lie within the constraint boundaries. To maximise bandwidth efficiency, the combination of N = 256 sub-carriers and N_p = 62 is chosen with a suffix of N_s = 2 allowed for timing errors.

Thus, each OFDM symbol is 16ms in duration. Given the constraint upon transmission duration as well as the duration for LFM signal transmission, a total of 24 OFDM symbols can be transmitted.

5.1.3 Data and Signal Modulation Parameters

The pilot OFDM symbols are evenly distributed once every 8 symbols for both DPSK and QPSK modulation schemes presented in Chapter 3. For QPSK, the angular update coefficient β_ϕ is chosen to be 0.8 while the update coefficient for equalizer tap weights β_ω is 0.7 for pilot symbols and 0.1 when in data decision mode. Figure 5.2 shows the signal frame to be used for testing the communications system. From [5], it is found that the ideal carrier frequency is located at f_c = 50kHz.

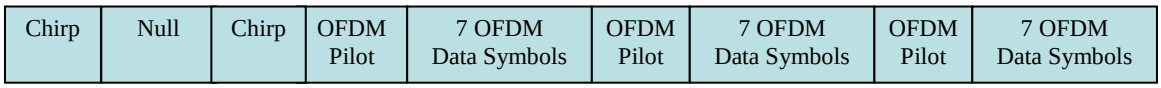

Figure 5.2**:** Proposed signal frame structure

5.2 Receiver Structure

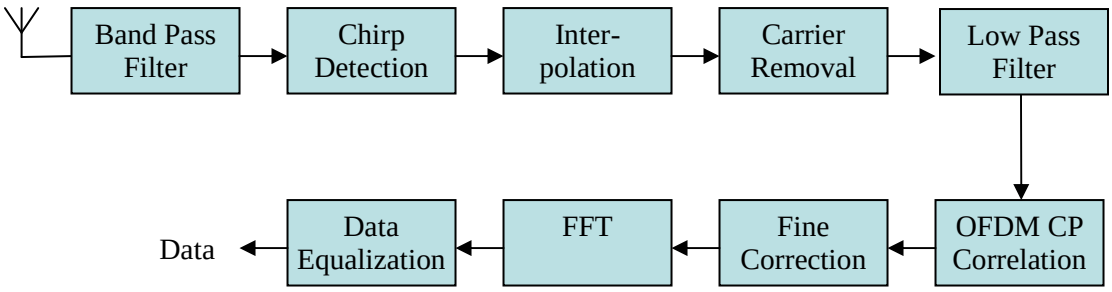

Figure 5.3**:** Schematic of single channel receiver structure

Figure 5.3 represents the receiver structure for the communications system. Incoming signals are first over-sampled at f_s = 640kHz then band pass filtered about the carrier frequency within the bandwidth of transmission. Care has to be taken to ensure

that the bandwidth of the filter is larger than that of the signal due to Doppler spreading and shifting of the frequency spectrum. Given a maximum speed of 5 m/s between the mobile transmitters and receivers and a propagation speed of 1500 m/s, the signal frame developed does not exceed more than 1kHz in the frequency spectrum of 40kHz to 60kHz. Hence, the filter should be designed to have a cut-off frequency at 39kHz and 61kHz. The LFM signal detection and interpolation is hence done in passband. Detection encompasses Doppler acquisition as well as symbol synchronization of the received signal to the first, *detectable* arrival path from which linear interpolation is performed.

The signal is then down-converted to baseband via carrier multiplication followed by low pass filtering. The low pass filter can be designed to have a cut-off frequency at 10kHz as linear interpolation would have corrected most of the Doppler spread and shift of the frequency spectrum. From the correlation of OFDM cyclic prefixes, the residual error in Doppler is detected. A priori, the fine correction would only require CFO compensation. However, initial tests reveal that the data constellation spreads as seen in Figure 5.4 for the in-phase & quadrature (I-Q) data plots obtained from the 1st and 7th OFDM data symbol. A second stage of interpolation is thus included as part of the fine correction in Figure 5.3 to compensate for the spreading constellation.

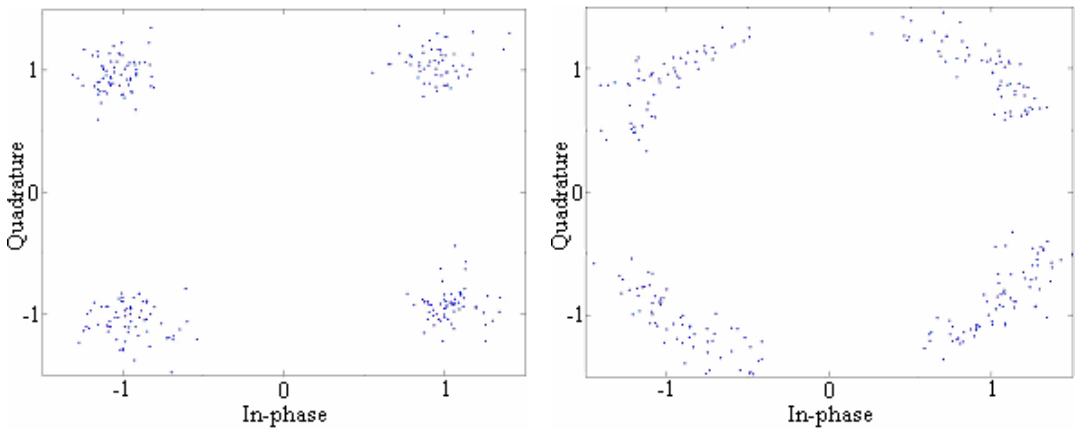

(a) (b)

Figure 5.4**:** I-Q plots for (a) 1st OFDM data symbol (b) 7th OFDM data symbol simulated at transmission range of 1km and ISNR of 30dB

FFT is performed for each pilot and data symbol received after down-sampling. The data samples obtained after FFT demodulation are subsequently equalized via DPSK and QPSK using the parameters in the previous section and the method presented in Chapter 3. The output from the equalizers is the received data.

5.3 Single Channel Simulation

Channel simulations were conducted at transmission ranges of 50m, 200m and 1000m using Doppler spreads of B_d = 9Hz, 6Hz and 3Hz, respectively. The Doppler spread governs the coherence fading time under the assumption that $T_c = 1/B_d$. A total of 2000 Monte Carlo trials were conducted. From Tables 5.1 to 5.3, the rate of detection observed is consistent across the different transmission ranges for any given ISNR.

Table 5.1: Number of successful detections at 50m range.

Velocity	ISNR (dB)						
m/s	0	5	10	15	20	25	30
-5.0	1688	1915	1984	1993	2000	2000	2000
-2.0	1724	1924	1978	1998	2000	2000	2000
0	1730	1936	1986	2000	2000	2000	2000
2.0	1789	1954	1992	1998	2000	2000	2000
5.0	1717	1911	1983	1995	1998	2000	2000

Table 5.2: Number of successful detections at 200m range.

Velocity	ISNR (dB)						
m/s	0	5	10	15	20	25	30
-5.0	1721	1906	1987	1998	2000	2000	2000
-2.0	1759	1935	1989	1998	2000	2000	2000
0	1736	1930	1992	1998	2000	2000	2000
2.0	1768	1944	1995	2000	2000	2000	2000
5.0	1699	1902	1974	2000	2000	2000	2000

Table 5.3: Number of successful detections at 1000m range.

Velocity m/s	ISNR (dB)						
	0	5	10	15	20	25	30
-5.0	1694	1917	1984	1998	2000	2000	2000
-2.0	1702	1930	1995	2000	2000	2000	2000
0	1727	1932	1989	2000	2000	2000	2000
2.0	1753	1947	1993	2000	2000	2000	2000
5.0	1687	1917	1992	2000	2000	2000	2000

The error in signal timing synchronization, shown in Tables 5.4 to 5.6, is measured in terms of OFDM samples. Higher errors are observed at short range transmission compared to medium and long range transmissions. This is due to the extensive delay spread at short ranges, resulting in a higher probability of ISI.

Tables 5.7 to 5.9 show that, despite having a longer cyclic prefix and more OFDM symbols, Doppler MSEs obtained over the average of the signal frame saturate at the order of 10^{-11} at high ISNR, which is higher than those obtained from Test 3.4 in Chapter 3. The increment in error is most likely due to time varying Rayleigh fading which affected the accuracy of the estimation.

Table 5.4: Single channel RMS error of timing synchronization at 50m range.

Velocity m/s	ISNR (dB)						
	0	5	10	15	20	25	30
-5.0	11.20	6.91	4.81	3.09	2.12	2.10	1.87
-2.0	15.29	11.48	8.41	6.26	4.89	4.88	4.59
0	10.44	7.70	4.07	2.86	2.35	2.35	2.48
2.0	11.94	7.84	6.81	5.01	4.89	4.83	4.83
5.0	12.01	8.14	5.82	3.46	2.94	2.93	2.92

Table 5.5: Single channel RMS error of timing synchronization at 200m range.

Velocity m/s	ISNR (dB)						
	0	5	10	15	20	25	30
-5.0	10.92	5.58	3.45	1.71	0.89	0.59	0.58
-2.0	12.21	6.90	4.00	2.63	1.12	0.43	0.41
0	12.53	6.59	4.52	2.38	0.43	0.44	0.44
2.0	14.38	6.98	3.87	0.57	0.58	0.57	0.57
5.0	9.34	4.25	2.80	2.82	0.90	0.48	0.48

Table 5.6: Single channel RMS error of timing synchronization at 1km range.

Velocity m/s	ISNR (dB)						
	0	5	10	15	20	25	30
-5.0	12.69	7.09	2.11	1.25	0.66	0.67	0.68
-2.0	10.94	5.93	3.01	1.86	0.59	0.58	0.57
0	11.37	5.53	5.06	2.13	1.31	0.79	0.80
2.0	11.88	5.91	2.63	2.16	1.53	0.66	0.64
5.0	9.46	4.28	2.11	1.13	1.04	0.74	0.75

Table 5.7: Single channel Doppler MSE ε at 50m range.

Velocity m/s	Doppler MSE $\varepsilon = \left(\Delta - \hat{\Delta}_1\right)^2$ at different ISNR (dB)						
	0	5	10	15	20	25	30
-5.0	$8.89*10^{-8}$	$6.56*10^{-8}$	$1.26*10^{-8}$	$4.91*10^{-9}$	$4.83*10^{-9}$	$4.07*10^{-9}$	$4.07*10^{-9}$
-2.0	$7.63*10^{-8}$	$3.77*10^{-8}$	$1.06*10^{-8}$	$6.85*10^{-9}$	$6.02*10^{-9}$	$5.22*10^{-9}$	$5.20*10^{-9}$
0	$4.49*10^{-8}$	$2.71*10^{-8}$	$8.53*10^{-9}$	$3.10*10^{-9}$	$1.56*10^{-9}$	0	0
2.0	$6.87*10^{-8}$	$2.55*10^{-8}$	$9.62*10^{-9}$	$6.69*10^{-9}$	$5.88*10^{-9}$	$5.86*10^{-9}$	$5.85*10^{-9}$
5.0	$7.67*10^{-8}$	$3.43*10^{-8}$	$4.08*10^{-9}$	$1.79*10^{-9}$	$1.76*10^{-9}$	$1.75*10^{-9}$	$1.75*10^{-9}$
Velocity m/s	Doppler MSE $\varepsilon = \left(\Delta - \hat{\Delta}_1 - \hat{\Delta}_2\right)^2$ at different ISNR (dB)						
	0	5	10	15	20	25	30
-5.0	$1.26*10^{-7}$	$8.56*10^{-8}$	$1.31*10^{-8}$	$2.00*10^{-9}$	$3.92*10^{-11}$	$1.36*10^{-11}$	$1.35*10^{-11}$
-2.0	$1.59*10^{-7}$	$7.15*10^{-8}$	$1.14*10^{-8}$	$3.75*10^{-9}$	$1.87*10^{-10}$	$2.96*10^{-11}$	$2.90*10^{-11}$
0	$9.76*10^{-8}$	$5.34*10^{-8}$	$1.55*10^{-8}$	$9.23*10^{-10}$	$3.69*10^{-10}$	$1.74*10^{-11}$	$1.70*10^{-11}$
2.0	$1.32*10^{-7}$	$4.53*10^{-8}$	$9.28*10^{-9}$	$1.86*10^{-9}$	$2.66*10^{-11}$	$2.53*10^{-11}$	$2.49*10^{-11}$
5.0	$1.27*10^{-7}$	$4.63*10^{-8}$	$5.82*10^{-9}$	$1.53*10^{-10}$	$1.47*10^{-11}$	$1.46*10^{-11}$	$1.45*10^{-11}$

Table 5.8: Single channel Doppler MSE ε at 200m range.

Velocity m/s	Doppler MSE $\varepsilon = \left(\Delta - \hat{\Delta}_1\right)^2$ at different ISNR (dB)						
	0	5	10	15	20	25	30
-5.0	$3.94*10^{-8}$	$2.27*10^{-8}$	$5.88*10^{-9}$	$4.22*10^{-9}$	$4.13*10^{-9}$	$4.09*10^{-9}$	$4.08*10^{-9}$
-2.0	$1.04*10^{-7}$	$3.78*10^{-8}$	$1.69*10^{-8}$	$6.66*10^{-9}$	$6.80*10^{-9}$	$6.00*10^{-9}$	$5.24*10^{-9}$
0	$5.88*10^{-8}$	$2.15*10^{-8}$	$7.61*10^{-9}$	$1.34*10^{-9}$	0	0	0
2.0	$8.04*10^{-8}$	$3.84*10^{-8}$	$1.87*10^{-8}$	$6.70*10^{-9}$	$5.89*10^{-9}$	$5.87*10^{-9}$	$5.87*10^{-9}$
5.0	$2.53*10^{-8}$	$1.27*10^{-8}$	$4.59*10^{-9}$	$4.71*10^{-9}$	$2.47*10^{-9}$	$1.75*10^{-9}$	$1.75*10^{-9}$
Velocity m/s	Doppler MSE $\varepsilon = \left(\Delta - \hat{\Delta}_1 - \hat{\Delta}_2\right)^2$ at different ISNR (dB)						
	0	5	10	15	20	25	30
-5.0	$7.14*10^{-8}$	$3.53*10^{-8}$	$3.83*10^{-9}$	$1.26*10^{-10}$	$1.24*10^{-11}$	$1.24*10^{-11}$	$1.24*10^{-11}$
-2.0	$1.57*10^{-7}$	$6.64*10^{-8}$	$2.40*10^{-8}$	$2.14*10^{-9}$	$7.54*10^{-11}$	$3.80*10^{-11}$	$2.11*10^{-11}$
0	$9.69*10^{-8}$	$3.67*10^{-8}$	$1.88*10^{-8}$	$3.71*10^{-10}$	$1.50*10^{-11}$	$1.45*10^{-11}$	$1.43*10^{-11}$
2.0	$1.45*10^{-7}$	$6.97*10^{-8}$	$2.98*10^{-8}$	$1.88*10^{-10}$	$1.95*10^{-11}$	$1.88*10^{-11}$	$1.87*10^{-11}$
5.0	$5.11*10^{-8}$	$2.39*10^{-8}$	$7.69*10^{-9}$	$7.61*10^{-10}$	$3.98*10^{-10}$	$1.42*10^{-11}$	$1.42*10^{-11}$

Table 5.9: Single channel Doppler MSE ε at 1km range.

Velocity m/s	Doppler MSE $\varepsilon = \left(\Delta - \hat{\Delta}_1\right)^2$ at different ISNR (dB)						
	0	5	10	15	20	25	30
-5.0	$1.65*10^{-7}$	$8.73*10^{-8}$	$9.82*10^{-9}$	$5.58*10^{-9}$	$4.78*10^{-9}$	$4.02*10^{-9}$	$4.01*10^{-9}$
-2.0	$8.00*10^{-8}$	$3.89*10^{-8}$	$1.38*10^{-8}$	$9.12*10^{-9}$	$5.12*10^{-9}$	$5.06*10^{-9}$	$5.03*10^{-9}$
0	$5.61*10^{-8}$	$3.11*10^{-8}$	$1.25*10^{-8}$	$4.43*10^{-9}$	$1.56*10^{-9}$	0	0
2.0	$7.90*10^{-8}$	$3.51*10^{-8}$	$1.50*10^{-8}$	$8.88*10^{-9}$	$7.28*10^{-9}$	$5.68*10^{-9}$	$5.66*10^{-9}$
5.0	$3.29*10^{-8}$	$1.42*10^{-8}$	$5.71*10^{-9}$	$2.50*10^{-9}$	$2.48*10^{-9}$	$1.75*10^{-9}$	$1.75*10^{-9}$
Velocity m/s	Doppler MSE $\varepsilon = \left(\Delta - \hat{\Delta}_1 - \hat{\Delta}_2\right)^2$ at different ISNR (dB)						
	0	5	10	15	20	25	30
-5.0	$2.17*10^{-7}$	$1.09*10^{-7}$	$7.92*10^{-9}$	$3.93*10^{-10}$	$2.02*10^{-11}$	$7.79*10^{-11}$	$7.74*10^{-11}$
-2.0	$1.58*10^{-7}$	$6.01*10^{-8}$	$2.11*10^{-8}$	$9.62*10^{-10}$	$2.52*10^{-11}$	$2.53*10^{-11}$	$2.53*10^{-11}$
0	$1.28*10^{-7}$	$6.22*10^{-8}$	$1.96*10^{-8}$	$1.15*10^{-8}$	$3.91*10^{-10}$	$4.95*10^{-12}$	$4.84*10^{-12}$
2.0	$1.68*10^{-7}$	$6.68*10^{-8}$	$1.74*10^{-8}$	$7.71*10^{-9}$	$3.82*10^{-9}$	$8.25*10^{-12}$	$7.52*10^{-12}$
5.0	$7.19*10^{-8}$	$3.05*10^{-8}$	$9.68*10^{-9}$	$2.09*10^{-10}$	$2.09*10^{-10}$	$1.52*10^{-10}$	$1.52*10^{-10}$

Figures 5.5 to 5.10 show the BER at various velocities and transmission range for both DPSK and QPSK data modulation. QPSK performs slightly better under low ISNR ratio, but is overtaken by the performance of DPSK from 15dB onwards. At the upper ranges of ISNR, BER is observed to be poorer for short range transmission. This is most likely due to the fact that the length of delay spread reduces with increasing distance in transmission until it is shorter than the cyclic prefix, resulting in ISI free demodulation. Also, the symbol timing error is more significant at short range, thus even a cyclic suffix of 2 OFDM samples may not be sufficient to demodulate the OFDM symbol within the ISI free region.

The reduction in BER reaches a threshold that is more evident at short range transmission. This could possibly be due to the threshold in CFO estimation error using the OFDM cyclic prefixes, hence introducing ICI even as ISNR increases. Also, the time-varying nature of Rayleigh fading is more acute at short range transmission. Since the ISNR is measured based on the deterministic ratio in variance of the received signal and impulsive noise, certain OFDM symbols located in deep fades will result in numerous data symbol errors upon demodulation. As a result, DPSK tends to suffer a penalty in performance when the overall ISNR is low.

An ISNR of more than 25 dB is expected at 50m transmission range. At 200m and 1km range, the anticipated range would be 15 to 25 dB and 5 to 15 dB, respectively. Therefore, QPSK is more suitable at 1km whilst DPSK is better for the shorter ranges. A BER performance in the order of 10^{-2} is guaranteed for the 3 different ranges of transmission under the given UWA channel condition at different velocities of communication. The effective bandwidth of the system is 27,015 bps.

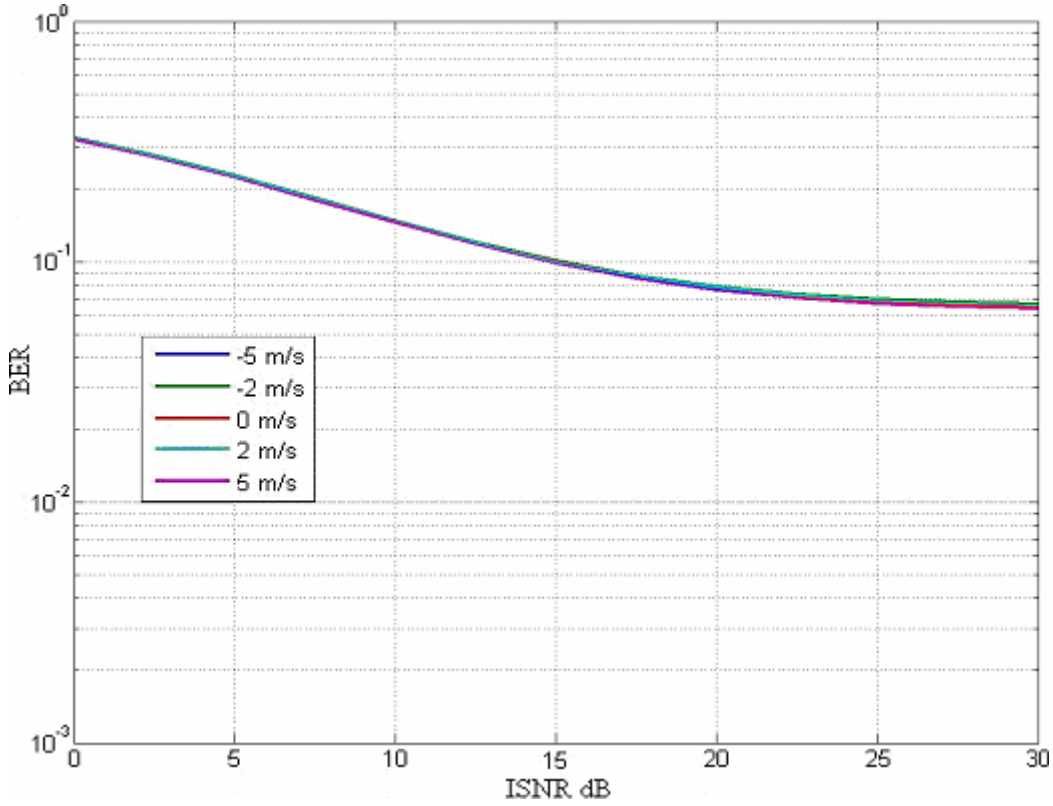

Figure 5.5**:** Single channel BER using DPSK at 50m transmission range

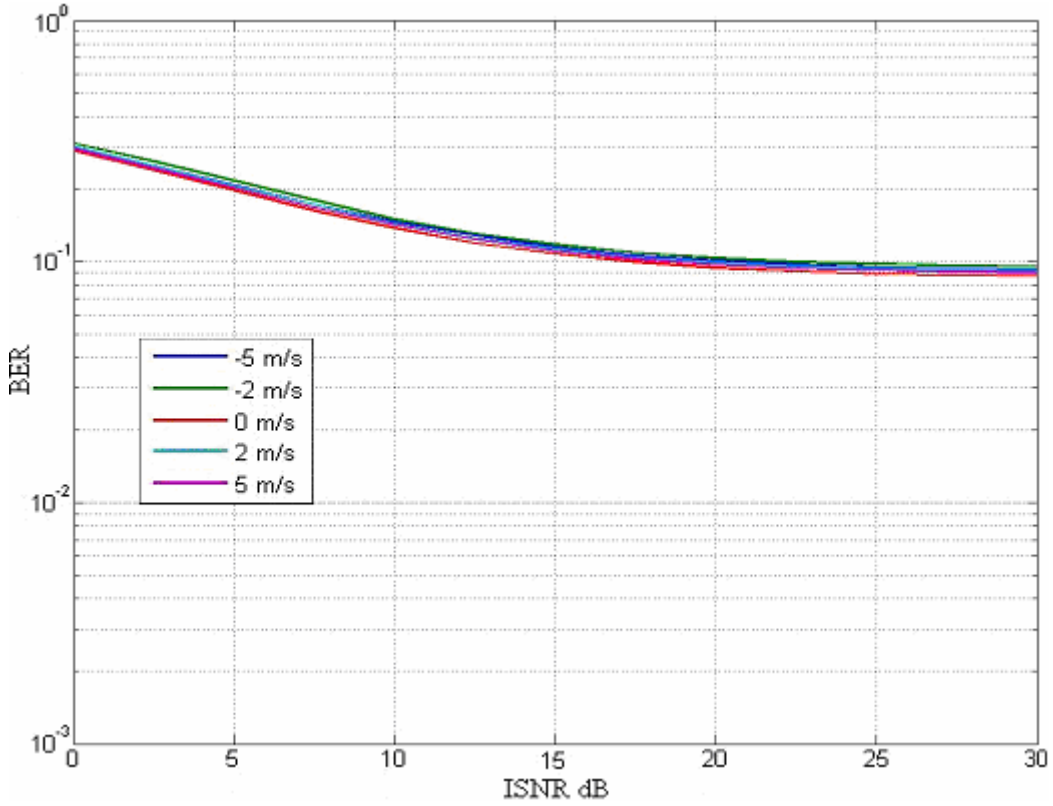

Figure 5.6**:** Single channel BER using QPSK at 50m transmission range

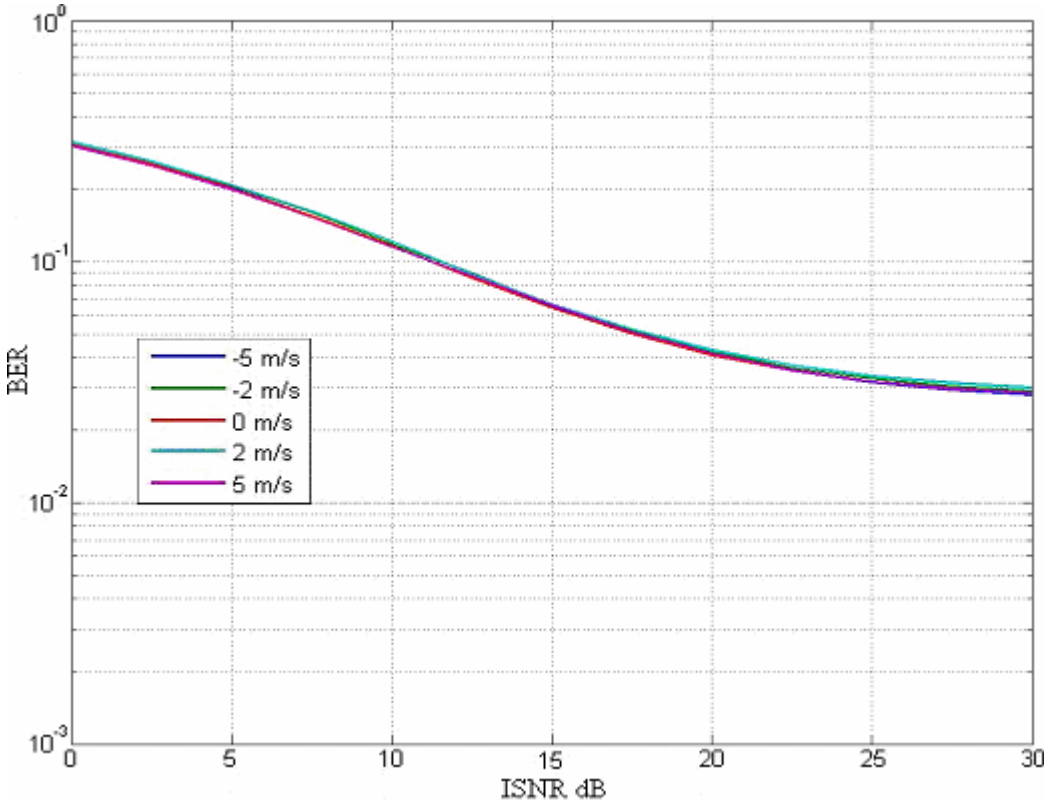

Figure 5.7**:** Single channel BER using DPSK at 200m transmission range

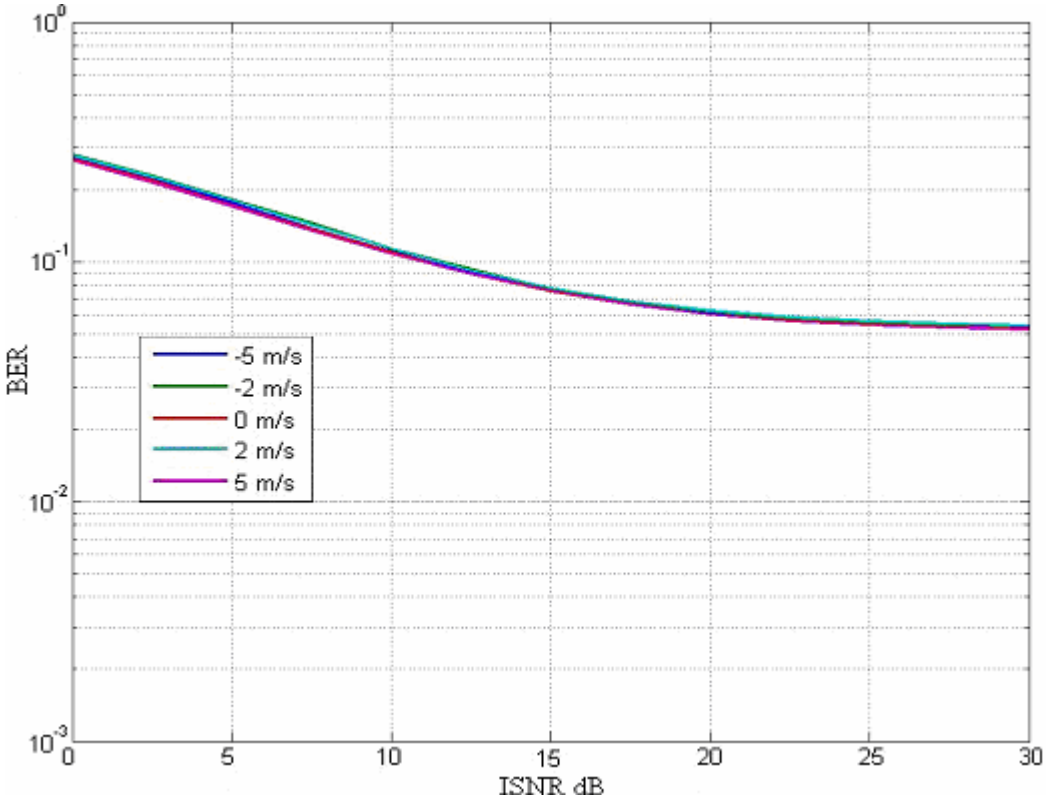

Figure 5.8**:** Single channel BER using QPSK at 200m transmission range

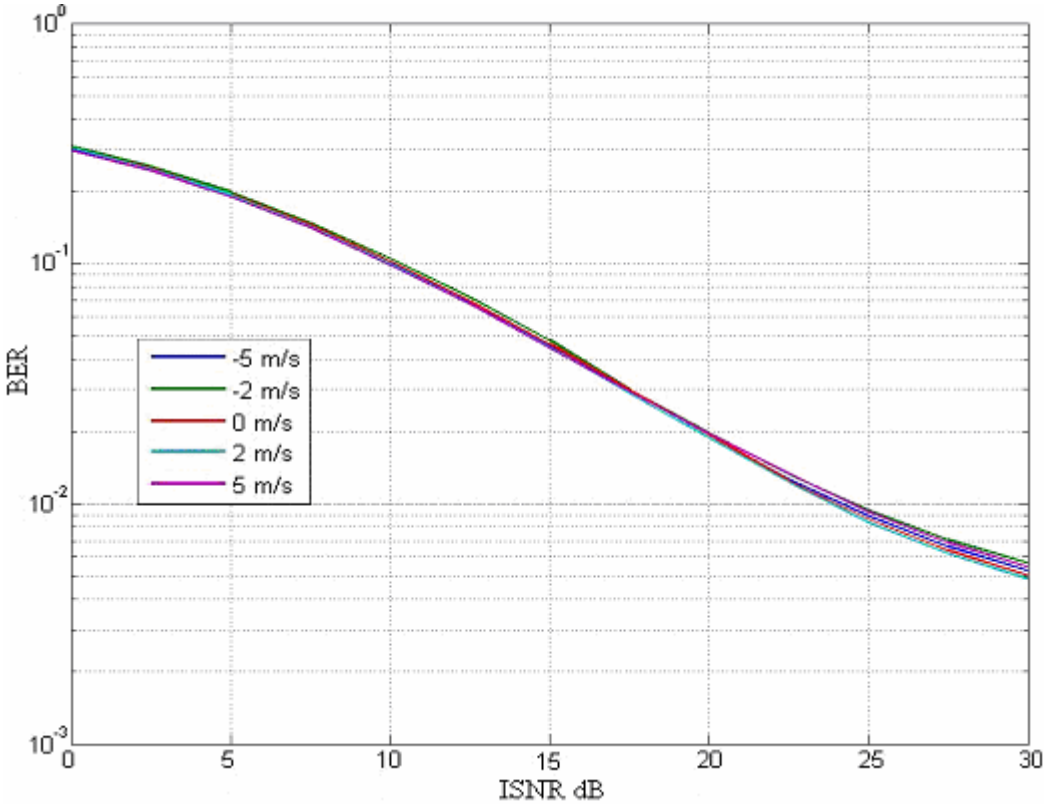

Figure 5.9**:** Single channel BER using DPSK at 1km transmission range

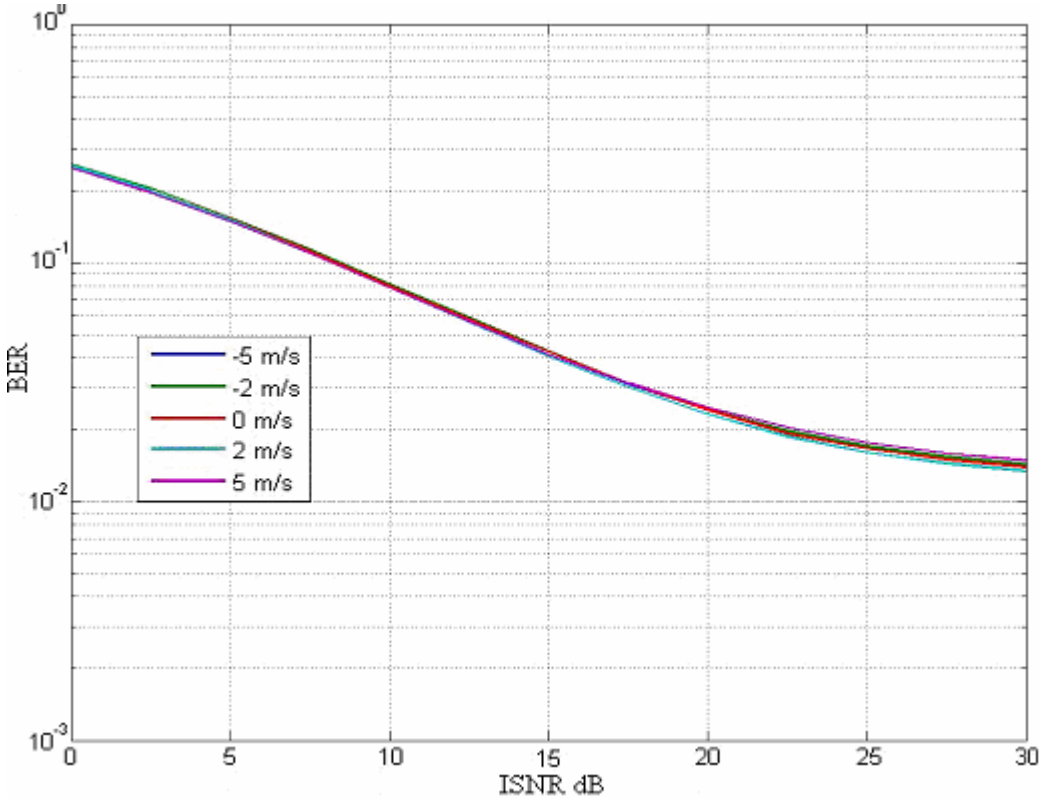

Figure 5.10**:** Single channel BER using QPSK at 1km transmission range

5.4 Conclusion

In this chapter, we combined the findings from the previous chapters to develop the structure of the signal frame as well as the receiver structure of the communications system. Due to small coherence bandwidth, short coherence time and long delay spread, the choice in number of OFDM sub-carriers and cyclic prefix length is limited.

The communications system was tested based on the assumption of a single receiver. Based on the similarity in BER performance at different velocities, we can conclude that the primary Doppler acquisition and compensation technique via LFM signals and linear interpolation can nullify most of the Doppler spread in the frequency spectrum of the signal.

ISI is dominant at short range transmission due to long delay spreads exceeding the length of cyclic prefix. Also, larger synchronization errors occur in simulation for short ranges. In reality, the energy of the first arrival path is usually higher than that of the reflected paths; thus smaller errors can be expected. The performance of the secondary Doppler compensation scheme using the OFDM cyclic prefix is affected by time-varying Rayleigh fading of individual paths, leading to ICI which inhibits further reduction in BER; In addition, the frequency of deep fades occurring increases as the transmission range reduces, causing a higher BER using DPSK when ISNR is low.

Therefore, we can conclude that the main challenges facing short range communications is an extensive delay spread and frequent deep fading; at medium to long ranges, low ISNR is the dominant factor affecting BER as fading occurs at a slower rate while delay spreads are shorter.

6. Channel Equalization Techniques

Diversity techniques are commonly applied to equalize channels in order to improve the performance of communications systems. Two such techniques are studied in this chapter: channel shortening and spatial beamforming.

6.1 Channel Shortening

Channel shortening equalizers are essentially time-domain filters that reduce the CIR to a desired length. Unlike adaptive filters, there is a greater degree of freedom in obtaining the filter weights since there is no restriction to reduce the CIR to a singular impulse response.

The UWA channel is generally characterized by a long and sparse CIR. Normally, such a sparse structure will be lost after filtering since an arbitrary power distribution results among the desired channel coefficients [22]. Multi-trellis Viterbi algorithms have been proposed to deal with such channels [21, 22], but tend to be computationally intensive due to the length of CIR associated with sparse channels. A blind method was proposed in [1] based upon minimization of the auto-correlation of the received signal. This method was further developed in [24-26] under the assumption of impulsive ambient noise. The possible drawback to the latter methods lies in the convergence time of the algorithm, although the method being blind seems suitable *a priori* in this context.

In this thesis, the 2 methods developed in [19] using the maximum shortening signal-to-noise ratio (MSSNR) and minimum mean square error (MMSE) as cost functions are tested for their suitability in shortening the UWA channel.

6.1.1 MSSNR and MMSE Techniques

Both the MSSNR and MMSE methods employed assume that the CIR is known, although application of the latter, as seen in [36], can also be within a blind context. When the CIR ***h(n)*** is known, let L_ω denote the length of the shortening filter $\boldsymbol{\omega}$, L_c the length of the target impulse response $\boldsymbol{c}$ and L_h the length of ***h(n)***. We define:

$$\mathbf{H}_{win}(\tau)=\begin{bmatrix} h(\tau) & h(\tau-1) & \cdots & h(\tau-L_\omega+1) \\ \vdots & & \ddots & \vdots \\ h(\tau+\upsilon) & h(d+\upsilon-1) & \cdots & h(\tau+\upsilon-L_\omega+1) \end{bmatrix} \tag{6.1}$$

$$\left.\begin{aligned} \mathbf{H}_1 &= \begin{bmatrix} h(0) & 0 & \cdots & 0 \\ h(1) & \ddots & & \vdots \\ \vdots & & \ddots & h(\tau-L_\omega-1) \\ h(\tau-1) & \cdots & h(\tau-L_\omega+1) & h(\tau-L_\omega) \end{bmatrix} \\ \mathbf{H}_2 &= \begin{bmatrix} h(\tau+\upsilon+1) & \cdots & h(\tau+\upsilon-L_\omega+2) \\ \vdots & \ddots & \vdots \\ h(L_h-1) & \ddots & h(L_h-L_\omega) \\ 0 & \ddots & h(L_h-L_\omega+1) \\ \vdots & \ddots & \vdots \\ 0 & \cdots & h(L_h-1) \end{bmatrix} \end{aligned}\right\} \mathbf{H}_{wall}(\tau)=\begin{bmatrix}\mathbf{H}_1 \\ \mathbf{H}_2\end{bmatrix} \tag{6.2}$$

$$\mathbf{H}=\begin{bmatrix}\mathbf{H}_1 \\ \mathbf{H}_{win} \\ \mathbf{H}_2\end{bmatrix} \quad \rightarrow \quad \mathbf{c}=\mathbf{H}\boldsymbol{\omega},\ \mathbf{c}_{win}=\mathbf{H}_{win}\boldsymbol{\omega},\ \mathbf{c}_{wall}=\mathbf{H}_{wall}\boldsymbol{\omega} \tag{6.3}$$

where υ+1 is the desired length of the target impulse response $\mathbf{c}_{\text{win}}$ and τ denotes the starting position of the target impulse response to be determined. Therein lies the disadvantage of channel shortening since the computational complexity of determining the optimal value of τ increases with L_c and L_h.

For MSSNR, the aim is to maximise the absolute square value of $\boldsymbol{c}_{win}$ subject to the constraint of making the absolute square value of $\boldsymbol{c}_{win}$ be equal to 1.

$$\max_{\boldsymbol{\omega}} \left\| \mathbf{c}_{win} \right\| = \max_{\boldsymbol{\omega}} \left\| \boldsymbol{\omega} \mathbf{H}_{win}^{T} \mathbf{H}_{win} \boldsymbol{\omega} \right\| \quad \text{subject to} \quad \left\| \mathbf{c}_{wall} \right\| = \boldsymbol{\omega} \mathbf{H}_{wall}^{T} \mathbf{H}_{wall} \boldsymbol{\omega} = 1 \tag{6.4}$$

$$\mathbf{H}_{win}^{T} \mathbf{H}_{win} \boldsymbol{\omega} = \lambda \mathbf{H}_{wall}^{T} \mathbf{H}_{wall} \boldsymbol{\omega} \tag{6.5}$$

Eq. (6.5) represents the generalized eigenvalue problem that needs to be solved to satisfy Eq. (6.4).

On the other hand, the MMSE method requires that the squared error between the desired response and the target impulse response to be minimum, subject to the constraint of making absolute square value of $\mathbf{c}_{\text{win}}$ be equal to 1 in order to prevent the trivial null solution. Thus, the eigenvalue problem is presented as:

$$\mathbf{H}_{win} \left(\mathbf{H}^{T} \mathbf{H} \right)^{-1} \mathbf{H}_{win}^{T} \mathbf{c}_{win} = \lambda \mathbf{c}_{win} \tag{6.6}$$

The computational complexity of searching throughout the valid range of τ for both the eigenvalue problems presented in Eqs. (6.5) and (6.6) can be minimised; the MSSNR method takes advantage of the symmetry of the square matrices while the MMSE method relies upon the computation of $\mathbf{R}(\tau) = \mathbf{I} - \mathbf{H}_{win} \left(\mathbf{H}^{T} \mathbf{H} \right)^{-1} \mathbf{H}_{win}^{T}$ to minimise the calculations for $\mathbf{R}(\tau+1)$ required to solve Eq. (6.6) [19].

6.1.2 Simulations

1 OFDM pilot and 3 OFDM data symbols modulated with DPSK at N = 256 and N_p = 64 is used as the test signal. No ambient noise and mobility is factored within the test for simplification. Instead, 3 channel types, defined as Type I, Type II and Type III generated with a maximum reflection of 2, 3 and 6, respectively, are used to test the channel shortening filters at different lengths. The CIR is known at the receiver and each arrival path is subjected to static, Rayleigh fading. The maximum CIR length is assumed to be 500 baseband OFDM samples, or 25ms as the signal bandwidth B_s = 20kHz. A total

of 1000 Monte Carlo trials are conducted to obtain the numerical results. Figure 6.1, Figure 6.2 and Figure 6.3 illustrates the typical channel profile of channel Type I to III.

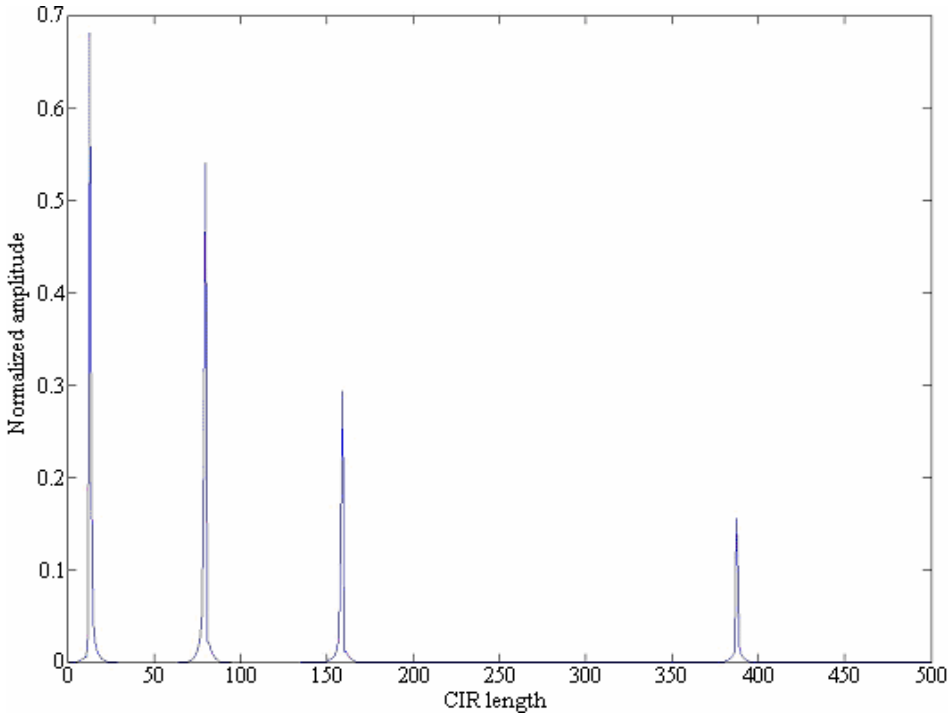

Figure 6.1**:** Typical profile of CIR for channel Type I

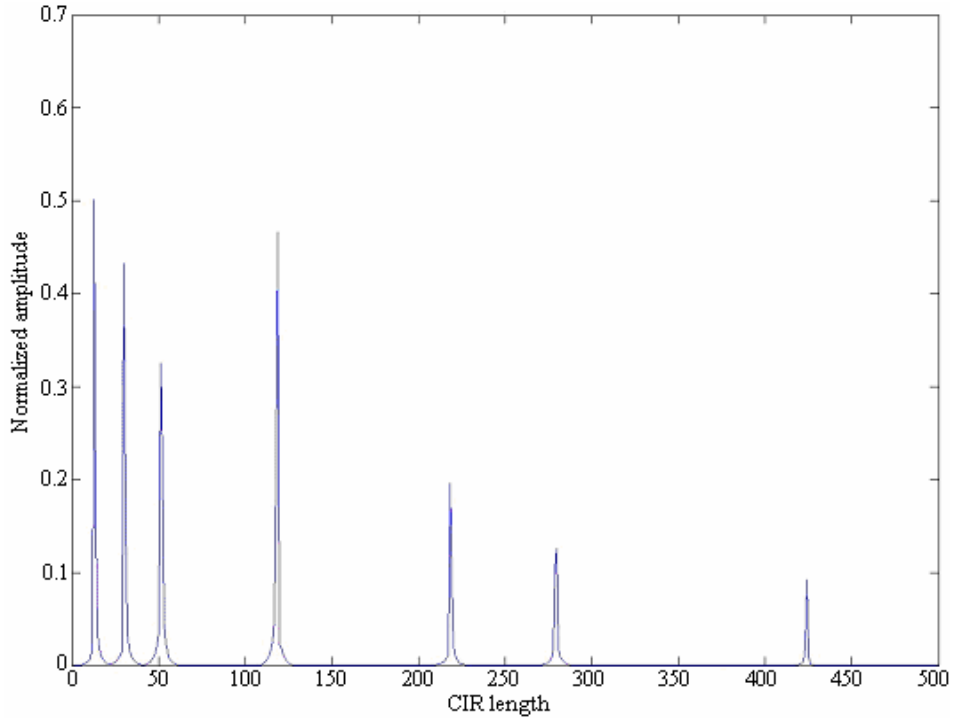

Figure 6.2**:** Typical profile of CIR for channel Type II

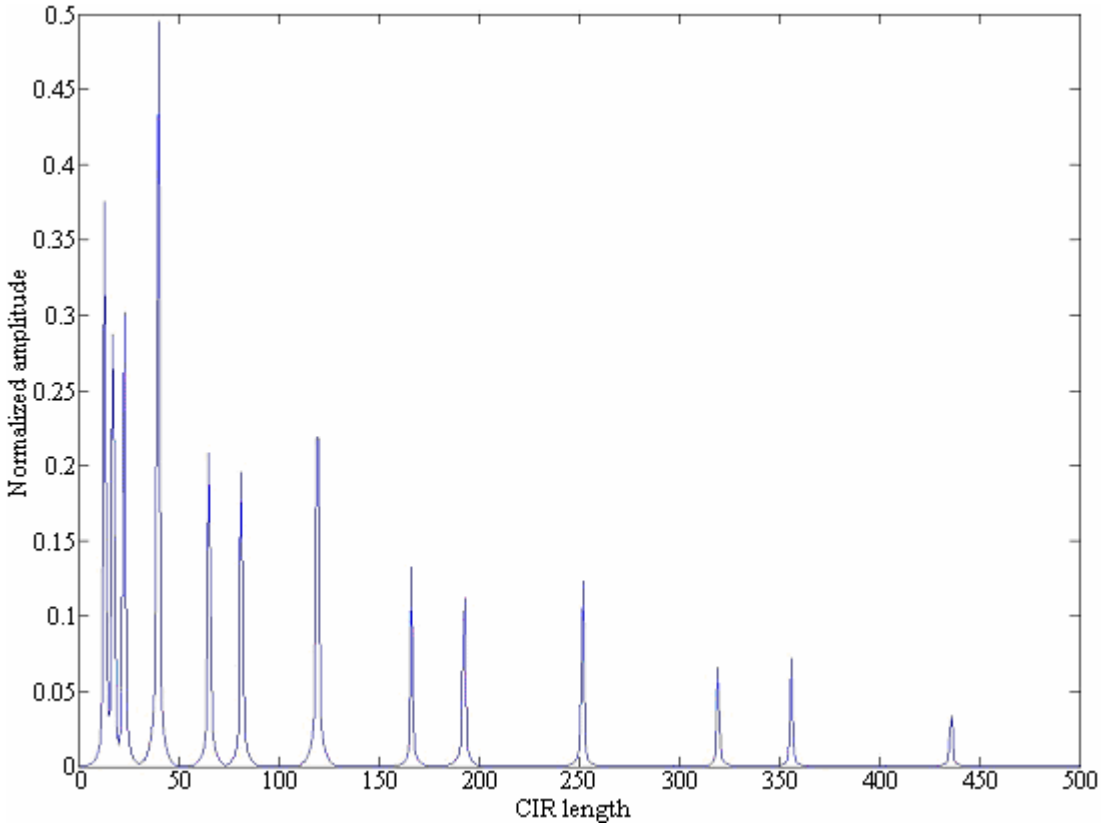

Figure 6.3**:** Typical profile of CIR for channel Type III

Two parameters are used as a measure of performance for channel shortening: signal-to-interference ratio (SIR) and BER. For SIR, the impulse response within the desired duration is taken as the useful signal energy while any remaining impulse response outside the window is considered to be interference. Hence, the window of useful energy is taken to be N_p = 64 from the optimal delay τ found using both methods.

From Figures 6.4 to 6.6, we observe that the MSSNR method is able to improve the SIR with increasing number of taps for all three channel types. The MMSE SIR performance deteriorates as the number of maximum reflections increase. More often than not, the SIR is not able to surpass that of the original channel. While the trend for the MSSNR method is increasing SIR with increasing number of taps, the performance of the MMSE method is indifferent to increasing filter taps.

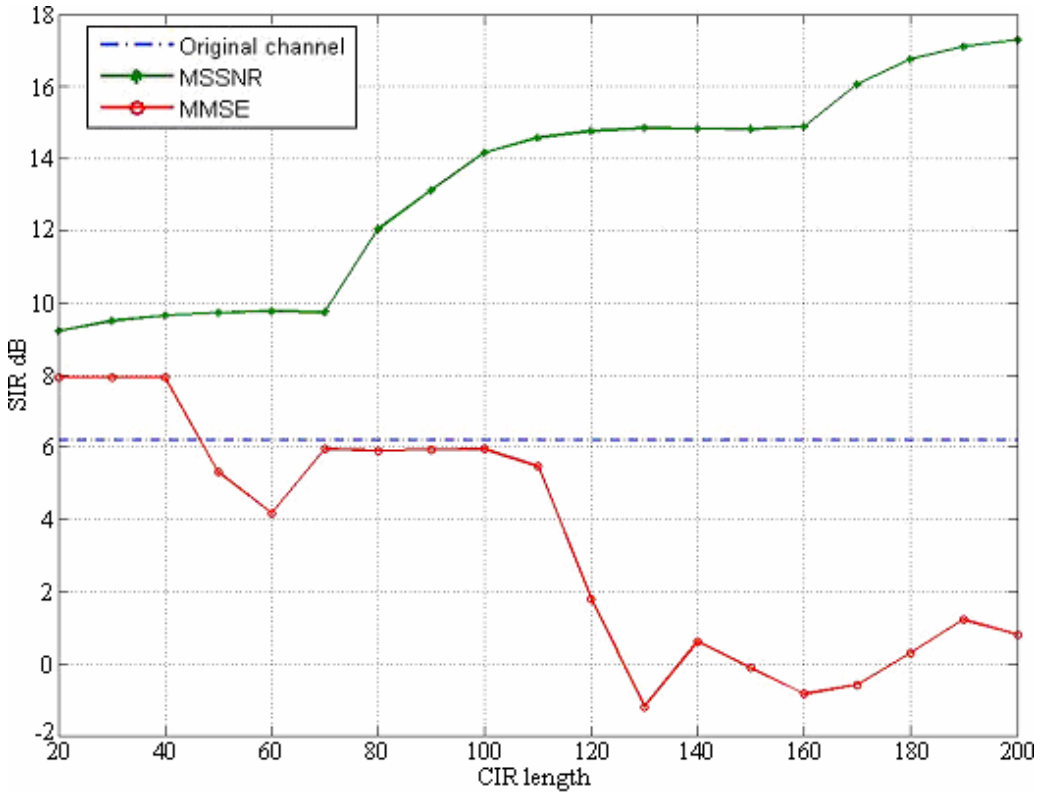

Figure 6.4**:** SIR of original channel, MSSNR and MMSE for channel Type I

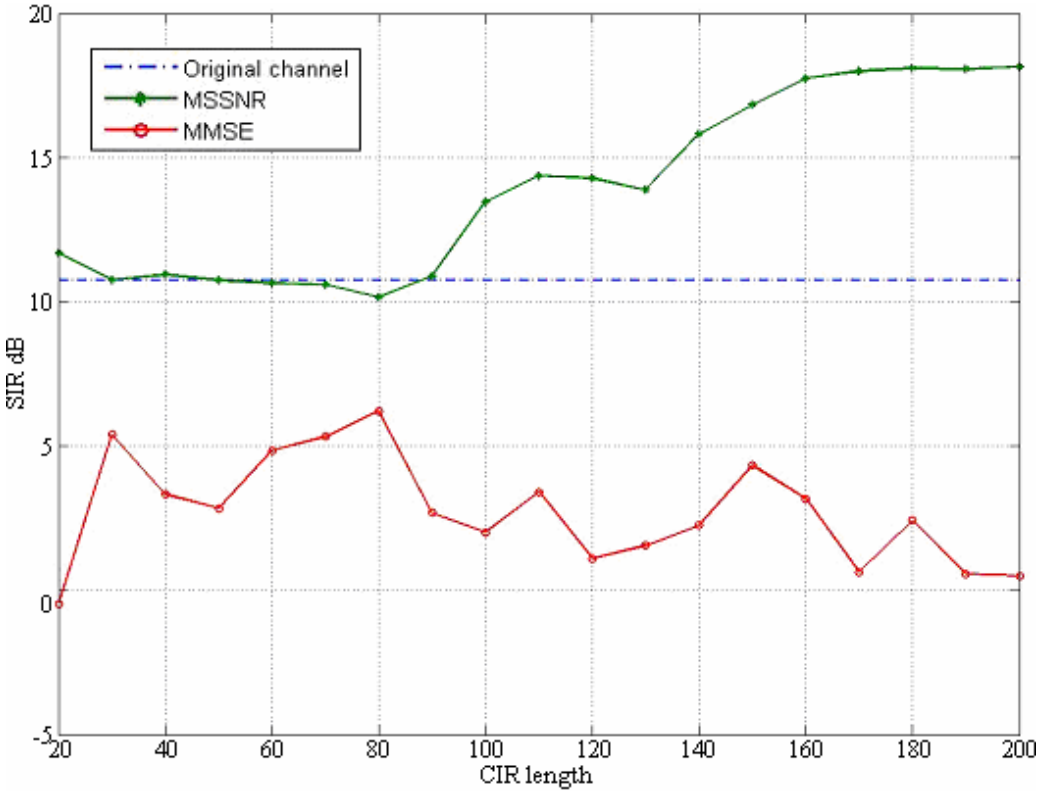

Figure 6.5**:** SIR of original channel, MSSNR and MMSE for channel Type II

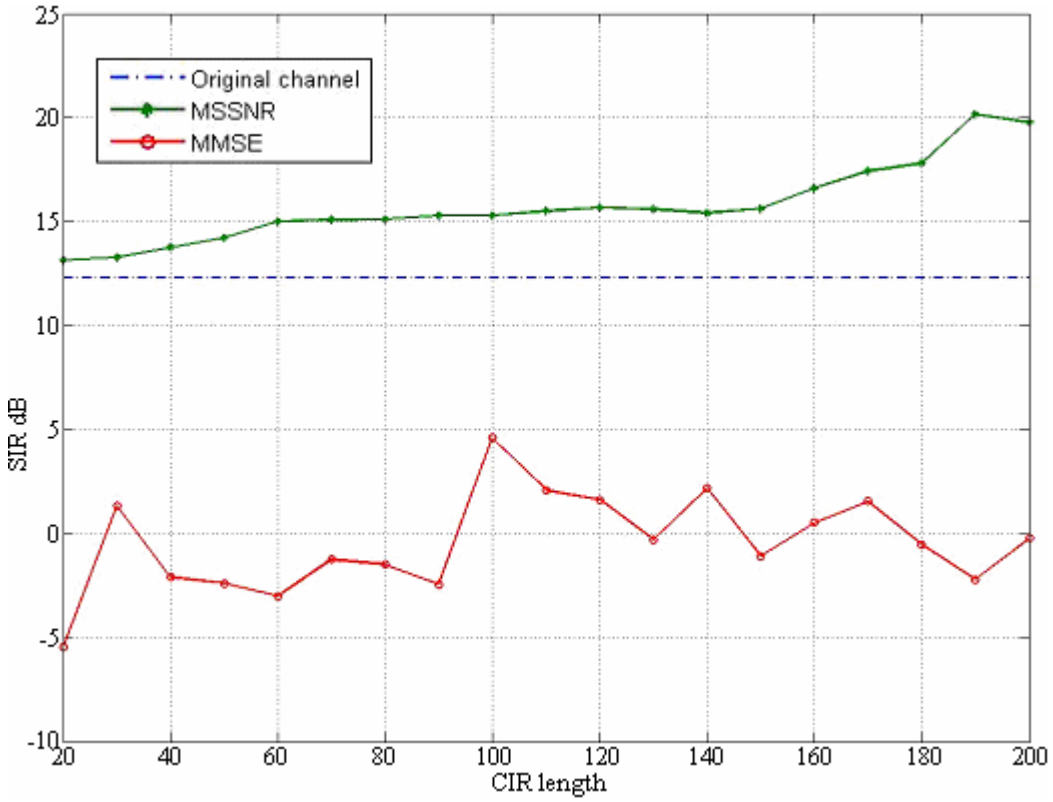

Figure 6.6**:** SIR of original channel, MSSNR and MMSE for channel Type III

Figure 6.7 shows that the MMSE is able to deliver a lower BER for channel Type I using 60 to 80 channel shortening filter taps. Figures 6.8 and 6.9 show the BER performance for channel Type II and III, respectively. Although the SIR for MSSNR is superior to that of the original channel and the MMSE method, the BER obtained is inferior in most instances to that resulting from the unfiltered signal. As for the MMSE method, the resulting BER is constantly higher for all the number of filter taps tested. Thus, even though channel shortening may be considered successful using MSSNR with respect to the improvement in SIR, it is ultimately the BER which determines the performance of the communications system. As such, the implementation of channel shortening methods using MSSNR and MMSE should be avoided in UWA communications.

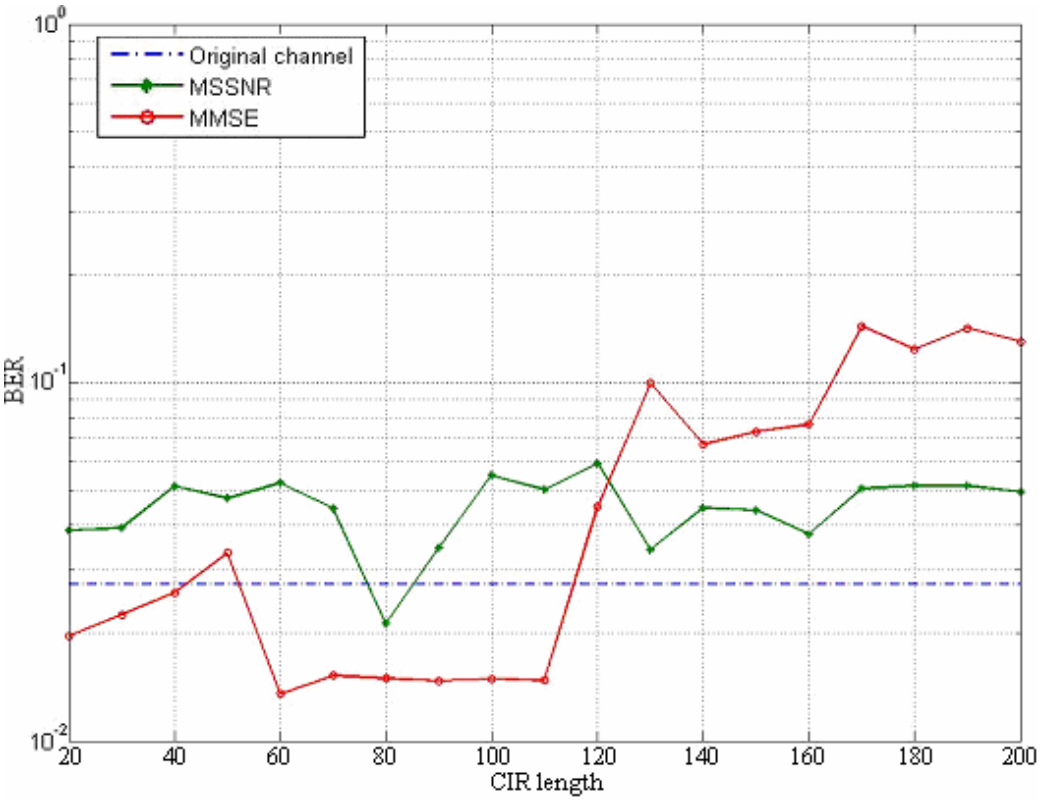

Figure 6.7**:** BER of original channel, MSSNR and MMSE for channel Type I

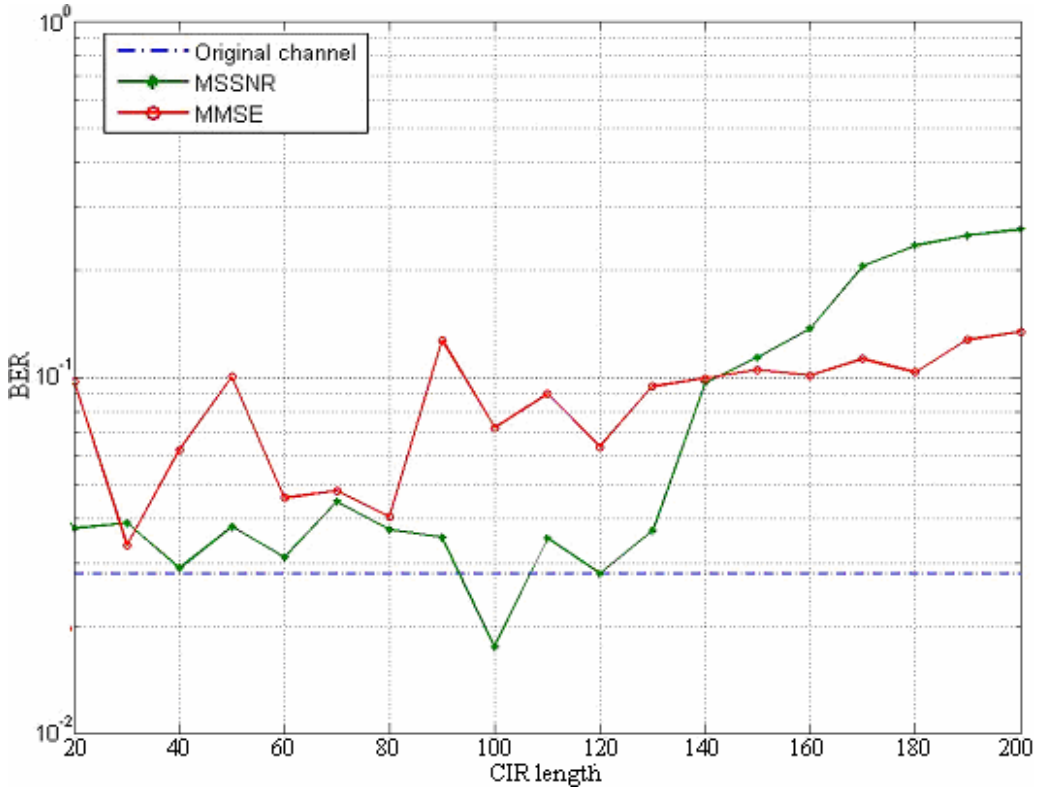

Figure 6.8**:** BER of original channel, MSSNR and MMSE for channel Type II

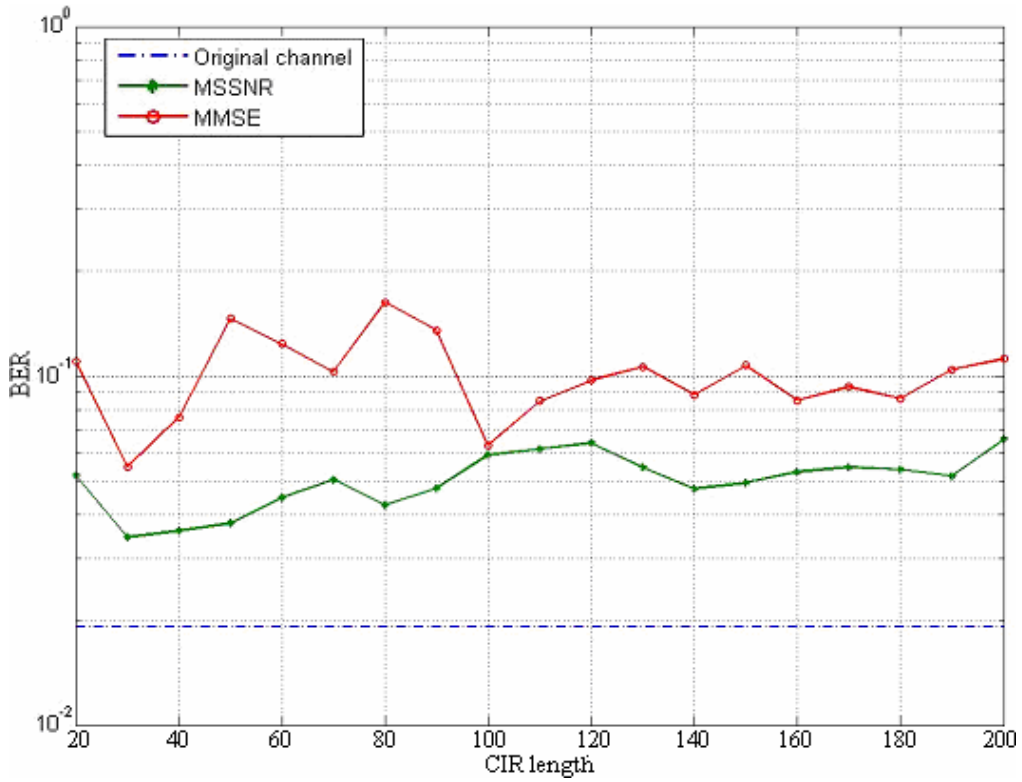

Figure 6.9**:** BER of original channel, MSSNR and MMSE for channel Type III

6.2 Multi-channel Techniques

Spatial diversity takes advantage of multiple receivers to deduce the angle of arrival of the desired signal and create a directivity pattern to suppress unwanted signals within the bandwidth of interest arriving from other directions. For short range transmission, the DOA is quite separated between arrivals; at medium to long ranges, the DOA for all the paths will be quite narrow, hence beamforming would be less effective in suppressing multi-path arrivals. However, it can suppress noise sources that are arriving from a different DOA, resulting in higher overall ISNR. In this thesis, we assume that the multi-path arrivals are limited to two-dimensions in space since we do not expect a high volume of underwater traffic or objects which will contribute to laterally reflected paths. Also, it is assumed that the added impulsive noise to each receiver is independent.

6.2.1 Blind, Least Square Spatial Equalization

Unconstrained spatial equalizers adhere to the principle of power inversion, whereby the weakest signal at the array input is enhanced at the array output of the equalizer [13]. In this case, the weakest arrival path is chosen and in the absence of multi-path arrival, the signal inevitably gets suppressed altogether. For constrained spatial equalizer, the DOA must first be deduced by aligning the incoming signal at each receiver to the desired arrival path.

Assume that there are Q receivers and that the incoming signal vector at each receiver $\mathbf{r}_q(n)$ is of length L_r, $\forall q \in [1,Q]$. The desired signal is assumed to be unknown at the receiver, hence a blind method. We assume without any loss of generality that $\mathbf{r}_q(n)$ are all aligned to the first path arrival. Let $\mathbf{R}(n) = [\mathbf{r}_1(n) \ \ldots \ \mathbf{r}_Q(n)]$; if $\mathbf{r}_q(n)$ comprises only of the transmitted signal $s(n)$ and ambient noise, then:

$$\begin{aligned}
&\mathbf{r}_q(n) = \mathbf{s}(n) + \mathbf{v}_q(n) \\
&\mathbf{R}(n) = \left[\mathbf{r}_1(n) \quad \cdots \quad \mathbf{r}_Q(n)\right] \\
&\mathbf{M} = \mathbf{R}^H\mathbf{R} = \underbrace{\begin{bmatrix} \mathbf{s}^H\mathbf{s} & \cdots & \mathbf{s}^H\mathbf{s} \\ \vdots & \ddots & \vdots \\ \mathbf{s}^H\mathbf{s} & \cdots & \mathbf{s}^H\mathbf{s} \end{bmatrix}}_{Q} + \begin{bmatrix} \mathbf{v}_1^H\mathbf{v}_1 & \cdots & \mathbf{v}_1^H\mathbf{v}_Q \\ \vdots & \ddots & \vdots \\ \mathbf{v}_Q^H\mathbf{v}_1 & \cdots & \mathbf{v}_Q^H\mathbf{v}_Q \end{bmatrix} + 2\,\mathrm{Re}\left(\begin{bmatrix} \mathbf{s}^H\mathbf{v}_1 & \cdots & \mathbf{s}^H\mathbf{v}_Q \\ \vdots & \ddots & \vdots \\ \mathbf{s}^H\mathbf{s} & \cdots & \mathbf{s}^H\mathbf{v}_Q \end{bmatrix}\right) \\
&E(\mathbf{M}) = E\left(\underbrace{\begin{bmatrix} \mathbf{s}^H\mathbf{s} & \cdots & \mathbf{s}^H\mathbf{s} \\ \vdots & \ddots & \vdots \\ \mathbf{s}^H\mathbf{s} & \cdots & \mathbf{s}^H\mathbf{s} \end{bmatrix}}_{Q}\right) + E\left(\begin{bmatrix} \mathbf{v}_1^H\mathbf{v}_1 & 0 & \cdots & 0 \\ 0 & \ddots & & \vdots \\ \vdots & & \ddots & 0 \\ 0 & \cdots & 0 & \mathbf{v}_Q^H\mathbf{v}_Q \end{bmatrix}\right)
\end{aligned} \tag{6.7}$$

Should the noise energy be negligible compared to the signal energy, then the matrix $\mathbf{M}$ can be considered to be ill-conditioned or singular in the absence of noise [12]. In a multi-path channel, $E(\mathbf{M})$ is normally an invertible, symmetric matrix.

Let **w** represent the tap-weight vector and **y***(n)* the equalized vector output:

$$\begin{aligned} &\mathbf{y}(n) = \mathbf{R}(n)\mathbf{w} \\ &\mathbf{c}^T\mathbf{w} = 1 \\ &\mathbf{c} = \underbrace{[1 \quad \cdots \quad 1]}_{Q}^T \end{aligned} \tag{6.8}$$

The weights are constrained such that the total sum yields 1 to prevent a trivial null solution. To render the algorithm adaptive, the weights are updated as follows [13]:

$$\begin{aligned} &1. \quad \mathbf{M} = \mathbf{P}^H \mathbf{\Lambda} \mathbf{P}, \quad \mathbf{\Lambda} = diag\begin{pmatrix} \lambda_1 & \cdots & \lambda_Q \end{pmatrix} \\ &2. \quad \hat{\varepsilon}_{beam} = \frac{\max(\lambda_q)}{\min(\lambda_q)}, \; q \in [1, Q] \\ &3. \quad \mathbf{M}_{inv} = \begin{cases} \mathbf{M}^{-1} & if \; \hat{\varepsilon}_{beam} < \varepsilon_{beam} \\ \mathbf{I}_Q & otherwise \end{cases} \\ &4. \quad \mathbf{w} = (1-\lambda)\mathbf{w} + \frac{\lambda \mathbf{M}_{inv}\mathbf{c}}{\mathbf{c}^T\mathbf{M}_{inv}\mathbf{c}} \end{aligned} \tag{6.9}$$

When the condition number $\hat{\varepsilon}_{beam}$ exceeds the stipulated threshold ε_{beam}, the matrix is considered to be ill-conditioned. In this situation, the tap weights are updated to move towards an omni-directional, overall unit gain. The forgetting factor λ is imposed to minimise variations due to noise.

6.2.2 Multi-channel Signal Detection and Doppler Acquisition

Having multiple channels allows for the LFM signal detection and primary Doppler acquisition to be refined. Signal detection and Doppler acquisition remains the same for each individual channel. Thereafter, the estimated starting point of the LFM signals which is closest to the mean starting point is taken as the valid start points. Channels which have both starting points within a window ε_{sym} of the valid start points are considered to be good estimates. Likewise, the mean Doppler estimate is obtained from

the channels that detected the LFM signals. If at least one channel is valid from the symbol timing estimation and the mean error in Doppler estimate is within a determined Doppler threshold ε_{dop}, then the overall detection and acquisition scheme is considered successful.

6.2.3 Simulation

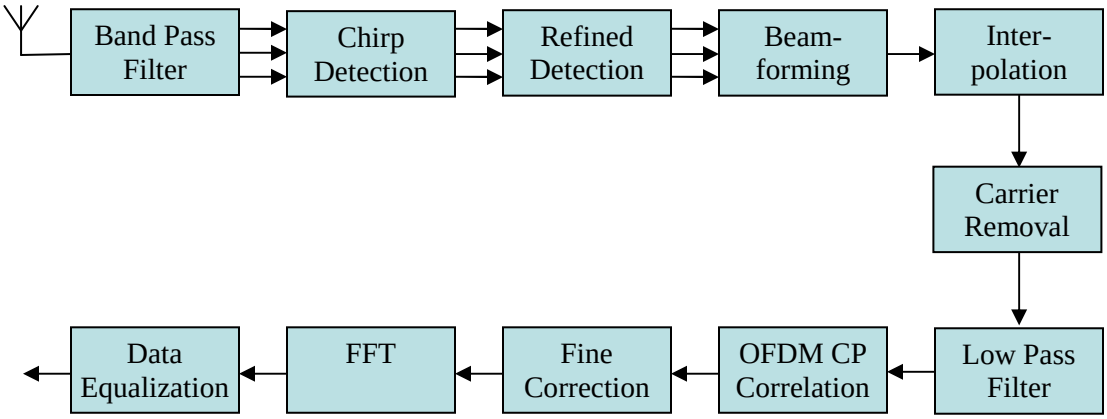

Figure 6.10**:** Schematic of multi-channel receiver structure

The signal and channel parameters used are identical to that of the single channel simulation conducted in Chapter 5, except 5 receivers are used. The beamforming parameters are L_r = 160 baseband OFDM samples (corresponds to 8ms signal duration), ε_{beam} = 60 and λ = 0.005; update is conducted once every 0.4ms. For the refined detection, ε_{sym} = 2 baseband OFDM samples and ε_{dop} = 0.0002. Two other similar signal structures were included in the simulations. The first structure have all the 3 OFDM pilot symbols arranged at the start of the OFDM signal block; the second consists of 48 OFDM symbols at N = 128 and N_p = 32 of which 6 are OFDM pilot symbols. The latter is effectively having half the number of OFDM sub-carriers and twice the number of OFDM symbols as compared to the former structure. Effective bandwidth remains at 27,015 bps.

Table 6.1: Multi-channel detection, synchronization and Doppler estimate at 50m.

Velocity	Number of successful detections at different ISNR (dB)						
m/s	0	5	10	15	20	25	30
-5.0	1725	1946	1994	2000	2000	2000	2000
-2.0	1798	1955	1997	1997	2000	2000	2000
0	1788	1961	1995	2000	2000	2000	2000
2.0	1823	1974	1998	2000	2000	2000	2000
5.0	1746	1947	1991	2000	2000	2000	2000
Velocity	Symbol timing RMS error at different ISNR (dB)						
m/s	0	5	10	15	20	25	30
-5.0	8.45	2.71	2.14	1.52	1.52	1.52	1.17
-2.0	11.10	7.37	5.76	4.08	3.99	3.98	3.97
0	6.31	3.42	2.67	2.67	2.66	2.45	2.44
2.0	6.52	4.67	4.85	4.51	4.80	4.81	4.80
5.0	7.44	5.63	3.66	3.92	3.92	3.91	3.91
Velocity	Doppler MSE $\varepsilon = \left(\Delta - \hat{\Delta}_1\right)^2$ at different ISNR (dB)						
m/s	0	5	10	15	20	25	30
-5.0	$1.27*10^{-8}$	$5.55*10^{-9}$	$3.97*10^{-9}$	$3.85*10^{-9}$	$3.74*10^{-9}$	$3.81*10^{-9}$	$3.84*10^{-9}$
-2.0	$1.99*10^{-8}$	$8.31*10^{-9}$	$3.63*10^{-9}$	$3.21*10^{-9}$	$3.27*10^{-9}$	$3.46*10^{-9}$	$3.57*10^{-9}$
0	$1.03*10^{-8}$	$3.84*10^{-9}$	$1.08*10^{-9}$	$2.76*10^{-10}$	$6.25*10^{-11}$	0	0
2.0	$1.72*10^{-8}$	$5.81*10^{-9}$	$2.60*10^{-9}$	$1.90*10^{-9}$	$1.98*10^{-9}$	$2.13*10^{-9}$	$2.18*10^{-9}$
5.0	$4.92*10^{-8}$	$6.93*10^{-9}$	$2.87*10^{-9}$	$2.15*10^{-9}$	$1.74*10^{-9}$	$1.75*10^{-9}$	$1.75*10^{-9}$
Velocity	Doppler MSE $\varepsilon = \left(\Delta - \hat{\Delta}_1 - \hat{\Delta}_2\right)^2$ at different ISNR (dB)						
m/s	0	5	10	15	20	25	30
-5.0	$4.01*10^{-9}$	$4.12*10^{-10}$	$1.27*10^{-11}$	$1.24*10^{-11}$	$1.23*10^{-11}$	$1.22*10^{-11}$	$1.22*10^{-11}$
-2.0	$7.93*10^{-9}$	$1.88*10^{-9}$	$2.54*10^{-11}$	$2.08*10^{-11}$	$1.84*10^{-11}$	$1.72*10^{-11}$	$1.67*10^{-11}$
0	$2.94*10^{-9}$	$8.46*10^{-11}$	$1.29*10^{-11}$	$8.13*10^{-12}$	$5.92*10^{-12}$	$4.96*10^{-12}$	$4.55*10^{-12}$
2.0	$2.66*10^{-9}$	$3.32*10^{-11}$	$1.79*10^{-11}$	$1.24*10^{-11}$	$9.44*10^{-12}$	$7.68*10^{-12}$	$6.83*10^{-12}$
5.0	$4.51*10^{-9}$	$3.98*10^{-9}$	$1.49*10^{-11}$	$1.40*10^{-11}$	$1.36*10^{-11}$	$1.33*10^{-11}$	$1.32*10^{-11}$

Table 6.2: Multi-channel detection, synchronization and Doppler estimate at 200m.

Velocity	Number of successful detections at different ISNR (dB)						
m/s	0	5	10	15	20	25	30
-5.0	1672	1907	1988	1998	2000	2000	2000
-2.0	1719	1932	1989	2000	2000	2000	2000
0	1722	1931	1991	1997	2000	2000	2000
2.0	1749	1940	1995	2000	2000	2000	2000
5.0	1645	1907	1985	2000	2000	2000	2000
Velocity	Symbol timing RMS error at different ISNR (dB)						
m/s	0	5	10	15	20	25	30
-5.0	7.23	2.19	0.42	0.41	0.41	0.41	0.41
-2.0	7.22	1.61	0.40	0.39	0.38	0.39	0.39
0	8.27	2.54	0.41	0.42	0.42	0.44	0.43
2.0	6.17	1.71	0.57	0.57	0.57	0.56	0.56
5.0	5.50	1.35	0.44	0.45	0.45	0.45	0.45
Velocity	Doppler MSE $\varepsilon = \left(\Delta - \hat{\Delta}_1\right)^2$ at different ISNR (dB)						
m/s	0	5	10	15	20	25	30
-5.0	$4.05*10^{-8}$	$6.17*10^{-9}$	$4.41*10^{-9}$	$3.73*10^{-9}$	$3.73*10^{-9}$	$3.83*10^{-9}$	$3.86*10^{-9}$
-2.0	$2.32*10^{-8}$	$7.62*10^{-9}$	$3.66*10^{-9}$	$2.99*10^{-9}$	$3.25*10^{-9}$	$3.41*10^{-9}$	$3.43*10^{-9}$
0	$1.22*10^{-8}$	$3.73*10^{-9}$	$2.11*10^{-9}$	$3.15*10^{-10}$	0	0	0
2.0	$1.90*10^{-8}$	$7.73*10^{-9}$	$3.65*10^{-9}$	$2.00*10^{-9}$	$1.91*10^{-9}$	$2.08*10^{-9}$	$2.09*10^{-9}$
5.0	$1.44*10^{-8}$	$6.04*10^{-9}$	$2.69*10^{-9}$	$2.13*10^{-9}$	$1.75*10^{-9}$	$1.75*10^{-9}$	$1.75*10^{-9}$
Velocity	Doppler MSE $\varepsilon = \left(\Delta - \hat{\Delta}_1 - \hat{\Delta}_2\right)^2$ at different ISNR (dB)						
m/s	0	5	10	15	20	25	30
-5.0	$3.15*10^{-8}$	$1.17*10^{-10}$	$1.07*10^{-11}$	$1.04*10^{-11}$	$1.03*10^{-11}$	$1.02*10^{-11}$	$1.02*10^{-11}$
-2.0	$8.92*10^{-9}$	$3.91*10^{-9}$	$1.40*10^{-11}$	$1.12*10^{-11}$	$1.11*10^{-11}$	$1.10*10^{-11}$	$1.11*10^{-11}$
0	$6.57*10^{-9}$	$1.94*10^{-9}$	$1.89*10^{-11}$	$3.40*10^{-12}$	$2.83*10^{-12}$	$2.71*10^{-12}$	$2.69*10^{-12}$
2.0	$2.75*10^{-9}$	$2.37*10^{-9}$	$8.96*10^{-12}$	$6.06*10^{-12}$	$5.35*10^{-12}$	$5.19*10^{-12}$	$5.13*10^{-12}$
5.0	$1.16*10^{-8}$	$2.12*10^{-9}$	$1.39*10^{-11}$	$1.35*10^{-11}$	$1.35*10^{-11}$	$1.35*10^{-11}$	$1.35*10^{-11}$

Table 6.3: Multi-channel detection, synchronization and Doppler estimate at 1km.

Velocity	Number of successful detections at different ISNR (dB)						
m/s	0	5	10	15	20	25	30
-5.0	1635	1907	1982	1998	2000	2000	2000
-2.0	1672	1929	1995	2000	2000	2000	2000
0	1735	1946	1989	2000	2000	2000	2000
2.0	1687	1943	1994	2000	2000	2000	2000
5.0	1675	1917	1992	1998	1998	2000	2000
Velocity	Symbol timing RMS error at different ISNR (dB)						
m/s	0	5	10	15	20	25	30
-5.0	7.69	2.09	0.64	0.66	0.66	0.67	0.67
-2.0	6.48	2.07	0.61	0.59	0.58	0.58	0.58
0	6.23	1.59	0.93	0.76	0.78	0.78	0.79
2.0	6.44	2.02	0.60	0.61	0.63	0.63	0.61
5.0	5.45	1.39	0.74	0.74	0.75	0.75	0.75
Velocity	Doppler MSE $\varepsilon = \left(\Delta - \hat{\Delta}_1\right)^2$ at different ISNR (dB)						
m/s	0	5	10	15	20	25	30
-5.0	$1.57*10^{-8}$	$7.64*10^{-9}$	$4.37*10^{-9}$	$4.24*10^{-9}$	$4.08*10^{-9}$	$3.97*10^{-9}$	$4.00*10^{-9}$
-2.0	$2.15*10^{-8}$	$9.77*10^{-9}$	$4.73*10^{-9}$	$4.13*10^{-9}$	$4.39*10^{-9}$	$4.69*10^{-9}$	$4.83*10^{-9}$
0	$1.31*10^{-8}$	$5.31*10^{-9}$	$1.67*10^{-9}$	$3.82*10^{-10}$	$8.87*10^{-11}$	0	0
2.0	$2.11*10^{-8}$	$9.84*10^{-9}$	$4.10*10^{-9}$	$3.34*10^{-9}$	$4.09*10^{-9}$	$4.58*10^{-9}$	$4.79*10^{-9}$
5.0	$7.99*10^{-8}$	$5.61*10^{-9}$	$3.16*10^{-9}$	$2.00*10^{-9}$	$1.78*10^{-9}$	$1.75*10^{-9}$	$1.75*10^{-9}$
Velocity	Doppler MSE $\varepsilon = \left(\Delta - \hat{\Delta}_1 - \hat{\Delta}_2\right)^2$ at different ISNR (dB)						
m/s	0	5	10	15	20	25	30
-5.0	$9.38*10^{-9}$	$4.17*10^{-9}$	$8.30*10^{-11}$	$7.85*10^{-11}$	$7.65*10^{-11}$	$7.61*10^{-11}$	$7.59*10^{-11}$
-2.0	$2.35*10^{-9}$	$4.06*10^{-9}$	$2.37*10^{-11}$	$2.39*10^{-11}$	$2.50*10^{-11}$	$2.60*10^{-11}$	$2.64*10^{-11}$
0	$2.22*10^{-9}$	$2.04*10^{-9}$	$8.91*10^{-12}$	$5.68*10^{-12}$	$5.12*10^{-12}$	$4.85*10^{-12}$	$4.82*10^{-12}$
2.0	$4.65*10^{-9}$	$5.92*10^{-9}$	$1.16*10^{-11}$	$7.71*10^{-12}$	$7.05*10^{-12}$	$6.72*10^{-12}$	$6.54*10^{-12}$
5.0	$7.10*10^{-9}$	$2.15*10^{-9}$	$1.57*10^{-11}$	$1.54*10^{-11}$	$1.53*10^{-11}$	$1.53*10^{-11}$	$1.53*10^{-11}$

Tables 6.1 to 6.3 show the results of detection rate, symbol timing error and Doppler estimate error for transmission range of 50m, 200m and 1km, respectively. Smaller symbol timing errors were observed from 200m onwards. Once again, the accuracy of the secondary Doppler acquisition reaches a threshold from 15dB onwards.

Figures 6.11 to 6.16 show the BER performance with multi-channel diversity for both DPSK and QPSK data modulation scheme at various transmission ranges. At 50m, the multi-channel BER performance for both QPSK and DPSK were similar. DPSK outperformed QPSK for the other transmission ranges. At 1km, the BER for both QPSK and DPSK converged towards that of the single channel results. The most likely causes for this threshold are fading as well as the limited accuracy of Doppler compensation after 15dB. Overall, multi-channel combining was able to yield lower BER.

Figures 6.17 to 6.19 compares the different QPSK based data modulation scheme using multi-channel combining at various transmission ranges. The performance obtained from using 128 OFDM sub-carriers and a cyclic prefix of 32 samples is similar to that obtained from $N = 256$ and $N_p = 64$. Also, having the OFDM pilot symbols grouped at the start only yielded very slight gains in BER before reaching a threshold at 50m; however, at 200m, clear performance gain is seen for ISNR less than 15dB for the 256 OFDM sub-carrier signals. The signal using $N = 128$ runs almost parallel at a higher BER to the $N = 256$ counterpart due to ISI as path suppression is less effective at medium ranges. At 1km, the signals with 256 OFDM sub-carriers showed no difference in BER performance. The 128 sub-carrier system yielded a higher BER as ISNR increased. This agrees with the theory in [5] that DPSK is more suitable in impulsive ambient noise.

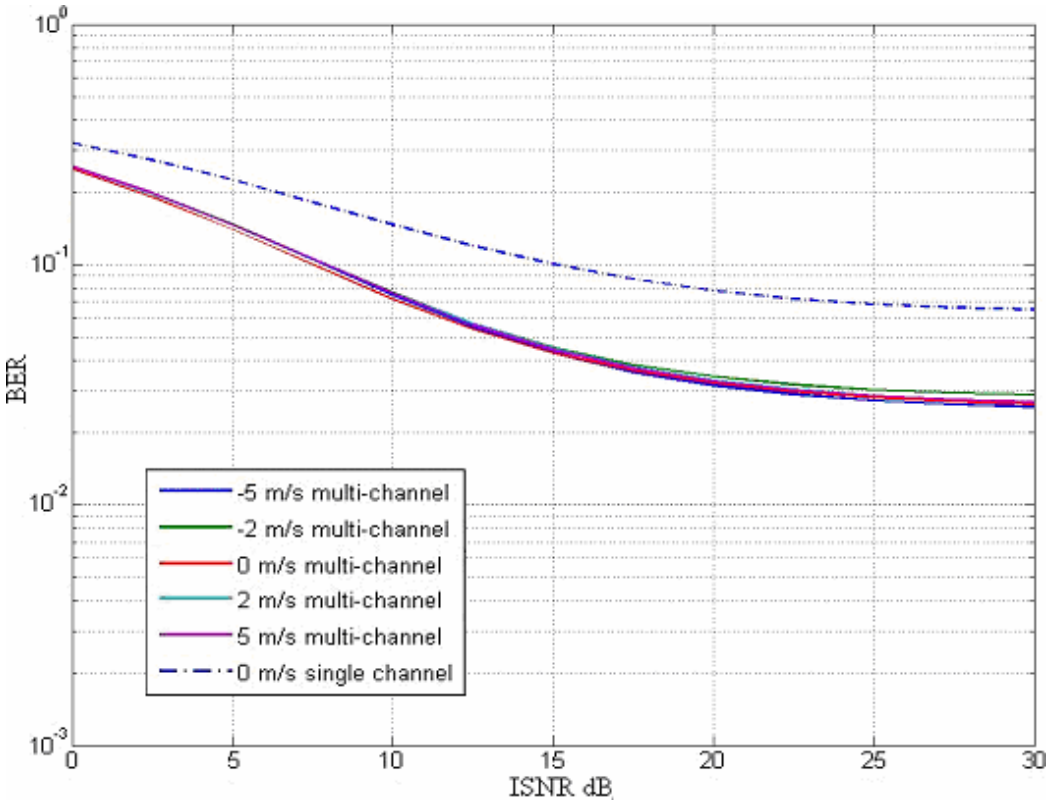

Figure 6.11**:** Multi-channel BER using DPSK at 50m transmission range

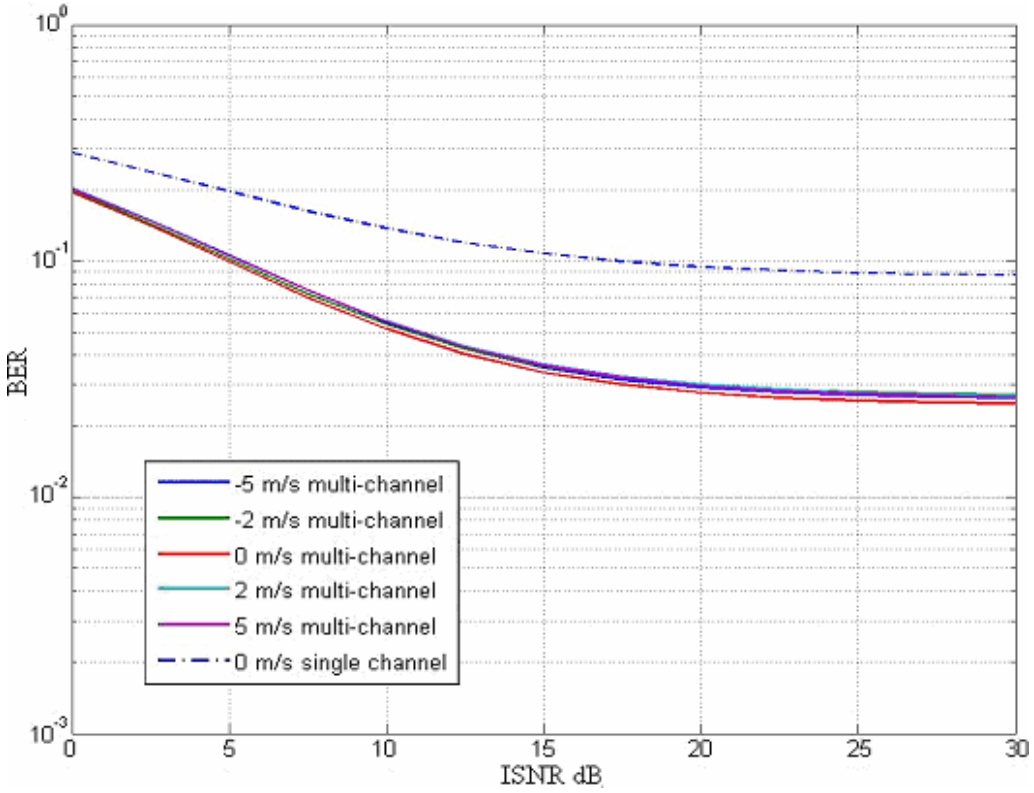

Figure 6.12**:** Multi-channel BER using QPSK at 50m transmission range

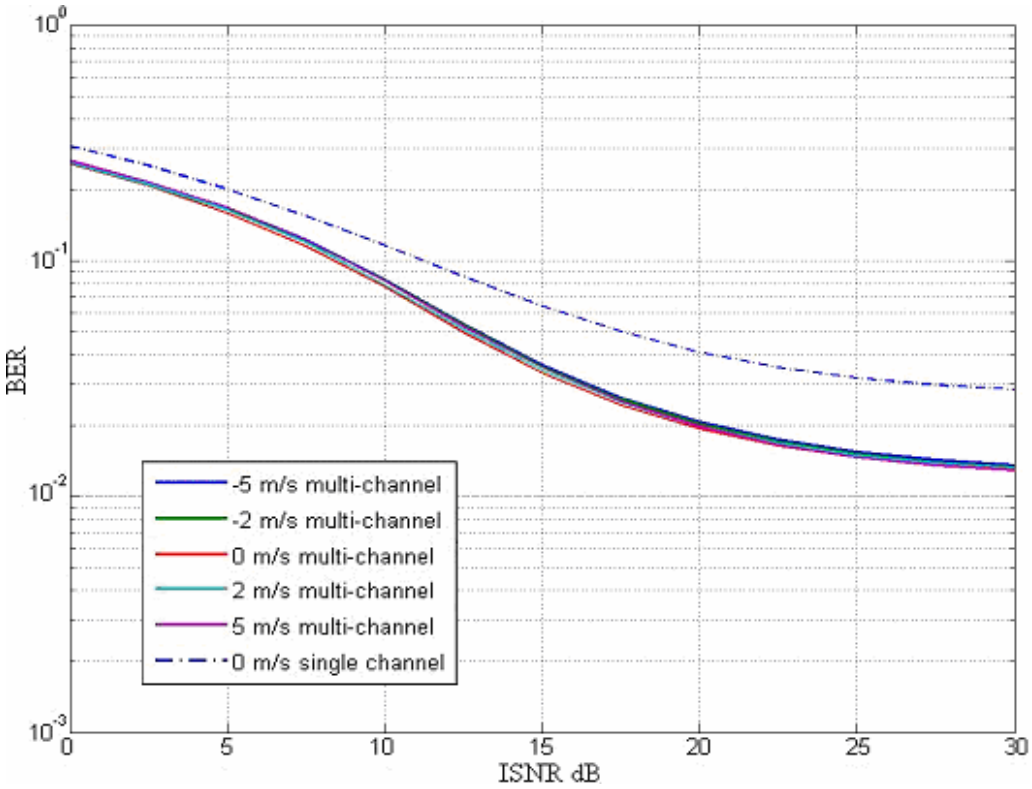

Figure 6.13**:** Multi-channel BER using DPSK at 200m transmission range

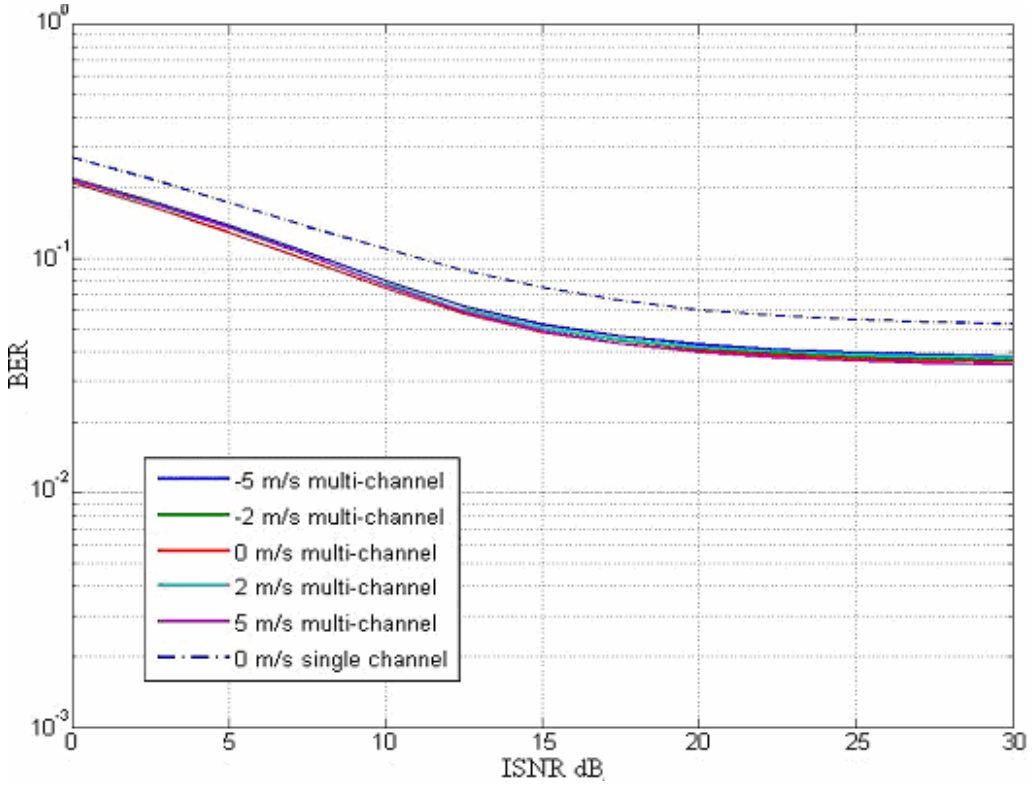

Figure 6.14**:** Multi-channel BER using QPSK at 200m transmission range

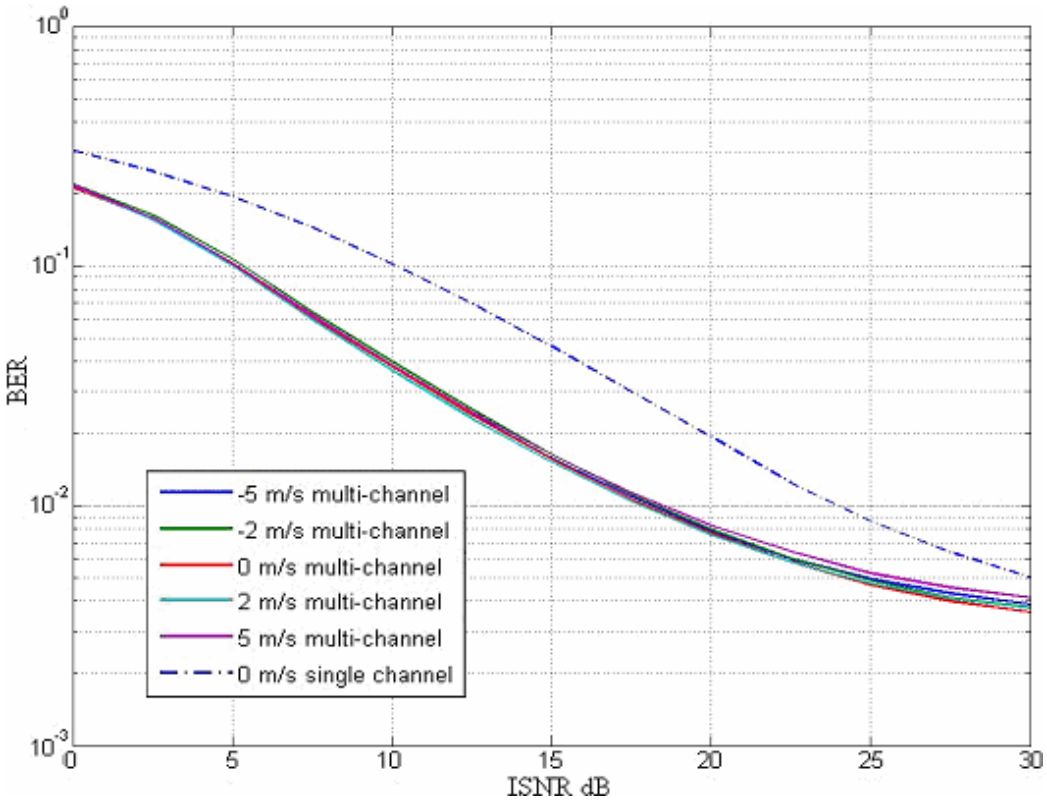

Figure 6.15**:** Multi-channel BER using DPSK at 1km transmission range

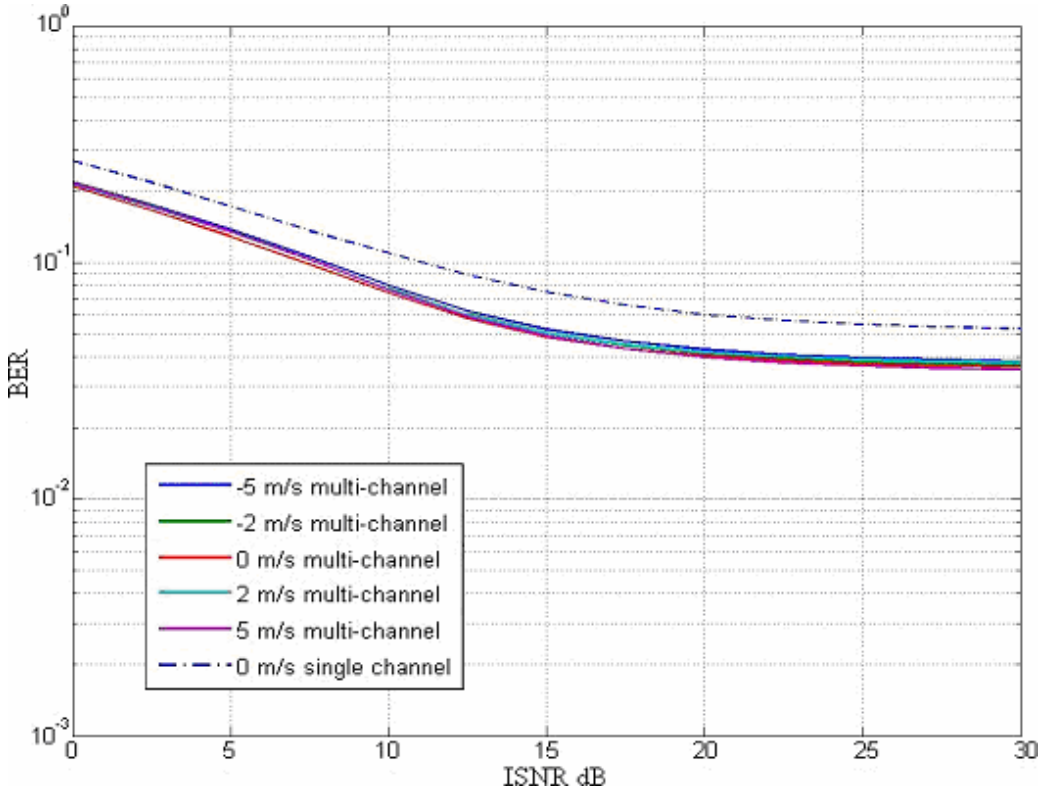

Figure 6.16**:** Multi-channel BER using QPSK at 1km transmission range

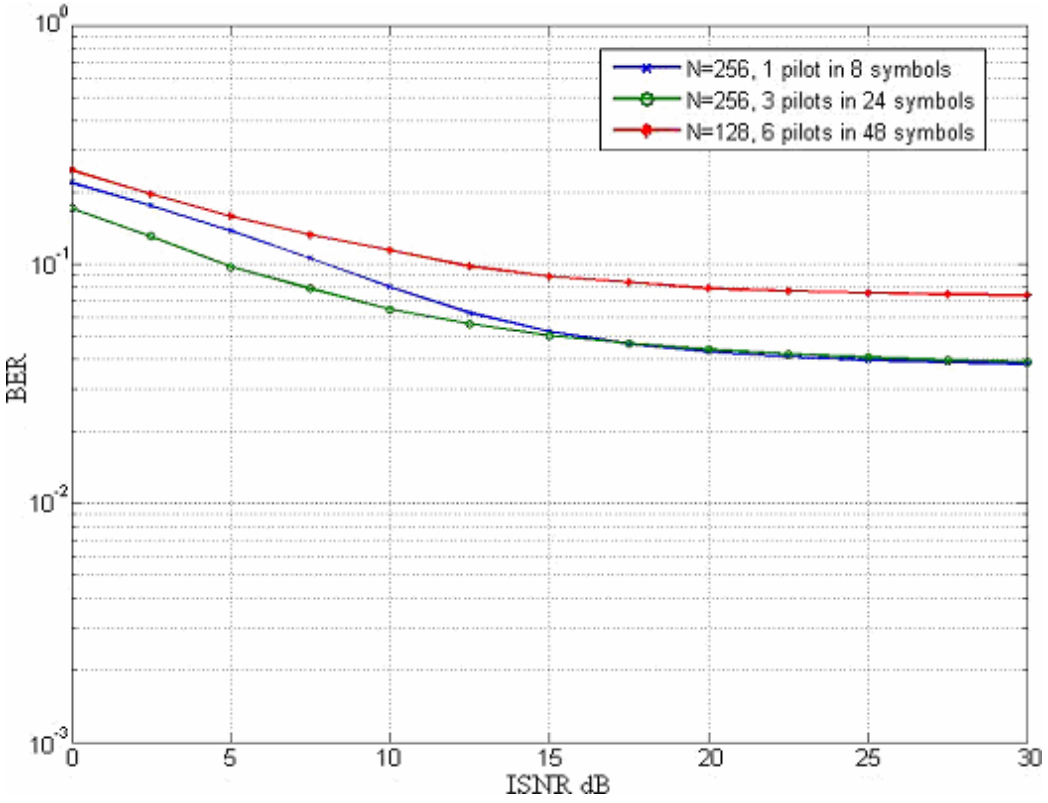

Figure 6.17**:** Multi-channel BER using QPSK at 50m range and 0m/s velocity

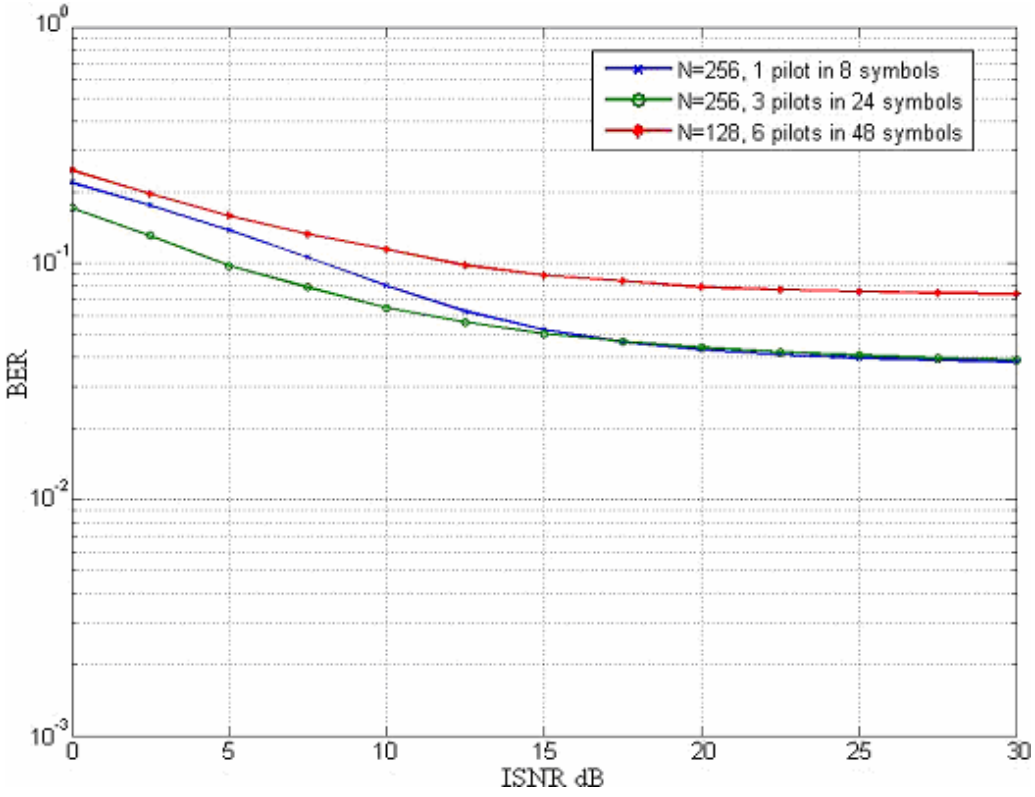

Figure 6.18**:** Multi-channel BER using QPSK at 200m range and 0m/s velocity

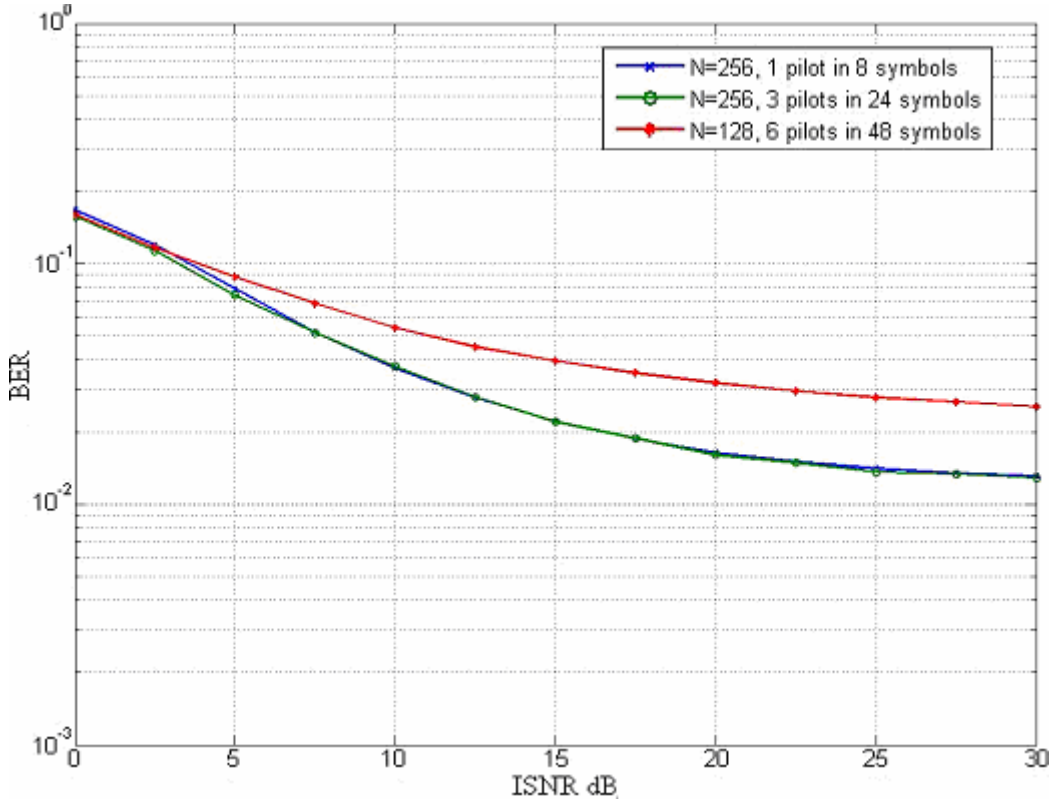

Figure 6.19**:** Multi-channel BER using QPSK at 1km range and 0m/s velocity

6.2.4 Further Investigations

In order to understand the exact reason why BER reaches a threshold, further tests are conducted using a shorter signal frame. Instead of having 3 segments of OFDM symbols consisting of 1 pilot and 7 data symbols, only 1 segment is used instead. A comparison of the BER for the 3 different scenarios will enable us to identify the dominant factor resulting in irreducible BER at high ISNR: 1) perfect symbol timing and Doppler compensation 2) perfect symbol timing only 3) estimated symbol timing and Doppler compensation.

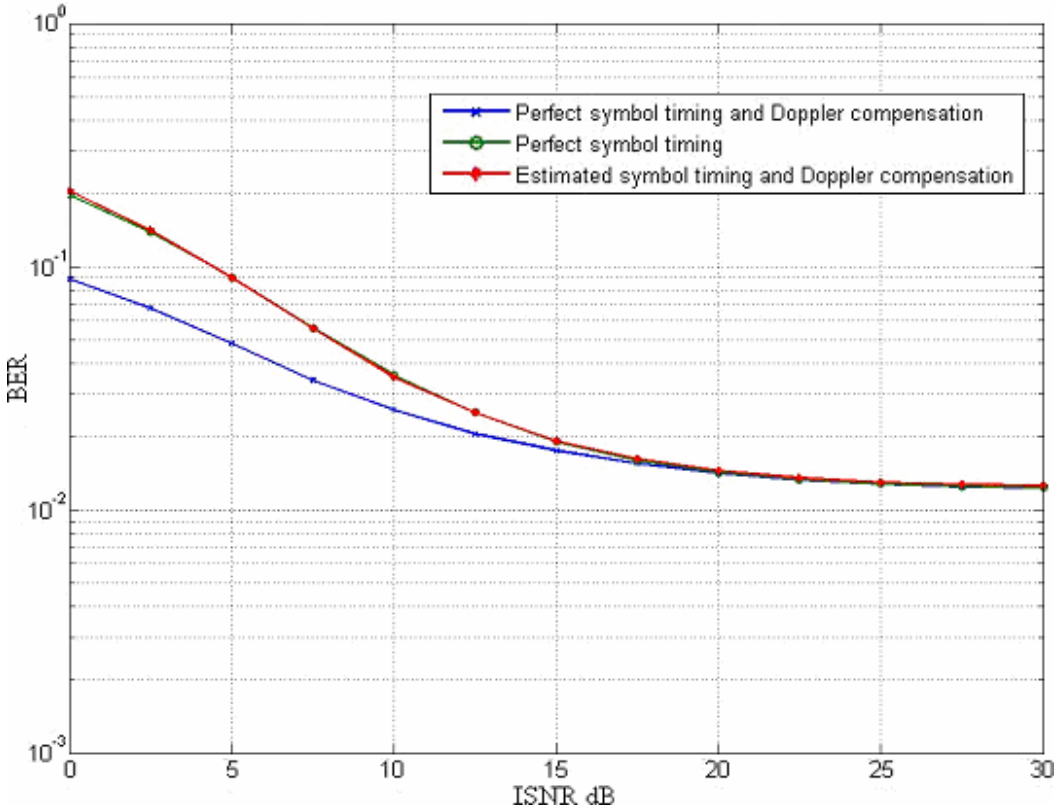

Figure 6.20**:** Multi-channel BER using DPSK at 50m range and 0m/s velocity

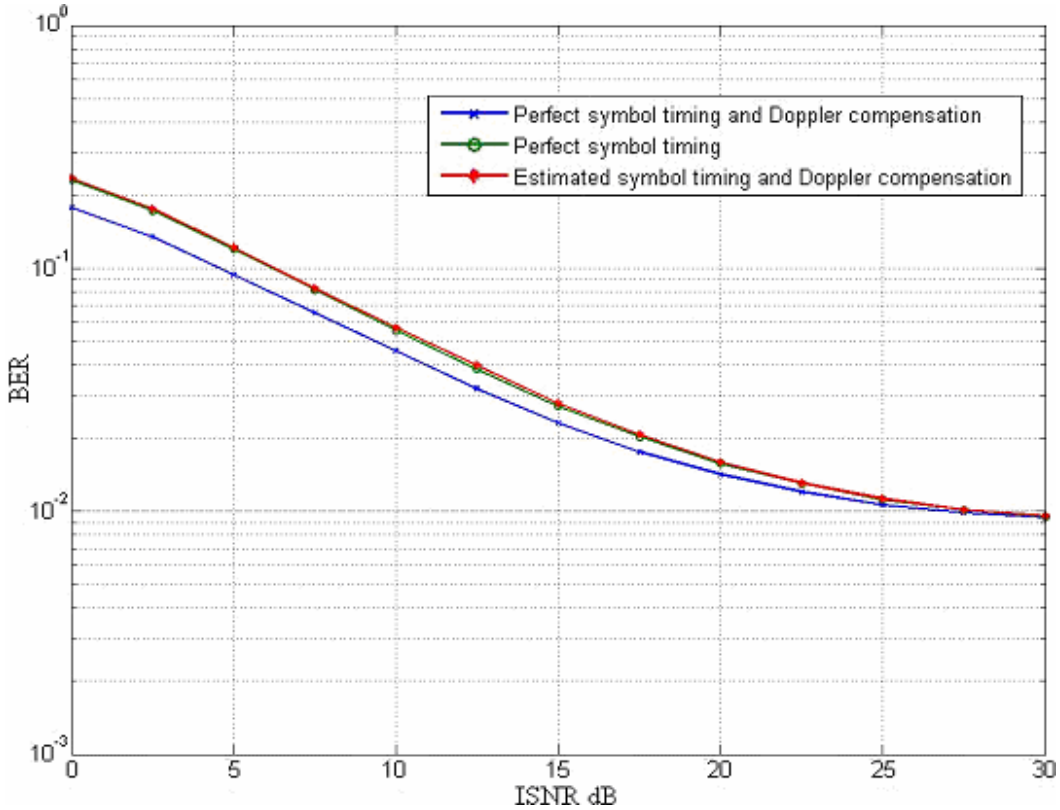

Figure 6.21**:** Multi-channel BER using DPSK at 200m range and 0m/s velocity

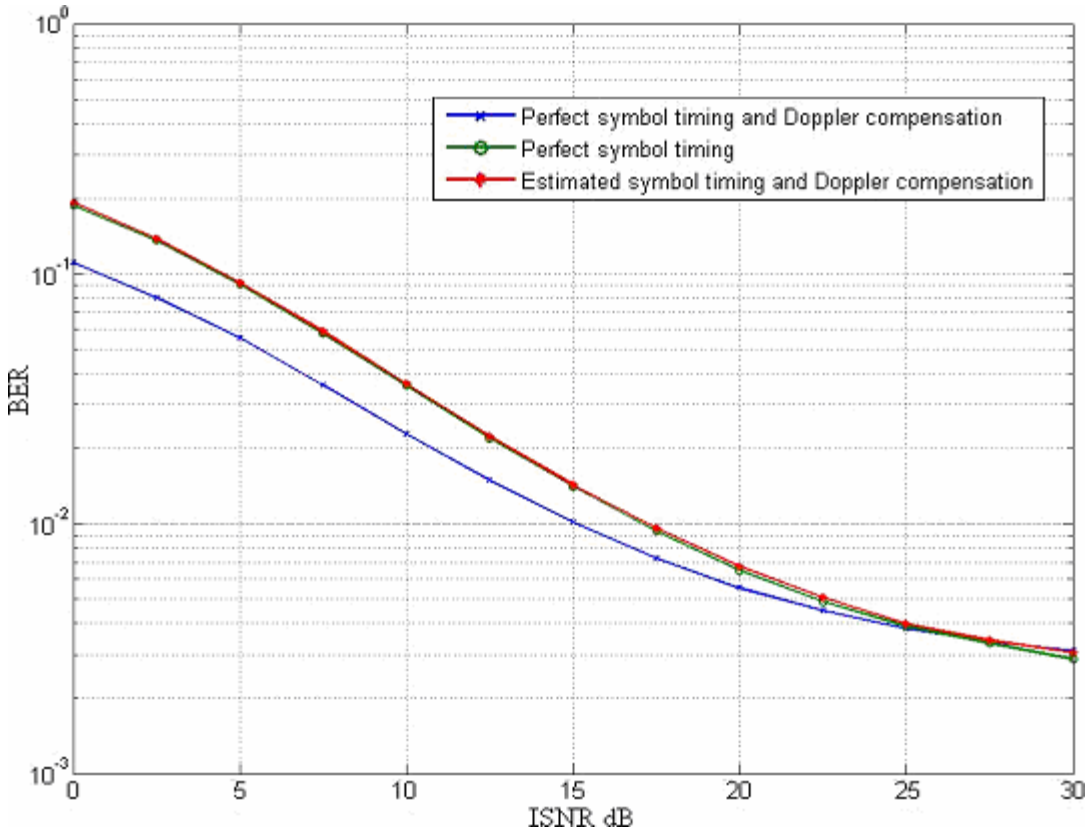

Figure 6.22**:** Multi-channel BER using DPSK at 1km range and 0m/s velocity

From Figures 6.20 to 6.22, it is observed that the BER in all 3 scenarios saturated at the same level for all the transmission ranges tested. The penalty incurred from errors in symbol timing is considerably negligible. On the other hand, Doppler estimation errors result in higher BER at low ISNR. As ISNR increases, this error gap decreases as the dominant influence in BER arises from time-varying channel conditions. From Chapter 2, we deduced that the channel coherence time tends to be shorter as transmission range decreases resulting in fast fading. This is evident from the 3 figures, as BER at 30dB is higher at 50m and decreases further at 200m and 1km, respectively. Therefore, an improvement in the Doppler estimation would be ineffective as the performance is bounded by the fading statistics of the channel.

6.3 Conclusion

In this chapter, a study of two equalizations technique was made. Simulations conducted with channel shortening techniques gave inconclusive evidence that such a method would be able to minimise ISI and hence improve BER. Although channel shortening via Viterbi algorithm were shown in [21] and [22] to be suitable for sparse channels, they were not tested in this thesis due to the computational complexity involved.

Spatial diversity techniques proved to be a robust equalization method at the cost of increased number of receivers and computational complexity. A blind, least squares, equalization technique was used and proved to be most effective at short range transmission where DOA is easily separable. At medium to long ranges, the advantage it poses is an improvement in ISNR since DOA is narrow. By employing DPSK, a reduction of 50% in BER can be expected at all ranges compared to using a single channel. Nevertheless, BER remains in the order of 10^{-2} in the uncoded channel at a transfer speed of 27 kbps.

Errors in estimation of the Doppler scaling factor leads to higher BER at low ISNR, but this effect becomes negligible compared to the penalty imposed by channel fading statistics at high ISNR, resulting in irreducible BER. Symbol timing errors were found to have less effect on the BER performance.

7. Thesis Conclusion and Further Research

7.1 Conclusion

This thesis incorporated the study of the warm shallow UWA channel to develop a strategy for mobile communications underwater. Due to relatively lower propagation speeds in water, Doppler effects are not limited to Doppler shift, but also Doppler spreading of the signal frequency spectrum. We have shown that a failure to compensate for the latter results in poor performance of an OFDM based communications system even at modest speeds.

Doppler compensation technique involves a two-prong attack upon the challenge posed by mobility – interpolation and carrier frequency offset compensation. Due to difficulties in detecting OFDM signals without involving numerous match filters, LFM signals are used instead for detection and primary Doppler acquisition as they are insensitive to mobility-induced time scaling. Secondary Doppler acquisition relies on the simple method of OFDM cyclic prefix correlation. Interpolation is performed after both instances with an additional CFO compensation required after secondary acquisition. Based upon numerical results, the compensation scheme has proven to be effective at velocities of up to 5m/s.

Symbol timing synchronization is shown to be more erroneous at short ranges due to increased fading, delay and Doppler spreads. OFDM cyclic prefix based methods of obtaining symbol timing may be accurate between OFDM symbols, however a start timing as close to the first path of arrival as possible is desired to minimise ISI, especially

when delay spread may exceed the length of the cyclic prefix used. Channel estimation based on the LFM signal is able to reduce the error in estimating the starting point of the signal based on simulations. Effectively, timing synchronization are expected to perform better in sea trials as fading conditions are less severe.

Simulation results show that by using an uncoded, single channel for OFDM based communications with 256 sub-carriers and DPSK modulation, we can expect a BER of 10^{-2} at an effective transfer speed of 27kbps for communication ranges up to 1km. By combining multiple channels, BER is expected to stay within the same order but lower than that obtained using a single channel.

Deeper investigation revealed that the performance of OFDM based communications in shallow UWA channel is limited by time-varying fading statistics at higher ISNR. Due to the dynamism of the channel, frequency selective fading as well as deep amplitude fades causes numerous errors upon demodulation. At low ISNR, Doppler estimation error penalises the BER performance. Nevertheless, we believe that the simulated channel poses a harsher condition upon fading statistics compared to the real channel; hence, BER is postulated to be lower in sea trials.

7.2 Further Research

In many real applications of signal communications, channel coding and interleaving have shown improvements in BER albeit at lower bandwidth efficiency and higher computational cost. Introducing turbo codes into the system developed here would create a more robust communications scheme when implemented for sea trials. In addition, multiple input multiple output systems takes advantage of space-time diversity to improve data rate, thus it is a potential candidate for further exploration.

The multi-channel system in this thesis assumes a two-dimensional space with independent noise at each receiver. In reality, the ambient noise source as well as the signal source is three-dimensional. Some of the noise would then be correlated and the receiver structure will have to be modified to take this into account. The received signal should be mostly two-dimensional, barring horizontal scattering of the signal source. Thus, impulsive noise may be further reduced from the unwanted space but become more correlated in the DOA of the signal. More data is required to develop a model for simulating ambient noise detected using multiple transducers.

Bibliography

[1] J. Balakrishnan, R. K. Martin, and C. R. Johnson, Jr., "Blind, Adaptive Channel Shortening by Sum-squared Auto-correlation Minimization (SAM)," *IEEE Trans. on Signal Processing*, December 2003.

[2] J. Bingham, "Multicarrier Modulation for Data Transmission: An Idea Whose Time Has Come," *IEEE Trans. Commun.*, vol. 28, no. 5, pp. 5--14, May 1990.

[3] L. M. Brekhovskikh and Y. Lysanov, *Fundamentals of Ocean Acoustics (2nd edition)*. Germany: Springer-Verlag, 1991.

[4] J. A. Catipovic, "Performance Limitations in Underwater Acoustic Telemetry," *IEEE J. Oceanic Eng.*, vol. 15, no. 3, pp. 205-216, 1990.

[5] M. Chitre, "Underwater Acoustic Communications in Warm Shallow Water Channels," P.hD. Thesis, Singapore: National University of Singapore, 2006.

[6] M. Chitre, J. Potter and S. H. Ong, "Underwater Acoustic Channel Characterization for Medium-range Shallow Water Communications," in *Proceedings of MTS/IEEE TECHNO-OCEANS '04*, pp. 40-45, 2004.

[7] D Daly, C Heneghan, and A D Fagan, "A Minimum Mean-Squared Error Interpretation of Residual ISI Channel Shortening for Discrete Multitone Transceivers," *ICASSP 2001*, vol. 4, pp. 2065-2068, May 2001.

[8] G. F. Edelmann, T. Akal, W. S. Hodgkiss, S. Kim, W. A. Kuperman, and H. C. Song, "An Initial Demonstration of Underwater Acoustic Communication Using Time Reversal," *IEEE J. Oceanic Eng.*, vol. 27, pp. 602-609, 2002.

[9] L. Erup, F. M. Gardner, and R. A. Harris, "Interpolation in Digital Modems – Part II: Implementation and Performance," in *IEEE Transactions On Communications*, vol. 41 no. 6, pp. 998-1008, June 1993.

[10 Freitag, L., M. Johnson and M. Stojanovic, "Integrated Doppler Tracking and Interpolation for Phase-Coherent Acoustic Communication," *IEEE Journal of Oceanic Engineering*, January 2002.

[11] F. M. Gardner, "Interpolation in Digital Modems – Part I: Fundamentals," in *IEEE Transactions On Communications*, vol. 41 no. 3, pp. 501-507, March 1993.

[12] G. H. Golub, C. F. Van Loan, *Matrix Computations*, Baltimore: Johns Hopkins University Press , 1983.

[13] S. Haykin, *Adaptive Filter Theory*, 4th ed. New Jersey: Prentice Hall, 2002.

[14] D. B. Kilfoyle and A. B. Baggeroer, "The State of the Art in Underwater Acoustic Telemetry," *IEEE J. Oceanic Eng.*, vol. 25, no. 1, pp. 4-27, 2000.

[15] B-C. Kim, I-T. Lu, "Parameter Study of OFDM Underwater Communications System," in *Conference and Exhibition of MTS/IEEE OCEANS '00*, vol. 2, pp. 1251-1255, September 2000.

[16] W. A. Kuperman, W. S. Hodgkiss, H. C. Song, T. Akal, C. Ferla, and D. R. Jackson, "Phase Conjugation in the Ocean: Experimental Demonstration of a Time Reversal Mirror," *J. Acoust. Soc. Am.*, vol. 103, pp. 25-40, 1998.

[17] E. Lawrey, "The Suitability of OFDM as a Modulation Technique for Wireless Telecommunications, with a CDMA Comparison." James Cook University, 1997.

[18] Z.-B. Lin, "Wideband ambiguity function of broadband signals, " *J. Acoust. Soc. Amer.*, vol. 83, no. 6, June 1988.

[19] R. K. Martin, M. Ding, B. L. Evans, and C. R. Johnson Jr., "Efficient Channel Shortening Equalizer Design," *EURASIP Journal on Applied Signal Processing*, vol. 2003, no. 13, pp. 1279-1290, December 2003.

[20] P. J. W. Melsa, R. C. Younce, and E**.** Rohrs, "Impulsive Response Shortening for Discrete Multitone Transceivers," *IEEE Transactions on Communications*, vol. 44 no. 12**,** pp. 1662-1672, December 1996.

[21] J. Mietzner, S. Badri-Hoeher, and P. A. Hoeher, "Prefiltering and trellis-based equalization for sparse ISI channels, " *Proc. 14th IST Mobile & Wireless Commun. Summit*, Dresden, Germany, June 2005.

[22] J. Mietzner, S. Badri-Hoeher, I. Land and P. A. Hoeher, "Equalization of Sparse Intersymbol-Interference Channels Revisited," *EURASIP Journal onWireless Communications and Networking*, vol. 2006, pp. 1-13, 2006.

[23] R. A. Mucci, "An Efficient Procedure for Broadband Doppler Compensation," *ICASSP '04*, vol. 9 part 1, pp. 526-529, March 1984.

[24] R. Nawaz, and J.A. Chambers, "Partial Equalization of Multicarrier Systems in Non-Gaussian Noise," *IMA Mathematics in Signal Processing 2004*, Cirencester, U.K., 2004.

[25] R. Nawaz, and J.A. Chambers, "Robust Blind Channel Shortening in Alpha-Stable Noise," *IBCAST 2004*, Pakistan, 2004.

[26] R. Nawaz, and J.A. Chambers,"Robust Blind Channel Shortening in Impulsive Noise Environments," *EUSIPCO 2004*, Vienna, Austria, 2004.

[27] C. L. Nikias and M. Shao, *Signal Processing with Alpha-Stable Distributions and Applications*. New York: Wiley, 1995.

[28] J. R. Potter, T. W. Lim, and M. Chitre, "High-Frequency Ambient Noise in Warm Shallow Waters," in *Sea Surface Sound, UK* 1997.

[29] J. R. Potter, T. W. Lim, and M. Chitre, "Ambient Noise Environments in Shallow Tropical Seas and the Implications for Acoustic Sensing," in *Oceanology International 97 Pacific Rim, Singapore*, 1 ed 1997, pp. 191-199.

[30] J. G. Proakis, *Digital Communications*, NY: McGraw-Hill, 1995.

[31] A. W. Rihaczek, *Principles of High-Resolution Radar*, Peninsula Publishing, 1985.

[32] T.S. Rappaport, *Wireless Communications*, 2nd ed. New Jersey: Prentice Hall, 2002.

[33] A-B. Salberg and A. Swami, "Doppler and Frequency-Offset Synchronization in Wideband OFDM," *IEEE Transactions on Wireless Communications*, vol. 4 issue 6, pp. 2870-2881, November 2005.

[34] B.S. Sharif, J. Neasham, O.R. Hinton, A.E. Adams, J. Davies, **"**Adaptive Doppler Compensation for Coherent Acoustic Communication," *IEEE Proceedings on Radar, Sonar and Navigation*, vol. 147 issue 5, pp. 239-246, October 2000.

[35] B.S. Sharif, J. Neasham, O.R. Hinton, A.E. Adams, **"**A Computationally Efficient Doppler Compensation System for Underwater Acoustic Communications," *IEEE Journal of Oceanic Engineering*, vol. 25 issue 1, pp. 52-61, January 2000.

[36] A. Song, M.Badiey, "Generalized Equalization for Underwater Acoustic Communications,**"** in *Proceedings of MTS/IEEE TECHNO-OCEANS '05*, vol. 2, pp. 1522-1527, September 2005.

[37] M. Stojanovic, "Recent Advances in High Rate Underwater Acoustic Communications," *IEEE Journal of Oceanic Engineering*, vol. 21, pp. 125-136, April 1996.

[38] M. Stojanovic, J. A. Catipovic, and J. G. Proakis, "Adaptive Multi-channel Combining and Equalization for Underwater Acoustic Communications," *J. Acoust. Soc. Am.*, vol. 94, pp. 1621-1631, 1993.

[39] M. Stojanovic, J. A. Catipovic, and J. G. Proakis, "Phase-coherent Digital Communications for Underwater Acoustic Channels," *IEEE J. Oceanic Eng.*, vol. 19, no. 1, pp. 100-111, 1994.

[40] M. Stojanovic and Z. Zvonar, "Mulitchannel Processing of Broad-Band Multiuser Communication Signals in Shallow Water Acoustic Channels," *IEEE Journal of Oceanic Engineering*, vol. 21, pp. 156-166, April 1996.

[41] B. A. Tan, "Multichannel Communication Based on Adaptive Equalization in Very Shallow Water Acoustic Channels," M.Eng. Thesis, Singapore: National University of Singapore, 2006.

[42] S. P. Tan, T. B. Koay, P. Venugopalan, M. A. Chitre, and J. R. Potter, "Development of a shallow water ambient noise database," in *Underwater Technology 2004, Taiwan* 2004.

[43] I. Tolstoy and C.S. Clay, *Ocean Acoustics; Theory and Experiment in Underwater Sound***,** New York: McGraw-Hill, 1966.

[44] J. J. van de Beek, M. Sandell, and P. O. Borjesson, "ML Estimation of Time and Frequency Offset in OFDM Systems," in *IEEE Transactions On Signal Processing*, vol. 45 no. 7, pp. 1800-1805, July 1997.